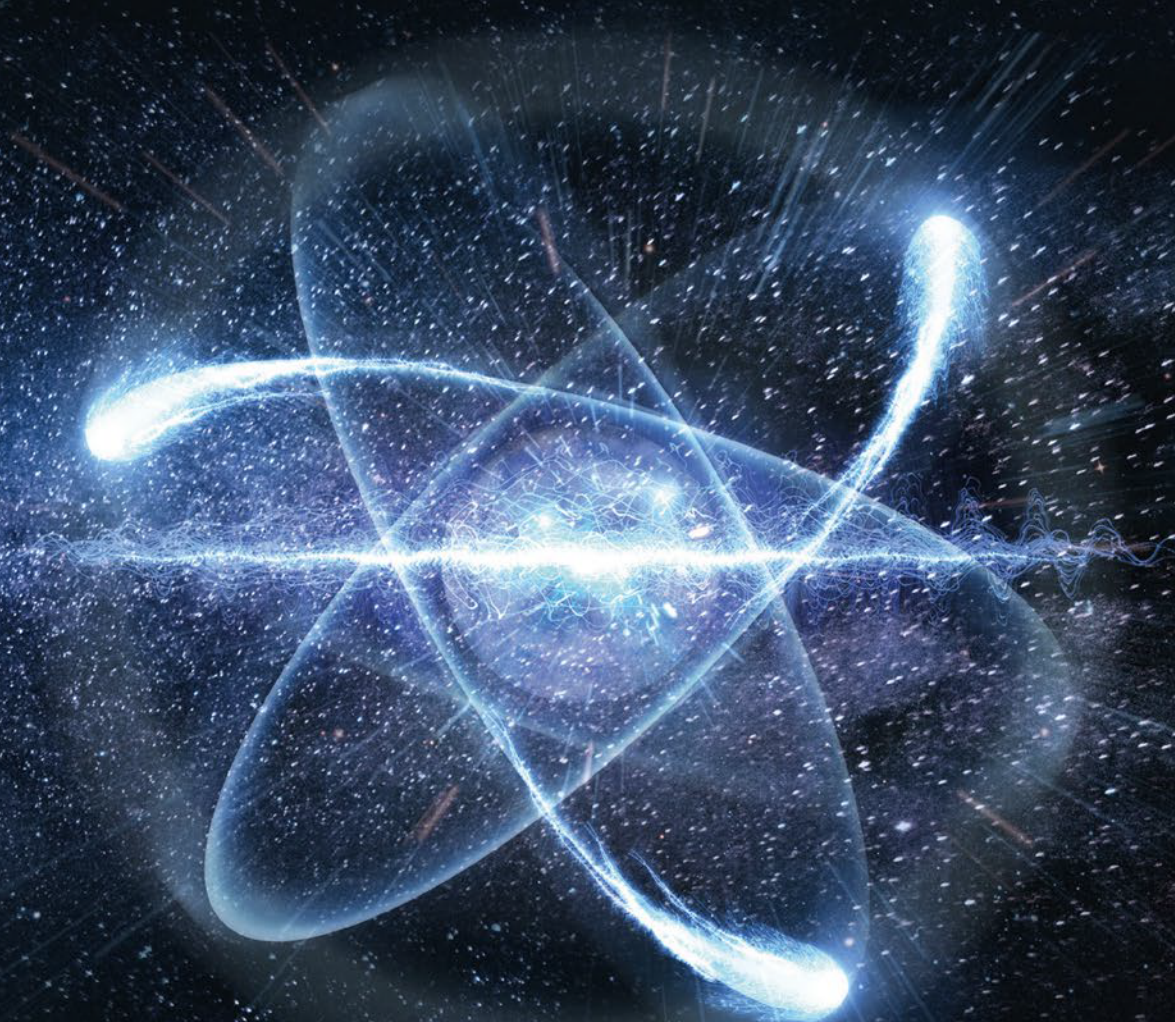




The International Journal of Nuclear Safeguards and Non-Proliferation



Editorial Board

K. Axell (SSM, Sweden)
 V. Berthou (EC, JRC, G.II.7, Italy)
 S. Cagno (EC, JRC, G.II.7, Italy)
 A. De Luca (EC, JRC, G.II.7, Italy)
 S. Grape (UU, Sweden)
 O. Okko (STUK, Finland)
 I. Popovici (CNCAN, Romania)
 G. Renda (EC, JRC, G.II.7, Italy)
 A. Reznicek (Uba GmbH, Germany)
 R. Rossa (SCK-CEN, Belgium)
 J. Rutkowsky (SNL, USA)
 Z. Štefánka (HAEA, Hungary)
 E. Stringa (EC, JRC, G.II.7, Italy)
 A. Tomanin (DG ENER, Luxembourg)
 J. Tushingham (NNL, United Kingdom)

Papers submitted for publication are reviewed by independent authors including members of the Editorial Board.

Manuscripts are to be sent to the Editor (EC-ESARDA-BULLETIN@ec.europa.eu) following the paper guidelines available in the ESARDA Bulletin section of the ESARDA website (<https://esarda.jrc.ec.europa.eu/>) where the bulletins can also be viewed and downloaded.

Accepted manuscripts are published free of charge.

N.B. Articles and other material in the ESARDA Bulletin do not necessarily present the views or policies of either ESARDA nor the European Commission.

ESARDA Bulletin is published jointly by ESARDA and the Joint Research Centre of the European Commission and distributed free of charge to over 700 registered members, libraries and institutions Worldwide.

The publication is authorized by ESARDA.

© Copyright is reserved, but part of this publication may be reproduced, stored in a retrieval system, or transmitted in any form or by any means, mechanical, photocopy, recording, or otherwise, provided that the source is properly acknowledged.

Cover designed by Christopher Craig Havenga, (EC, JRC, G.II.7, Italy)

*Printed by
IMPRIMERIE CENTRALE, Luxembourg*

Bulletin

Table of Content Issue n° 59

Editorial

Elena Stringa	1
Optimisation and uncertainty estimation of the enrichment meter measurement technique for UF6 cylinders	2
Jean-Luc Dufour, Nicolas Pepin, Clement Deyglun and Anne-Laure Weber	
New developments in neutron counting chains for safeguards.....	11
Giovanni Varasano, Mahel Abousahl, Tatjana Bogucarska, Bent Pedersen	
Nuclear forensics via the electronic properties of particulate and samples	21
Robert B. Hayes, Ryan P. O'Mara, Fatma Abdelrahman	
Production of particle reference and quality control materials	29
Timothy R. Pope, Bruce W. Arey, Mindy M. Zimmer, Michael DeVore II, Michael G. Bronikowski, Wendy Kuhne, Aaron T. Baldwin, Cristina Padilla-Cintron, Norman C. Anheier, Marvin G. Warner, Matthew S. Wellons, and Christopher A. Barrett	
Nuclear archaeology: reconstructing reactor histories from reprocessing waste.....	39
Antonio Figueroa, Malte Götsche	
Verification of spent fuel inside dry storage casks using fast neutrons	47
Young Ham, Shivakumar Sitaraman, Phil Kerr	
Development and examination of a proliferation trade risk metric	57
Adam Attarian, Peter Heine, Amanda Sayre	

Editorial

Elena Stringa

Dear readers,

I am pleased to send you the 59th issue of the *ESARDA Bulletin — The International Journal of Nuclear Safeguards and Non-Proliferation*.

On behalf of the Editorial Committee, I would like to thank all the authors and reviewers for the time and energy they have dedicated to providing high-quality articles that are of great interest to ESARDA. Publishing valuable contributions is essential in order to be considered by Scopus: while I am writing this editorial, we are still waiting for the evaluation result from the Scopus Content Selection and Advisory Board. The response from Scopus is expected no later than mid January 2020, so please check our ESARDA web page regularly for updates.

I am also pleased to announce that the ESARDA Editorial Committee has set up a newsletter, entitled *ESARDA Connector*, which hosts news from ESARDA working groups and on past and future events, as well as technical articles that do not meet the requirements to be published in the Bulletin, but that are, however, of interest to the ESARDA community. The newsletter is issued twice a year, with an autumn and a spring edition, and will be published online on the ESARDA website, where it can be downloaded for free. Anyone who would like to contribute to the newsletter with information about events or technical articles that could be of interest to the ESARDA community is strongly encouraged to send their contribution by email to EC-ESARDA-CONNECTOR@ec.europa.eu.

I encourage ESARDA researchers to publish their work at any time so that the ESARDA community as a whole can benefit from the latest relevant research novelties. In order to submit a contribution you are kindly asked to follow the instructions given on the ESARDA website at <https://esarda.jrc.ec.europa.eu>.

Moreover, I would like to encourage members of the safeguards community to volunteer as potential reviewers by

sending an email to EC-ESARDA-BULLETIN@ec.europa.eu, specifying the area of expertise by choosing from the following list:

- non-destructive analysis
- destructive analysis
- arms control and nuclear disarmament verification
- geological repositories
- spent-fuel verification and spent-fuel transfer
- containment and surveillance
- process monitoring
- statistical methodologies
- implementation of safeguards
- safeguard methodologies
- nuclear security.

I would also like to take this opportunity to recommend that you cite articles and findings published in the ESARDA Bulletin in order to increase the visibility and citing index of ESARDA activities.

Finally, I would like to express my sincere thanks to Andrea De Luca, webmaster and essential assistant, for the preparation of the ESARDA Bulletin. Thank you very much for your engagement, for your pertinent suggestions and for your fruitful ideas that support our work, allowing the dissemination of knowledge in the ESARDA community. Your contributions are essential and highly appreciated.

Merry Christmas and a happy 2020!

Dr Elena Stringa

Editor of the *ESARDA Bulletin — The International Journal of Nuclear Safeguards and Non-Proliferation*

<https://esarda.jrc.ec.europa.eu/>

ec-esarda-bulletin@ec.europa.eu

Elena.Stringa@.ec.europa.eu

Optimisation and uncertainty estimation of the enrichment meter measurement technique for UF₆ cylinders

Jean-Luc Dufour, Nicolas Pepin, Clement Deyglun and Anne-Laure Weber

IRSN

Fontenay-Aux-Roses, France

Email: jean-luc.dufour@irsn.fr, nicolas.pepin@irsn.fr, clement.deyglun@irsn.fr, anne-laure.weber@irsn.fr

Abstract:

IRSN carries out on-site non-destructive assay of nuclear material for domestic safeguards purposes in France. The paper presents the study of uncertainty components and the optimisation of the traditional uranium enrichment meter method, applied to UF₆ in 30B and 48Y cylinders. This calibration-based gamma spectrometry technique measures the enrichment by quantifying the count rate in the 185.7 keV peak of uranium 235 in conditions of infinite thickness of the measured material. It is based on high resolution gamma spectrometry measurements coupled with an ultrasonic gauge. The calibration is performed with the spectrometer in a collimated geometry using U₃O₈ laboratory standards, whereas UF₆ assays performed on-site are un-collimated in order to reduce the inspection time. Therefore, corrections need to be done to correct for the differences between laboratory and on-site measurements, and associated uncertainties have to be taken into account. A measurement of the container wall thickness is performed using an ultrasonic gauge in order to correct the gamma ray attenuation through the container wall. On-site tests and MCNP simulations were also performed to calculate a calibration transfer factor and evaluate the impact of different detector localisations on the count-rate acquisition. In addition, these tests showed the impact of the background, mainly due to the higher energy gamma rays of U-238 daughters that Compton scattered within UF₆ and the detector. Finally, the measurement time was estimated, the use range of the technique was defined and the measured uranium enrichment uncertainty was calculated.

Keywords: enrichment; UF₆; spectrometry; uncertainty; MCNP

1. Introduction

IRSN carries out on-site non-destructive assay of nuclear material as part of its mission of technical assistance to the Authority responsible for the protection and control of nuclear material in France. In order to enlarge its measurement control capabilities to uranium hexafluoride (UF₆) contained in 30B and 48Y cylinders, a study was conducted to develop a dedicated measurement system including software and mechanical support development. For this

purpose, the traditional enrichment meter method was adapted to high resolution gamma spectrometry instrumentation and U₃O₈ standards available within IRSN nuclear material metrology laboratory.

High resolution portable gamma spectrometry measurements are routinely used to verify the U-235 enrichment in large UF₆ cylinders applying the calibration-based method known as the enrichment meter method in conjunction with an ultrasonic measurement of the container wall thickness [1-9]. Calibration between the uranium enrichment and the net count rate of the 185.7 keV gamma ray in a collimated geometry is performed at IRSN using U₃O₈ reference materials (U-235 from 0.7 % to 89 %). Due to the small dimensions of the reference materials (48 mm diameter by 26 to 33 mm filling height), the collimation is needed during calibration to fulfil the infinite thickness conditions at 185.7 keV. But the collimation cannot be applied on UF₆ cylinders on-site with reasonable container inspection time. It is therefore proposed here:

- to measure the net count rate of the 185.7 keV gamma ray from the UF₆ container in a non-collimated geometry in order to reduce the container inspection time on-site;
- to correct the differences in gamma-ray attenuation between the container wall of the U₃O₈ reference material and the container wall of the 30B and/or 48Y cylinder, in measurement geometry and in chemical composition between the reference materials and the item to be measured.

This paper presents the methodology and equipment implemented on-site within the framework of a qualification measurement campaign, and the study of uncertainty components. It also discusses some improvement prospects to reduce the measurement uncertainty.

2. Measurement principle

The enrichment meter method is based on the proportional relation between the U-235 enrichment value and the count rate for 185.7 keV gamma rays. If the detector views only a fraction of the uranium sample through a collimator, the 185.7 keV gamma rays from only a fraction of the total sample radiation reach the detector because of the strong absorption of uranium. This is the ‘infinite-thickness’ criterion (Table 1 lists the infinite-thickness values) [7]. The size

of this visible volume is independent of the U-235 enrichment and depends only on the collimated geometry and uranium's physicochemical properties.

Uranium compound	Density	Infinite thickness (cm)
Metal	18.7	0.26
UF ₆ (solid)	4.7	1.43
UO ₂ (powder)	2.0	2.75
U ₃ O ₈ (powder)	7.3	0.74

Table 1: Mean free paths and infinite thickness for 185.7 keV gamma rays in uranium compounds [7].

This method presents the following limitations:

- only the near surface depth of the uranium sample is interrogated, which means that the material must be isotopically uniform;
- the available reference materials are small and need a narrow collimator to fulfil the infinite thickness requirements which require significant measurement time. Large measurement times are possible during the calibration in the laboratory, but not consistent with on-site measurements. Thus, a calibration transfer function (C_{TFE}) is calculated to measure the on-site sample without collimation, using calibration performed with collimation on reference materials;
- the calibration is performed with U₃O₈, but on-site UF₆ is measured. The coefficient F/F' corrects for the difference in chemical composition;
- if the measured material is embedded within a container, the gamma rays are attenuated by the container wall. The correction factor CF_c corrects for such attenuation;
- the detector efficiency can change between the calibration in the laboratory and the measurement on-site. The correction factor CF_e corrects for the variations in efficiency.

Taking into account all these correction factors, U-235 enrichment E can be expressed as follows:

$$E = \left(A + B \times [R \times CF_c \times C_{TFE} \times CF_e] \right) \times \left(\frac{F}{F'} \right) \quad (1)$$

where A, B are constants calculated during the calibration in collimated configuration with U₃O₈ reference materials. The term in brackets contains the measured net count rate at 185.7 keV obtained in non-collimated configuration (R) and correction factors. Each component is studied in the following paragraphs.

The measurement system implemented on-site contains a portable high resolution gamma spectrometer Detective type (AMETEK/ORTEC), a computer equipped with both Gammavision software (AMETEK/ORTEC) and in-house Enrichment software to drive the spectrum acquisition and apply the enrichment meter method, a shielding, a collimator, a spectrometer positioning system and an ultrasonic measurement system. The measurement set-up is shown in Figure 1.

3. Container wall impact

The component $CF_c = e^{-\mu_c T_c}$ corrects the attenuation of gamma rays by UF₆ container wall:

- μ_c the photon linear attenuation coefficient (bibliographical data);
- T_c the container wall thickness (measured using an ultrasonic thickness gauge).

The variance of the wall attenuation correction is given by the following expression:

$$u_{CF_c}^2 = \left(\frac{\partial e^{-\mu_c T_c}}{\partial \mu_c} \right)^2 u_{\mu_c p_c}^2 + \left(\frac{\partial e^{-\mu_c T_c}}{\partial T_c} \right)^2 u_{T_c}^2 \quad (2)$$

$$\left(\frac{u_{CF_c}}{CF_c} \right)^2 = (\mu_c T_c)^2 \left[\left(\frac{u_{\mu_c}}{\mu_c} \right)^2 + \left(\frac{u_{T_c}}{T_c} \right)^2 \right] \quad (3)$$

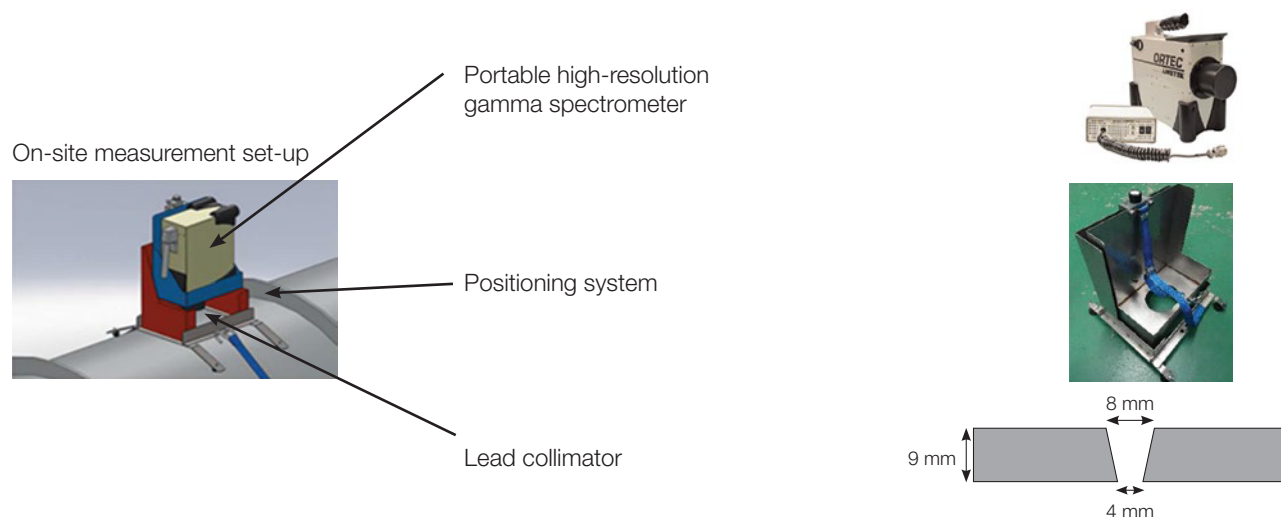


Figure 1: Measurement configuration.

Expressions and values of the parameters of Equation 2 and Equation 3 are presented in Sections 3.1 and 3.2. A numerical estimation of the variance is presented in Section 3.3.

3.1 Container wall measurement T_c

In the absence of a known reference standard stainless steel ASTM A516 Grade 65 type block, the ultrasonic gauge calibration was based on thickness measurements on the edge of UF₆ containers with a digital micrometer (0.001 mm resolution and ± 0.002 mm precision), considered as a reference. Thickness measurements with the ultrasonic gauge were then performed at the same location, adjusting the ultrasound speed according to the thickness value measured with the micrometer. Once the speed was fixed, the bias and precision of the ultrasonic gauge was evaluated (Figure 2).

The best measurements are obtained at a speed of 5925 m/s and the average wall thickness of measured 30B containers is 13.206 mm. The difference between the micrometer and the ultrasonic gauge measurements shows a uniform distribution. The precision (Equation 4) and the bias (Equation 5) are then calculated as follows [10]:

$$\text{precision} = \frac{\Delta_{\max} - \Delta_{\min}}{2\sqrt{3}} = 0.046\text{mm} \quad (4)$$

$$\text{bias} = \frac{\sum_{i=1}^n \Delta_i}{n} = -0.043\text{mm} \quad (5)$$

The overall uncertainty of the container wall thickness u_{T_c} (Equation 6) also includes components due to resolution, container paint thickness, ultrasound speed variations with temperature and container wall dilatation with temperature. These components are presented in Table 2.

$$u_{T_c} = \sqrt{u_{\text{calib}}^2 + u_{\text{resol}}^2 + u_{\text{speed}}^2 + u_{\text{dilat}}^2} = 0.118\text{mm} \quad (6)$$

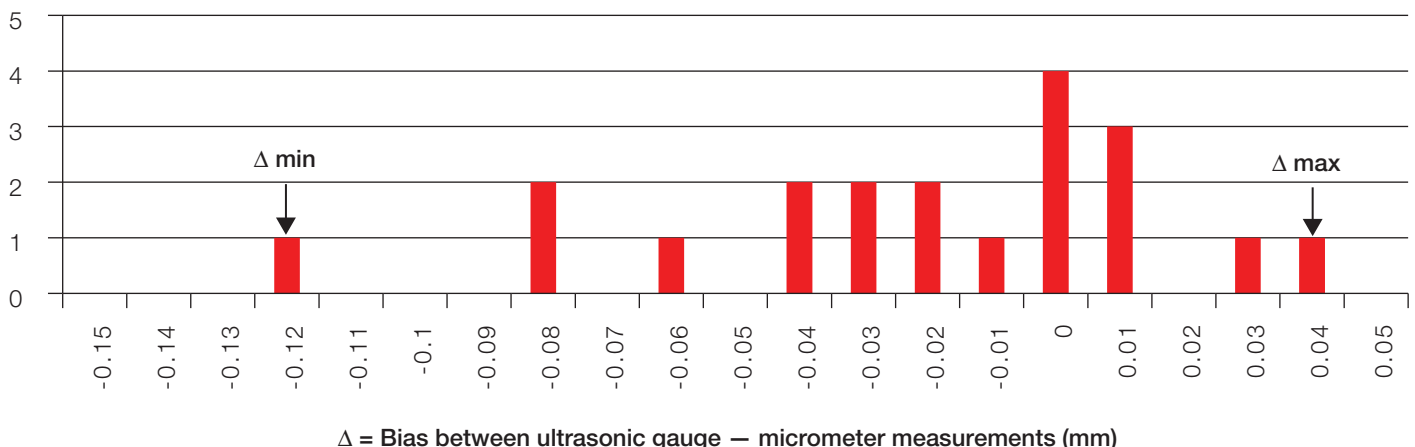


Figure 2: Distribution of the bias between the ultrasonic gauge and the micrometer during the measurement of the edge of containers.

Denomination	Comments	Evaluation
Calibration	Takes into account bias and precision from the calibration, but also additional bias sources such as the curvature of the container ($u_{\text{curve}} = 0.012\text{mm}$) and coating ($u_{\text{coating}} = 0.031\text{mm}$).	$u_{\text{calib}} = u_{\text{precision}} + \frac{ u_{\text{bias}} + u_{\text{curve}} + u_{\text{coating}} }{\sqrt{3}}$ $u_{\text{calib}} = 0.096\text{mm}$
Resolution	The resolution of the ultrasonic gauge is 0.01 mm. At each measurement there could be an error of $\pm 0.01/2$ mm.	Error is described by a uniform distribution: $u_{\text{resol}} = 0.01 / 2\sqrt{3}$ $u_{\text{resol}} = 2.887 \times 10^{-3}\text{mm}$
Variation of ultrasounds speed with temperature	The ultrasound's speed depends on the matter temperature. If the gauge is calibrated at 20 °C but the container wall is warmer, ultrasounds are slower and the wall appears thicker.	In winter, the container wall can be about -10 °C and in summer 60 °C (range of use defined by the manufacturer of the ultrasonic gauge) $u_{\text{speed}}[-10^\circ\text{C};60^\circ\text{C}] = 0.068\text{mm}$
Container wall dilatation with temperature	The dilatation of the wall decreases the matrix density and increases the thickness.	$u_{\text{dilat}} = 4.191 \times 10^{-3}\text{mm}$

Table 2: Components of the wall thickness measurement overall uncertainty.

3.2 Container wall attenuation correction

The typical chemical composition of 30B or 48Y containers (ASTM A516) and maximal fractions are presented in Table 3 [11].

C	Mn	Si	Al	P	S
0.18 (max = 0.26)	1.05 (0.85-1.20)	0.32	0.04	0.015 (max = 0.035)	0.008 (max = 0.035)

Table 3: Typical chemical composition of ASTM A516 Grade 65 and maximum [11].

μ_c for 185.7 keV gamma rays is calculated using XMuDat software [12] by assuming ASTM A516 Grade 65 and a density of 7.75. The coefficient is calculated for a typical composition and two ‘extreme’ compositions: μ_{min} is calculated with the minimal iron concentration and the maximum concentration for the other elements and μ_{max} is calculated with iron only.

$$\mu_{typical\ composition} = 1.222\text{ cm}^{-1}$$

$$\mu_{min} = 1.210\text{ cm}^{-1} \text{ and } \mu_{max} = 1.231\text{ cm}^{-1}$$

We assume a uniform distribution of μ between μ_{min} and μ_{max} , thus:

$$\mu_c = \frac{\mu_{max} + \mu_{min}}{2} = 1.221\text{ cm}^{-1} \quad (7)$$

and:

$$u_{\mu_c} = \frac{\mu_{max} - \mu_{min}}{2\sqrt{3}} = 0.006\text{ cm}^{-1} \quad (8)$$

3.3 Conclusion about the wall impact

The wall of the container absorbs gamma rays. The coefficient CF_c is applied in Equation 1 to correct these absorptions but it induces uncertainty. A numerical estimation of the variance (Equation 3) based on Equation 6 and Equation 8 is calculated using the data provided in the previous paragraphs. The variance of the wall attenuation correction u_{CF_c} depends on the measured wall thickness. An average

thickness of 13.206 mm induces a variance $\frac{u_{CF_c}}{CF_c}$ of 1.644 %.

4. Impact of the detector location

The distribution of solid UF_6 inside the container is an important, but unknown, measurement parameter. MCNP6 simulations were performed to determine the influence of the detector position and the filling level on the enrichment measurement. On-site tests were also performed to check the simulation results.

4.1 MCNP6 simulations

MCNP6 [13] was used to model the gamma ray transport through UF_6 and 30B cylinder (Figure 3). Tally F5 (flux at a point) was used for the gamma ray spectrum detection, and only 185.7 keV gamma rays were generated. Many hypotheses are assumed for the model, as shown below:

- H1. uniform properties of UF_6 (uniform chemical, isotopic composition and uniform density);
- H2. gamma rays emitted by the gaseous UF_6 neglected;
- H3. uniform wall thickness.

The impact of the detector location and the filling level on measurement results is studied by considering different detector locations on 30B container and filling level. Three locations (D1, D2 and D3) and different filling levels were studied as described in Figure 4.

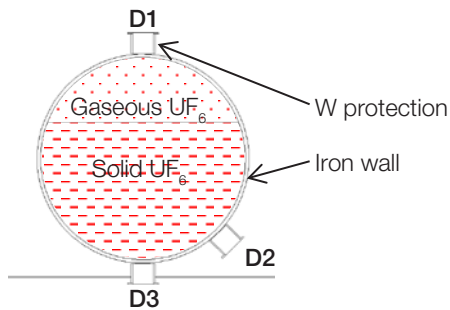


Figure 3: Cross section through a MCNP model of a 30B container.

As we can see in Figure 4, for filling levels higher than 30 cm (approximately 2180 kg) locations D1, D2 and D3 can be used interchangeably.

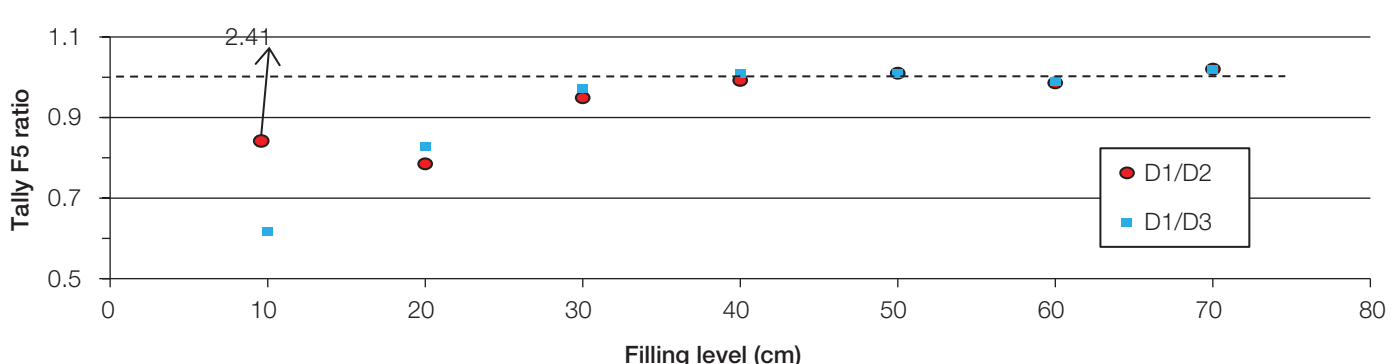


Figure 4: Ratios of tally F5 for different localisation (D1, D2 and D3) and filling levels.

4.2 On-site measurements

The influence of the detector position on the enrichment measurement is evaluated experimentally for seven detector locations along a 30B container (filled with 2200 kg of UF_6 , at 1.41 % enrichment). At each detector position a thickness measurement is performed with the ultrasonic gauge to correct for the attenuation of the photons in the container wall. Locations and results are provided in Figure 5.

The relative standard deviation of the distribution of the count rate according to the detector position is around 1.1 %, which is less than the repeatability uncertainty (1.35 %).

4.3 Conclusion about the detector location

Simulation and on-site measurements show that detectors at the top and on the side of the container can be used interchangeably if the 30B container contains at least 2200 kg of UF_6 . A measurement position at the top of the container and centred along the cylinder axis has the following two advantages:

- it is the most practical location to install the system;
- the acquisition is less impacted by the background generated by surrounding containers.

5. Correction due to the differences in chemical composition between reference materials and item to be measured

In the Equation 1 the coefficient $\frac{F}{F'}$ corrects the predicted enrichment from the differences in chemical composition between the reference material and the item to be measured (based on the data in Table 4). In case of UF_6 enrichment measurements based on a calibration performed with U_3O_8 samples, a correction factor of 1.02 needs to be applied to the enrichment value obtained from the calibration.

	Nuclear Material of Items Measured (Factor F)					
Nuclear Material of Calibration Standards (Factor F')	U	UC	UC_2	UO_2	U_3O_8	UF_6
U (100 % U)	1.00	1.00	1.00	1.01	1.01	1.04
UC (95 % U)	1.00	1.00	1.00	1.01	1.01	1.03
UC_2 (91 % U)	0.99	1.00	1.00	1.00	1.01	1.03
UO_2 (88 % U)	0.99	0.99	1.00	1.00	1.00	1.03
U_3O_8 (85 % U)	0.99	0.99	0.99	1.00	1.00	1.02
UF_6 (68 % U)	0.96	0.97	0.97	0.98	0.98	1.00
U nitrate (47 % U)	0.92	0.92	0.93	0.93	0.93	0.95

Table 4: Material composition correction factors (F/F') [7].

Table 4 does not provide any associated uncertainties $u_{F/F'}$. Taking two ratios F/F' with small difference, for example $F/F'_1 = 1$ and $F/F'_2 = 1.01$, these two values are random values with means of 1 and 1.01 and associated uncertainties u_{F/F'_1} and u_{F/F'_2} . If we use the classic comparison test to compare the two means:

$$\frac{|F/F'_1 - F/F'_2|}{3 \sqrt{\frac{u_{F/F'_1}^2 + u_{F/F'_2}^2}{2}}} < 1 \quad (9)$$

If the test of Equation 9 is true, the two means can be considered equal with a ‘false alarm’ probability of 0.26 %, and the difference is due to their associated uncertainties u_{F/F'_1} and u_{F/F'_2} . $|F/F'_1 - F/F'_2| = 0.01$ and the inequality becomes $3 \sqrt{\frac{u_{F/F'_1}^2 + u_{F/F'_2}^2}{2}} > 0.01$. If we assume the two uncertainties u_{F/F'_1} and u_{F/F'_2} are equal, i.e. $u_{F/F'_1} = u_{F/F'_2} = u_{F/F'}$, the inequality becomes $3 \sqrt{2u_{F/F'}^2} > 0.01$ and $u_{F/F'} = \frac{0.01}{3\sqrt{2}} = 0.0024$.

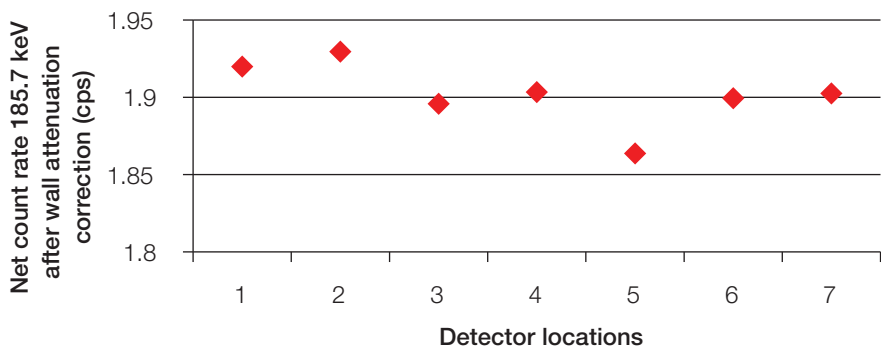
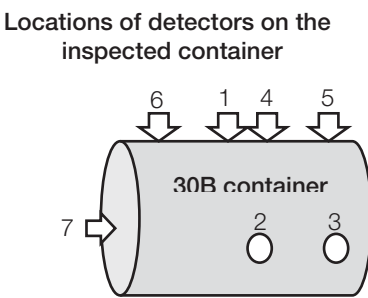


Figure 5: Impact of the detector localisation on the 185.7 keV gamma ray count rate (on-site measurements).

6. Correction due to the non-collimated geometry

Calibration with reference materials is performed in a collimated configuration to fulfil the infinite thickness requirements. By removing the collimator during on-site measurements on UF_6 cylinders, the calibration conditions are modified and then the counting rate measured for an unknown sample needs to be corrected with a calibration transfer function (C_{TFE}). C_{TFE} is derived from the ratio between the counting rates at 185.7 keV recorded in the two measurement configurations, with and without collimation. MCNP6 [13] simulations were performed to determine the C_{TFE} coefficient and were compared with on-site measurements.

6.1 MCNP6 simulations

MCNP6 was used to model the gamma-ray transport through UF_6 , 30B cylinder and HPGe detector. A precise

model of a 12 % relative efficiency p-type HPGe coaxial detector was created for photon detection (see Figure 6). Detector resolution and dead layers were determined by different experiments. The model was validated by comparing calculated and experimental full energy peak counting and FWHM for an Eu-152 source.

The gamma spectra are obtained using tally F8 (pulse height distribution). Collimated and non-collimated simulation results are presented in Figure 7.

C_{TFE} is derived from the ratio between the counting rates at 185.7 keV recorded in the two measurement configurations, with and without collimation, and is estimated at 0.00456. The associated uncertainty ($u_{C_{TFE}}$) includes components due to the trueness of the model, statistic and software deconvolution uncertainties $u_{C_{TFE}} = \sqrt{u_{\text{model}}^2 + u_{\text{stat}}^2 + u_{\text{peak}}^2} = 9.23\%$. These components are presented in Table 5.

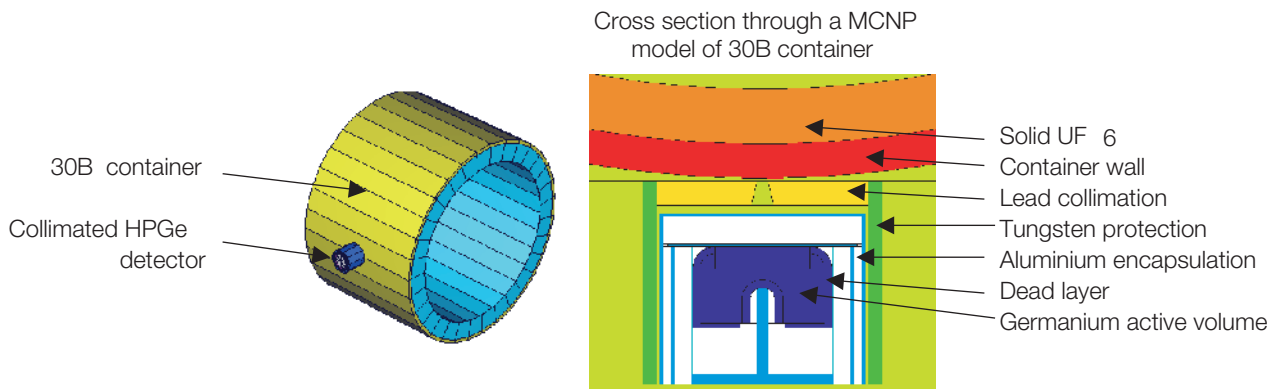


Figure 6: Model of the HPGe detector in collimated configuration (the lead collimator is replaced by air in the non-collimated configuration).

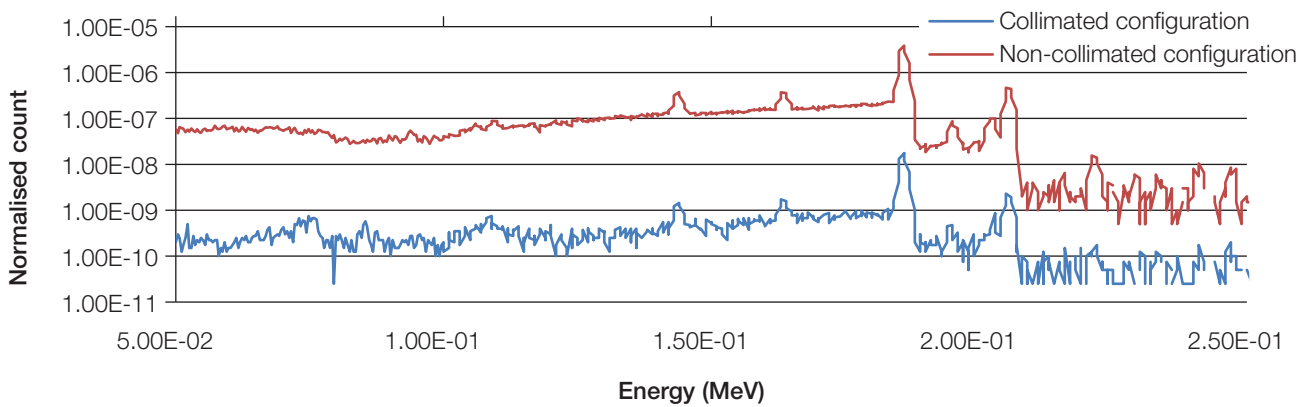


Figure 7: MCNP6 spectra of U-235.

Designation	Origin	Estimation	Comments
u_{model}	Adjustment of the MCNP model	4.65 %	Estimated with Eu-152 source between 80 keV and 1408 keV.
u_{stat}	Statistical uncertainty of Monte Carlo simulation	7.65 %	Mainly due to the low efficiency of the collimated configuration. Uncertainty could be reduced by increasing the calculation time
u_{peak}	Subtraction of the continuum background of the peak area	2.23 %	The simulation is free from the background continuum due to U-238

Table 5: Components of $u_{C_{TFE}}$.

6.2 Experimental C_{TFE}

Experimental measurements have been performed on one 30B container to estimate C_{TFE} . Three 120 seconds measurement time acquisitions are enough to get good counting statistics in the non-collimated configuration, but the collimated configuration needs a long measurement time (> 13 hours) to have good statistical uncertainty. The counting rates recorded in the collimated configuration on the side and at the top of the container are different due to the background from the other containers. C_{TFE} was calculated with the system at the top of the container, where the background contribution of the neighbour containers is small, and estimated at 0.00476.

C_{TFE} is derived from the ratio between the net counting rates at 185.7 keV recorded in the two measurement configurations, with and without collimation.

$$C_{TFE} = \frac{N_{\text{with colli}}}{t_{\text{with colli}}} / \frac{N_{\text{without colli}}}{t_{\text{without colli}}} \quad (10)$$

where $N_{\text{with colli}}$ is the number of detected 185.7 keV gamma rays for the collimated configuration and $t_{\text{with colli}}$ is the measurement time. Thus, the associated uncertainty

$\left(\frac{u_{C_{TFE}}}{C_{TFE}} \right)^2$ is expressed as follows:

$$\begin{aligned} \left(\frac{u_{C_{TFE}}}{C_{TFE}} \right)^2 &= \left(\frac{u_{N_{\text{with colli}}}}{N_{\text{with colli}}} \right)^2 + \left(\frac{u_{t_{\text{with colli}}}}{t_{\text{with colli}}} \right)^2 + \\ &+ \left(\frac{u_{N_{\text{without colli}}}}{N_{\text{without colli}}} \right)^2 + \left(\frac{u_{t_{\text{without colli}}}}{t_{\text{without colli}}} \right)^2. \end{aligned} \quad (11)$$

The contribution of the measurement time uncertainties

$\left(\frac{u_{t_{\text{with colli}}}}{t_{\text{with colli}}} \right)^2$ and $\left(\frac{u_{t_{\text{without colli}}}}{t_{\text{without colli}}} \right)^2$ is neglected, and in Equation 11 leads to:

$$\frac{u_{C_{TFE}}}{C_{TFE}} = 3.40\%$$

Despite a long measurement time, the relative uncertainty related to the counting rate with collimation is high (3.4 %) due to the poor signal-to-noise ratio. The noise is attributed to the Compton continuum of higher energy photons mainly coming from the large amounts of U-238 in the item and the *bremsstrahlung* emitted by its daughters.

6.3 Conclusion about C_{TFE}

MCNP6 was used to estimate the calibration transfer function correction, but modelling uncertainties and simulation time induce significant uncertainties. In the end, the experimental C_{TFE} has a better uncertainty. C_{TFE} is needed because on-site measurements and calibration conditions are different.

7. Calibration and inverse calibration

The reference materials available within the laboratory are four U_3O_8 powder samples, infinitely thick with respect to the 185.7 keV gamma emission, embedded in a POMC (Acetal Copolymer) container. Their characteristics are summarised in Table 6.

U_3O_8 mass (g)	Enrichment (wt %)	Enrichment Unc. (wt %)
120.9	0.714	0.005
114.73	3.038	0.018
106.81	29.187	0.018
104.74	89.303	0.018

Table 6: Reference materials ^{235}U enrichment.

The calibration is performed in a collimated geometry as follows: the reference material is placed on the collimator, which is itself positioned against the front face of the germanium detector, both of them being centred on the axis of the coaxial germanium detector. The calibration consists in measuring the net counting rate at 185.7 keV (R_i) for each reference material using the ROI (Region Of Interest) report option of the Gammavision software. The correction factor CF_r is then applied to correct it from the attenuation of the wall thickness, and a weighted least-squares linear regression is applied to the couples (R_i, E_i), E_i being the U-235 enrichment value given by the certificate. The measurement time is defined in order to get a counting statistics of around 1 % in the 185.7 keV net peak area.

The correction factor due to the attenuation from the reference material container wall (CF_r) is estimated experimentally by performing the ratio $CF_r = \frac{R_0}{R}$, where R_0 is the counting rate measured at 184.4 keV with a ^{166m}Ho source and R is the counting rate measured when an equivalent container wall is installed between the detector and this source.

The weighted linear least-squares regression is applied to the couples (R_i, E_i), using as weight the inverse of the variance of the counting rate ($g_i = \frac{1}{S_i^2}$) [14,15]. The coefficients a , b and R are given by the following expressions:

$$b = CF_r \frac{\sum g_i \sum g_i E_i R_i - \sum g_i E_i \sum g_i R_i}{\sum g_i \sum g_i E_i^2 - (\sum g_i E_i)^2} \quad (12)$$

$$R = \frac{\sum g_i R_i C F_r}{\sum g_i} = C F_r \frac{\sum g_i R_i}{\sum g_i} \quad (13)$$

and:

$$a = R - bE \quad (14)$$

Equation 12 and Equation 14 lead to calibration factors $a = -0.011496151$ and $b = 0.806211927$.

The enrichment of an ‘unknown’ item can then be predicted using the inverse calibration.

$$R = a + b \times E \quad (15)$$

$$E = A + R \times B \quad (16)$$

where R is the measured net counting rate at 185.7 keV obtained in non-collimated configuration, E is the unknown U-235 enrichment, $A = -\frac{a}{b}$ and $B = \frac{1}{b}$.

8. Overall uncertainty

The enrichment measurement uncertainty is calculated as follows:

$$u_E = \sqrt{u_{Calibration}^2 + u_{F/F'}^2 + u_{Trueness}^2} \quad (17)$$

where:

- $u_{Calibration}^2$ depends mainly on the regression model, counting rates uncertainties and corrections applied to these counting rates. Enrichment can be expressed as

follows, $E_{\text{after } \frac{F}{F'} \text{ correction}} = E_{\text{before } \frac{F}{F'} \text{ correction}} \times \frac{F}{F'}$. and thus

$$u_{Calibration}^2 = E_{\text{after } \frac{F}{F'} \text{ correction}}^2 \left(\frac{u_{E_{\text{before } \frac{F}{F'} \text{ correction}}}^2}{E_{\text{before } \frac{F}{F'} \text{ correction}}} \right)^2$$

- $u_{\frac{F}{F'}}^2$ is evaluated based on a difference of 0.01 between the ratios of two matrix material composition correction factors (Section 5);

- $u_{Trueness}^2$ is evaluated from the known enrichment-item measurements. It is calculated considering a rectangular distribution of the bias of n assays, i.e.

$$u_{Trueness} = \frac{\left| \sum_{i=1}^n (E_{\text{Reference}_i} - E_{\text{Measured}_i}) \right|}{n\sqrt{3}}$$

The inverse calibration is applied to the corrected count rate $R_{\text{corrected}}$ in order to determine the predicted enrichment $\left(E_{\text{before } \frac{F}{F'} \text{ correction}} \right)$:

$$R_{\text{corrected}} = R C_{TFE} CF_c C_e \quad (18)$$

$$u_{R_{\text{corrected}}} = R_{\text{corrected}} \sqrt{\left(\frac{u_R}{R} \right)^2 + \left(\frac{u_{CF_c}}{CF_c} \right)^2 + \left(\frac{u_{C_{TFE}}}{C_{TFE}} \right)^2 + \left(\frac{u_{C_e}}{C_e} \right)^2} \quad (19)$$

Based on Equation 16 and Equation 18, the predicted the enrichment is expressed as follows:

$$E_{\text{before } \frac{F}{F'} \text{ correction}} = \frac{(R \times CF_c \times C_{TFE} \times C_e - a)}{b} \quad (20)$$

The estimation of the predicted enrichment uncertainty before $\frac{F}{F'}$ correction $u_{E_{\text{before } \frac{F}{F'} \text{ correction}}}$ is calculated from the confidence interval of the predicted enrichment $IC_{\text{Regression}}$ [14,15]. Assuming that the confidence interval variable follows a rectangular probability law, the uncertainty associated with the predicted enrichment is given by

$$u_{E_{\text{before } \frac{F}{F'} \text{ correction}}} = \frac{IC_{\text{Regression}}}{2\sqrt{3}}.$$

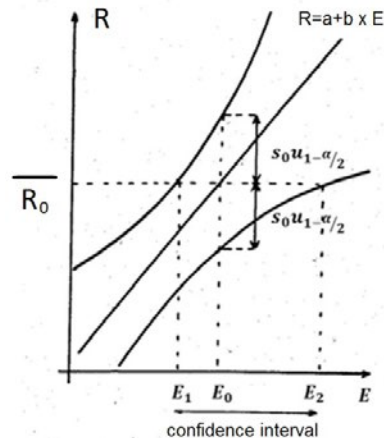


Figure 8: The enrichment confidence interval.

The enrichment confidence interval $IC_{\text{Regression}}$ is limited by E_1 and E_2 (see Figure 8). These boundaries are calculated through the intersection between $R = R_0$ and $R = a + bE \pm S_0 u_{1-\frac{\alpha}{2}}$, where $u_{1-\frac{\alpha}{2}}$ is a normal restricted variable ($u_{1-\frac{\alpha}{2}} = 3$ induces a false alarm risk of 0.26 %).

E_1 and E_2 are calculated by resolving the two following equations:

$$R_0 = a + bE_0 + S_0 u_{1-\frac{\alpha}{2}} \quad (21)$$

$$R_0 = a + bE_0 - S_0 u_{1-\frac{\alpha}{2}} \quad (22)$$

$$\text{with } S_0 = \sqrt{S_{R_{\text{corrected}}}^2 + \frac{1}{\sum g_i} + \frac{(E_0 - \bar{E})^2 \sum g_i}{\sum g_i \sum g_i E_i^2 - (\sum g_i E_i)^2}}$$

The confidence interval $IC_{\text{Regression}}$ is then made symmetrical by calculating the boundaries $E_1 = E_0 - \text{Max}(|E_0 - E_1|, |E_0 - E_2|)$ and $E_2 = E_0 + \text{Max}(|E_0 - E_1|, |E_0 - E_2|)$.

9. Conclusions

The on-site measurement of UF_6 containers and numerical simulations contributed to the validation of the U-235 enrichment calibration-based method relying on the small dimension reference materials available at IRSN. Only small U_3O_8 reference materials are available at IRSN so that collimation is needed to fulfil the infinite thickness conditions during calibration. On the other hand, in order to make

on-site verifications compatible with time inspection constraints, the 185.7 keV net counting rate is measured in a non-collimated geometry. Therefore, a transfer function between the two different geometries is applied. This correction was estimated both experimentally and numerically, with good agreement between the two of them.

The measurement uncertainty, around 5 % for low enriched uranium and 10 % for depleted uranium, could be improved in the future. Peak-fitting algorithms could be investigated in order to extract net peak area from a high background continuum with better accuracy. The geometry transfer function coefficient could be useless if the calibration was performed with a large uranium reference sample.

10. References

- [1] IAEA, *Safeguards Techniques and Equipment*, 2011 edition, *International Nuclear Verification Series No 1 (Rev. 2)*.
- [2] *Standard test method for measurement of ^{235}U fraction using enrichment meter principle*, norm ASTM C1514, 2002.
- [3] *International target values 2010 for measurement uncertainties in safeguarding nuclear materials*, STR-368, IAEA, Vienna, 2010.
- [4] Kull, L. A., Ginaven, R. O. and Glancy, J. E., 'A simple gamma spectrometric technique for measuring isotopic abundances in nuclear materials', *Atomic Energy Review*, 1976.
- [5] Kull, L. A. and Ginaven, R. O., *Guidelines for gamma-ray spectroscopy measurements of ^{235}U enrichment*, Technical Support Organization, Brookhaven National Laboratory, Upton, New York, 1974.
- [6] Carchon, R., *IAEA Verification Techniques on UF6 Shipping Cylinders*, 2007.
- [7] Reilly, D., Ensslin, N., Smith, H. and Kreiner, S., *Passive Nondestructive Assay of Nuclear Materials*, NUREG/CR-5550, LA-UR-90-732, 1991.
- [8] Mortreau, P. and Berndt, R., *Handbook of gamma spectrometry methods for non-destructive assay of nuclear materials*, European Commission Joint Research Centre, 2006.
- [9] Montgomery, J. B., 'Enhanced techniques and improved results in ^{235}U enrichment measurement of large UF6 cylinders by portable germanium spectrometer', *Journal of Nuclear Materials Management*, Vol. 34, No 2, 2006.
- [10] Feinberg, M., *Labo-Stat: Guide technique d'accréditation pour l'évaluation des incertitudes de mesure en biologie médicale*, SH GTA 14 Rev00.
- [11] *Specification for pressure vessel plates, carbon steel, high strength, for moderate and lower temperature service*, SA-516/SA-516M Section II, Part A, 2009.
- [12] Nowotny, R., *XMuDat: Photon Attenuation Data on PC*, version 1.0.1, Institut für Biomedizinische Technik und Physik, University of Vienna, AKH-4L, 1998.
- [13] Pelowitz, D. B. (ed.), *MCNP6 User's Manual — Version 1.0*, Los Alamos National Laboratory report LA-CP-13-00634 (May 2013).
- [14] CETAMA, *Statistique appliquée à l'exploitation des mesures*, Ed. MASSON, second edition, 1986.
- [15] Neuilly, M., *Modélisation et estimation des erreurs de mesures*, CETAMA, 1993.

New developments in neutron counting chains for safeguards

Giovanni Varasano, Mahel Abousahl, Tatjana Bogucarska, Bent Pedersen

European Commission, Joint Research Centre,
Nuclear Safety & Security Directorate, Nuclear Safeguards & Security Department
Nuclear Security Unit
Via E. Fermi 2749, Ispra 21027 (VA), Italy
Email: giovanni.varasano@ec.europa.eu

Abstract:

Standard neutron counting systems in nuclear safeguards typically use a thermal neutron absorber material in gas proportional counters embedded in a neutron moderator block, and surrounding the central sample cavity. Multiple detector tubes are normally connected to one electronics chain composed of a pre-amplifier, an amplifier, a single channel analyser and a digital signal mixer summing signals from multiple chains to produce a single pulse train representing the neutron detection events. This has typically been the design compromise considering factors such as the dead-time of the detection system, the reliability of the electronics, complexity and cost.

In this paper we describe the ongoing developments at JRC for modernizing the entire electronics chain, including all the individual components mentioned above as well as the digital signal analyser. A key element of this work concerns an in-house designed digitizer board capable of processing pre-amplifier outputs to identify neutron detection events. The board has multiple analogue inputs, a multichannel ADC, pulse processing in FPGA hardware and output of timestamps of neutron detection events. The benefits from this work are expected to be a reduced pulse processing time in the electronics, better pulse pair resolution, the elimination of the physical signal analyser and better systems diagnostics.

The new electronics developments are being assembled and tested in the JRC reference passive neutron counter, and will be ready for demonstration in the coming year. The reference counter is a cylindrical well-counter incorporating 126 ^3He neutron detector tubes.

Keywords: NDA; neutron counter; digitiser; list-mode; safeguards

1. Introduction

Several non-destructive techniques (NDA) and devices for safeguards using passive or active neutron measurement methods have been developed and tested at the Joint Research Centre (JRC) over decades.

Traditionally a neutron measurement chain consists of analogue and digital components: a detector with high voltage

bias supply, a preamplifier, an amplifier/shaper circuit and, finally, a digital discriminator. Modern neutron detection systems apply many ^3He or BF_3 gas proportional counters in order to increase the neutron detection probability and to reduce the paralysing, or updating, dead-time effects.

A necessary requirement for systems of multiple detection chains is that the resulting digital signal lines must be summed to produce one signal pulse train for the analysis, without suffering loss of real signals and without causing false spurious signals. An analogue electronics chain performs rather well when only few parallel measurement chains are used, i.e. when several detectors grouped together within a moderator block are connected to a single measurement chain.

High efficiency neutron well-counters often use dozens of such measurement chains. Particular care must be observed when manufacturing such devices in order to eliminate internally or externally generated electromagnetic noise. Such precautions can include using proper filters on the high voltage rail, using multi-layer printed circuit boards (PCBs), separating analogue and digital ground planes, avoiding creating inductive paths that may amplify ground bounces [8], etc.

Such passive neutron counting systems currently operated at JRC include, for example, the Drum Monitor, the Boron-Based Neutron Coincidence counter (BBNCC), and neutron slab counters, applying 28, 6 and 1 analogue chains respectively. These systems output Transistor-to-Transistor Logic (TTL) pulse signals, representing neutron detection events, to be counted by means of standard signal analysers such as multichannel scalers (MCS) or shift registers (SH/R) commonly used in multiplicity analysis. The analysers are routinely used with standardised measurement software, for example for nuclear inspectors.

Most often, TTL signal outputs are used to maintain compatibility with existing analysers. An important part of the analogue electronics is the discriminator that filters out signals not originating from neutron detections but from other effects, for example gamma-ray background, and false bursts caused by electromagnetic noise. The discriminator level is set carefully to avoid eliminating real neutron signals, and not to trigger multiple output signals from a single analogue pulse. Correctly setting the discriminator can, in part,

eliminate gamma background and spikes of noise caused for example, by TTL ground bounces whose noise contribution to the analogue signal can increase significantly when multiple parallel measurement chains are in use. Each analogue pulse crossing the discrimination level triggers the output of a logical pulse for further processing.

Modern technologies offer alternative approaches to the solution of problems encountered in a standard analogue chain. For example, implementing measurement components using field programmable gate arrays (FPGA), and using low-voltage differential signal standards (M-LVDS) to propagate signals within the neutron counter [1]. In case a TTL output signal is needed to maintain compatibility with external instrumentation, a digital pulse can easily be produced as output.

The text below describes such techniques and components, we have implemented so far, together with other efforts currently under development in order to process neutron detection events using more modern digital techniques.

We use a Moving Window Deconvolution (MWD) algorithm [2] to process a signal in an entirely digital fashion using appropriate digital filters implemented in FPGA state-of-the-art technology. Another effort concerns implementing a novel low-noise charge pre-amplifier to be implemented eventually with every single ^3He tube, thus avoiding connecting several tubes to a single pre-amplifier. This will reduce the updating dead-time of the combined system. An analogue pulse shaper will no longer be used, but will be substituted by a digital filter featuring a comparable or possibly shorter shaping time. A final advantage of the digital pulse processing chain is expected simply from all data being transmitted via high-speed optical USB3.0 link. Avoiding the usage of multiple 50-Ohm coaxial cables will simplify the implementation of the overall system, as expected for example in a planned high-efficiency counter using 126 ^3He tubes. Multiplicity analysis and/or multichannel scalers are easily integrated inside the FPGA fabric.

Applying a pre-amplifier to each detector tube makes the individual tubes independent rather than integrated into the shared detection system. This fact greatly facilitates the sharing of ^3He proportional counters between neutron well-counters, thus avoiding the purchase of many ^3He tubes with a single usage in mind.

1.1 Digital techniques

The main advantages proposed in this paper for changing to digital processing techniques in neutron NDA instrumentation for safeguards are as follows:

1. elimination of noise spikes returning to the pre-amplifier input and generated by TTL digital output signals from another electronics chain. Low-voltage differential signal lines (M-LVDS Standard) can be an alternative to single ended TTL logic;

2. reduction of the dead-time, and possibly improved detection of pile-up pulses;
3. recording of both the timestamp and the energy information of a radiation detection event. The added energy information can help discriminate high-energy events, for example caused by cosmic radiation or unwanted ionisation;
4. if compatibility with existing instrumentation needs to be maintained, a TTL output pulse can be generated at the same time the timestamp is computed.

1.2 Time digitisers for neutron counting applications in safeguards

Neutron coincidence counting is the reference NDA technique used in nuclear safeguards to measure the mass of nuclear material in samples. Most neutron counting systems are based on the original shift register technology. The analogue signal from the ^3He tubes is processed by a charge amplifier/discriminator producing a train of TTL digital pulses that are fed into an electronics unit which records frequency distributions of neutron detections in short time intervals. In recent years many research laboratories have instead produced the frequency distributions based on software-based analysis of timestamps of detection events. For this purpose, so-called list-mode acquisition devices produce the list of timestamps. Standard laptops or desktop computers (PCs) are often seen that utilise external acquisition boards based on FPGA technology, providing a timestamp for every incoming digital signal. The acquisition can be performed at high data rates utilising the ubiquitous Universal Serial Buses (USB 2.0 or USB 3.0) for transfers to the host PC with typical data throughput in the order of 40 MB/s and 300 MB/s, respectively.

The timestamps of a given measurement are often saved to storage devices. This has the advantage that measurement data can be reanalysed with different parameter values, such as gate pre-delay and gate width. Other useful diagnostics information such as die-away time, dead-time, performance of individual electronics chains, and eventually electronics noise can be filtered from the original data stream. The diagnostics information can be extracted from this stored data, or even in real-time under certain circumstances.

At JRC, two models of the Time Digitizers for Safeguards (models TDS8 and TDS32) were developed with the timestamp features described above. The TDS8 and TDS32 are shown in Figure 1. The devices record the arrival time of digital pulses with a 10 ns resolution, and feature 8 or 32 input channels respectively. Also, the channel number is recorded for each event. Data are transferred to a host PC over USB 2.0 or USB 3.0 data links. The data throughputs are 38 MB/s and 300 MB/s respectively. The devices are housed in a small extruded aluminium enclosure and in

a standard 19-inch rack 1U enclosure respectively. Other features include powering over USB (TDS8) and front panel Light Emitting Diodes (LED) for each input line, allowing the user to observe the incoming pulses on individual channels (TDS32). A signal output on the rear panel is the sum of all input channels, and can be routed, for example, to a standard shift register analyser for comparison and/or test purposes. In both devices the recorded events are written into a dual-port memory block in the FPGA. Dual-port memories guarantee independence between the processes of writing and reading data simultaneously. Decoupling the data producer and data consumer allows a simpler but very efficient hardware/firmware design.

A state machine, evolving through several states (IDLE, WRITE _ START _ RECORD, WAIT FOR PULSE, WRITE _ PULSE _ EVENT, WRITE _ ROLLOVER _ EVENT and WRITE _ STOP _ RECORD) transfers into dual port memory the time of arrival of the TTL or LVTL signal on individual input channels.

The TDS8 uses a timestamp of 32 bits, so a roll-over event happens every 42.795 s, while the TDS32 uses timestamps of 29 bits, giving roll-over events every $(2^{29}-1 \times 10\text{ns})$ equals 5.185 s. The generation of a roll-over event allows arrival times to be measured in absolute time.

A Wishbone System-on-Chip (SoC) bus [3] makes data available to the host PC using a buffered USB transmission.

The usefulness of list-mode devices such as the TDS8 and TDS32 is shown in Table 1 and Table 2, where data records from a neutron background measurement are examined. The examples show bursts of noise in a 2 us coincidence window either from a single channel or on multiple channels.

Table 1 shows the timestamps of TTL events on channel No 4 within several hundred nanoseconds. Knowing that events from neutron detections cannot appear so close on a single channel, the last two events are removed in the diagnostic analysis.

Table 2 gives an example of a burst of 10 false signals likely caused by sporadic electromagnetic noise. Such events happen occasionally in large detection systems. Note, for example, that the second timestamp represents three signals observed on different channels in the same 10 ns clock step.

A simple OR circuit performs well for background measurements and other low count rate applications. At high count rates, however, summing of OR-gated signals

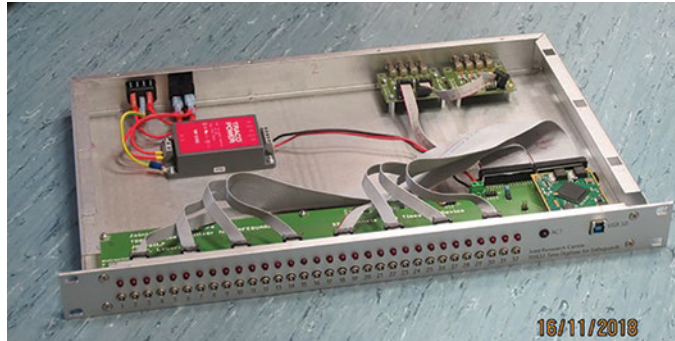


Figure 1: The TDS8 and TDS32 list-mode devices developed at JRC, one with 8 front panel inputs, the other with 32.

Channel number	Bit encoded channels	Timestamp
CH4	0b00000100	0[d] 0[h] 8[min] 25[s] 704[ms] 116[us] 540[ns]
CH4	0b00000100	0[d] 0[h] 8[min] 25[s] 704[ms] 117[us] 360[ns]
CH4	0b00000100	0[d] 0[h] 8[min] 25[s] 704[ms] 118[us] 140[ns]

Table 1: Example of noise detected on one channel (from TDS8).

Channel number	Bit encoded channels	Timestamp
CH15	0b00000000000000000000000000000000	0[d] 7[h] 29[min] 32[s] 866[ms] 820[us] 100[ns]
CH14,CH16,CH18	0b000000000000000010101000000000000	0[d] 7[h] 29[min] 32[s] 866[ms] 820[us] 160[ns]
CH17	0b00000000000000001000000000000000	0[d] 7[h] 29[min] 32[s] 866[ms] 820[us] 220[ns]
CH11	0b00000000000000000000000000000000	0[d] 7[h] 29[min] 32[s] 866[ms] 820[us] 280[ns]
CH19,20	0b00000000000011000000000000000000	0[d] 7[h] 29[min] 32[s] 866[ms] 820[us] 520[ns]
CH12	0b00000000000000000000000000000000	0[d] 7[h] 29[min] 32[s] 866[ms] 820[us] 600[ns]
CH3	0b00000000000000000000000000000000100	0[d] 7[h] 29[min] 32[s] 866[ms] 820[us] 720[ns]
CH9	0b00000000000000000000000000000000100000000	0[d] 7[h] 29[min] 32[s] 866[ms] 822[us] 40[ns]

Table 2: Example of a burst of electromagnetic noise recorded by TDS32 from a multichannel passive neutron counting system.

results in coincident or near-coincident events being lost in the process. The number of lost signals increases with the count rate.

For high count rate purposes, a digital mixer has been added to the TDS32 device. In this context we define a mixer as a circuitry with a de-randomiser on each input line and a buffer for recording the content of all input lines. A synchronous priority encoder is then used to output the buffer content on a single output line without the loss of the incoming signals. An output clock of 12.5 MHz has been adopted in order to output signals with a width of 40 ns. In this way the minimum distance between signals remains 80 ns. Because only the presence of signals is needed at this stage, a proper first-in-first-out (FIFO) is not necessary. Only read and write event-pointers are needed to advance the ‘virtual FIFO’ and to record the signal arrivals. An output signal is produced when the read pointer reaches the write-pointer in accordance with the following rules:

1. the read-pointer must be less than or equal to the write pointer, except for the condition outlined by the second rule. This means that a read operation normally follows a write operation as soon as the read has been enabled, i.e. when the priority encoder is freed from processing signals;
2. the read-pointer can only be greater than the write-pointer when a roll-over of pointers has occurred due to the limited size of the buffer. In this case the virtual FIFO must be sequentially emptied;
3. the virtual FIFO must not be read faster than the 12.5 MHz output clock rate. This condition is necessary to avoid the output of two signals instead of one while the priority encoder is busy.

Modulo 32 (5-bit) Gray code counters have been implemented but used as modulo 16 (4-bit) counters, the most significant bit being used to indicate pointer

‘wrap-arounds’. For this reason, only 16 FIFO slots are available on each individual line. Gray code counters exhibit an improved read-out error code with respect to binary counters, because only 1-bit transitions can happen between adjacent words. Bursts of electrical noise, such as the ones detected by the post-processing analysis of the pulse train (Tables 1 and 2), can also be eliminated by including filters in the mixer FPGA fabric. A simple inhibit gate on each individual line can eliminate for example situations depicted in Table 1, but not in Table 2.

This kind of real-time filtering should be performed only at low count rates or in background measurements in order to avoid removing real signals.

1.3 Signal digitiser for safeguards

At JRC we are currently in the process of developing an analogue signal digitiser to substitute the standard signal amplifier used in neutron counting instrumentation for safeguards. The signal digitiser will have eight analogue signal input lines intended for pre-amplifier signals from gas proportional counters. The main benefits of this prototype compared to the standard analogue front-end electronics are expected to be:

- reduced updating dead-time on each signal line;
- improved discrimination of pile-up events.

The digitiser will process the analogue charge pre-amplifier output with the characteristic long exponential decay by means of a Moving Window Deconvolution (MWD) and a ‘feature extraction algorithm’ (FEA). The algorithms are currently being tested in our laboratory. The hardware is expected to be operational by the end of 2019.

A larger version featuring up to 128 channels to be housed inside a detector head is the final goal. In this way a single optical USB cable from the detector eliminates the complex wirings of multiple coaxial cables normally interfacing a neutron detector head to a signal analyser.

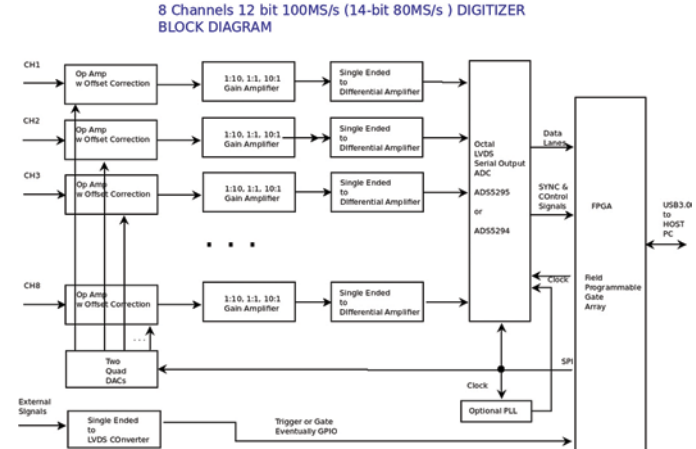
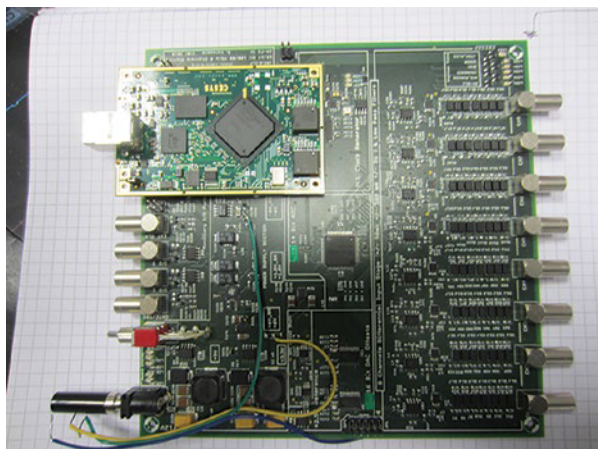


Figure 2: The prototype signal digitiser board and corresponding block diagram.

The hardware is enclosed in an extruded aluminium box (170 mm × 163 mm × 51.5 mm) with the following characteristics:

- sampling rate up to 100 MS/s (ADS5295) and 80 MS/s (ADS5294), depending on chipset;
- 12-bit (ADS5295) or 14-bit (ADS5294) resolution;
- 8 channels, DC coupled, fixed input impedance: moderately high impedance ($k\Omega$) or 50Ω ;
- trigger options: internal (software or driven by channel(s) criteria) or external (TTL logic levels);
- gate: external TTL signal;
- clock options: internal or external;
- digitally controlled gain, in principle settable independently for each channel (the current version uses the same gain for all channels to simplify the board design on a 4 layers PCB);
- input sensitivity covers the range from ± 50 mV (100 mVpp), ± 500 mV (1 Vpp), ± 5 V (10 Vpp) for ADC full scale;
- 50 (40) MHz analogue bandwidth, anti-aliasing LC filter included. Coefficients for low-pass filters can also be uploaded to the ADC registers.

2. Digital filter using Moving Window Deconvolution and feature extraction algorithm

The MWD algorithm, see Georgiev, Gast and Lieder [2], consists in a technique to determine a value proportional to the step amplitude of an exponential decaying signal (the output of a charge pre-amplifier) by looking at the sequence of values of the signal at successive time intervals. The values evidently contain an indication of the step value

A assumed at $t = 0$. In the continuous time domain, an exponential signal is defined as:

$$y(t) = \begin{cases} Ae^{\frac{-t}{\tau}} & t \geq 0 \\ 0 & t < 0 \end{cases} \quad (1)$$

To determine the step amplitude (A), we define a function $f(t) = A$.

A term $y(t)$ is added and subtracted:

$$f(t) = y(t) + A - y(t) \quad (2)$$

Then inserting the definition of the exponentially decaying function, the equation reads:

$$f(t) = y(t) + A \left(1 - e^{\frac{-t}{\tau}} \right) \quad (3)$$

By applying the fundamental theorem of integral calculus and using a variable substitution $u = \frac{t}{\tau}$, because

$$\tau \int_0^t e^{-u} du = -\tau e^{-u} \Big|_0^t = \tau \left(1 - e^{\left(\frac{-t}{\tau} \right)} \right) \quad (4)$$

we get:

$$f(t) = y(t) + \frac{1}{\tau} \int_0^t y(u) du \quad (5)$$

The sum can be extended to $-\infty$ because the signal is a null function for $t < 0$.

In the time domain this corresponds to a step function, i.e. the response of an ideal integrator.

To avoid the saturation of a real pre-amplifier, a continuous discharge is applied by a resistor in parallel to the integrating capacitor, so that the exponential response of the real

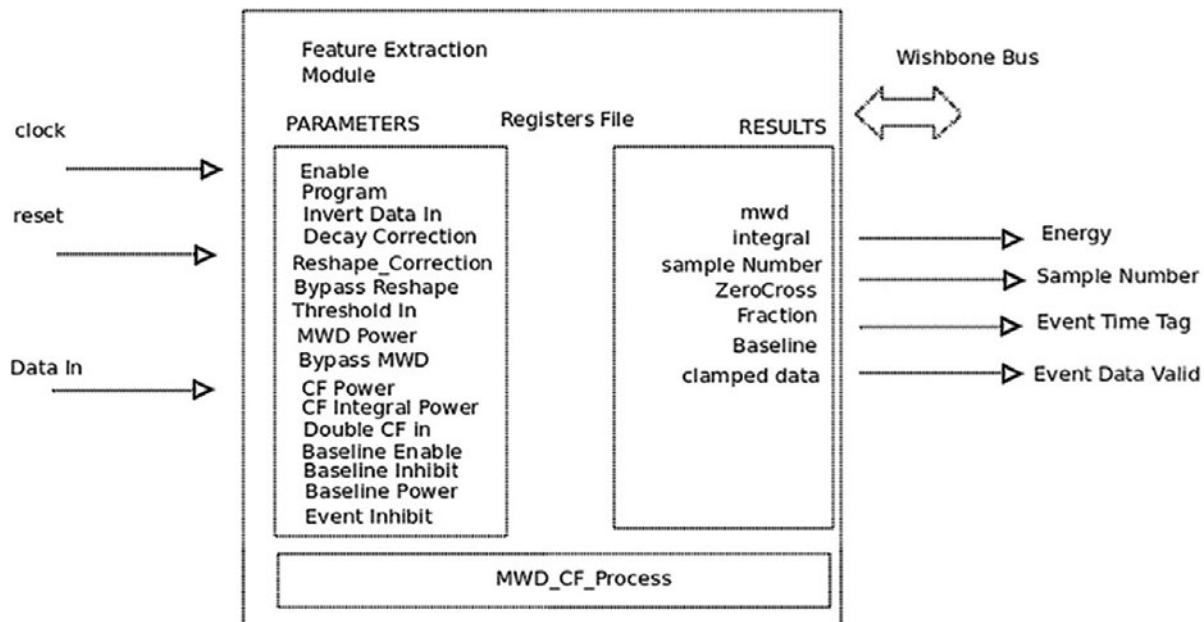


Figure 3: Block diagram in VHDL.

filter is deconvoluted to a step function. In the discrete time domain the integral becomes a sum, also extensible to $-\infty$:

$$A(n) = x(n) + \frac{\Delta}{\tau} \sum_{k=0}^{n-1} x(k) \quad \text{where } \Delta = \frac{1}{\text{sampling}_\text{rate}} \quad (6)$$

which can also be expressed as a recursion:

$$A(n) = x(n) - \left(1 - \left(\frac{1}{\tau}\right)\right)x(n-1) + A(n-1) \quad (7)$$

Equation 5 is differentiated (in discrete time) because we are interested only in the amplitude step of the signal from the radiation detector, we get:

$$\begin{aligned} MWD(n) &= A(n) - A(n-M) = \\ &x(n) - x(n-M) + \frac{\Delta}{\tau} \sum_{k=n-M}^{n-1} x(k) \end{aligned} \quad (8)$$

The MWD can be seen as a composition of two elementary blocks: Delay and Subtract (DS), and Moving Average (MA). The DS block takes the amplitude difference at two sampling points which are M sampling intervals apart $y[n] = (x[n] - x[n-M])$. M is the MWD differentiation filter length. The value of M can be taken as an integer power-of-two in order to easily implement a fast binary division.

2.1 Algorithm implementation

The block diagram of the algorithm as implemented in Very High Speed Integrated Circuits Hardware Description Language (VHDL) code is presented in Figure 3.

The top level block of the MWD filter dialogues with the external world using a Wishbone bus interface [3]. Several registers are available to the user in order to store

parameters and constant values for controlling the algorithm. The module outputs are:

- a timestamp indicating when step value A is recognised;
- the corresponding energy (step height);
- an indication of the validity of the data recorded.

The main registers to control the behaviour of the algorithm are:

- decay and reshape correction;
- MWD power (of 2) to give a length (M);
- cross fraction power (division by $\frac{1}{4}$ or $\frac{1}{2}$) and cross fraction integral power (of 2) length of pipeline;
- baseline power (of 2) so pipeline length;
- baseline inhibit and enable bits;
- event detect inhibit or enable;
- threshold input.

Details of the top-level diagram are given in Figure 4.

The ADC input data, or an inverted value representation, become the input of the programmable MWD module, which can optionally be bypassed. The data can become an input for a shaper module, which may also be bypassed. Following the MWD and shaper blocks, a further, more complex features extraction block follows in Figure 5. Implementing a MWD, consisting of a DS block and an MA block, is an easy task. The features extraction module, however, is not easily implemented. The latter module has been edited and adapted from a remarkable open source code [4-7].

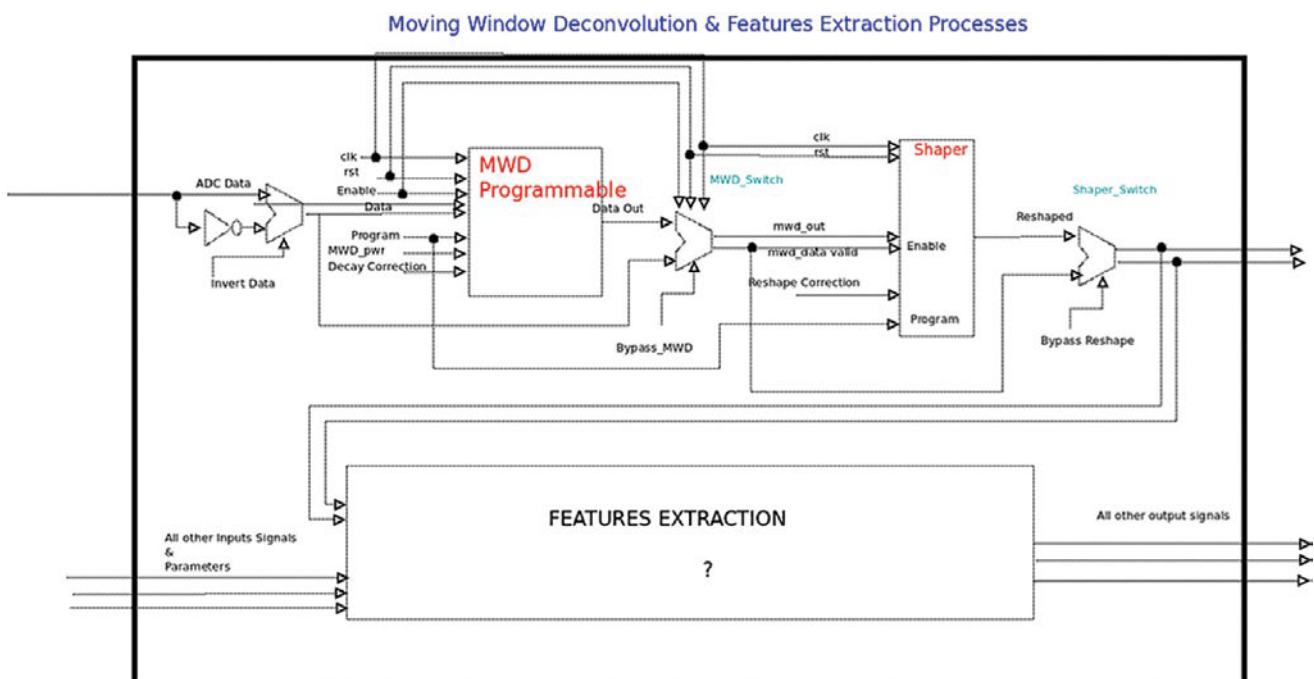


Figure 4: MWD and shaper block diagram.

The MWD logic consists of the moving sum and difference blocks. Fixed point arithmetic operations can be performed easily. However, the normalisation constant $\frac{\Delta}{\tau}$, expressed in units of the ADC sampling period $T = 10$ ns, is a real number (<1). A typical value is 1/14000 for the Crema CR110 preamplifier decay constant of 140 μ s. In order to make the FPGA implementation of the MWD filter algorithm possible, the normalisation constant is multiplied by an arbitrarily large power-of-two value, and after the multiplication operation the result is divided by the same factor.

2.1.1 Moving Sum or Moving Average (MA)

The MA entity is a basic building block for the MWD, and in general also for FEA. The block is composed of an accumulator register, an adder/subtractor and a delay line. The accumulator contains the sum of the delay-line elements. Each value coming out of the delay line is subtracted from the accumulator. After an initial delay, an averaged value is output at each clock-tick (10ns). It is straightforward to divide (shift right operation) by N if the delay line length (N) is a power of two.

2.1.2 The Features Extraction Algorithm (FEA)

A clamped data signal is obtained from the signal coming out of the previous MWD block and from the signal baseline information, which must be taken into account and subtracted from the input data. Of course, the baseline

computation must be disabled during the energy pulse duration interval, otherwise a false value for the baseline would be obtained. In order to compute the energy and timestamp information of step value A, a trigger signal must be determined at the same time.

The features extraction module (Figure 5) contains several blocks which compute different information more or less simultaneously using delayed pipelines, just to get information at a later time after other events have been already detected. In this way the algorithms can be executed in parallel, and global information can be figured out after a delay when a final trigger signal is generated. The algorithm can be run continuously, and is triggerless because the trigger is extracted from incoming data.

A constant-fraction discrimination (CFD) module is used as a preferred choice with respect to the simpler leading-edge discriminator. The CFD entity is implemented by subtracting a delayed copy of the clamped signal, which has been scaled (values are divided by two or four for the sake of simplicity and implementation). The obtained CFD signal has a zero-crossing timing independent of the shape and rise time of the clamped signal. After detection of the zero-crossing a trigger is sent to the event detection module.

An event is detected when an area of the pulse is above the set threshold. The area is computed by means of a trapezoidal filter: another MA module which computes

Features Extraction Process

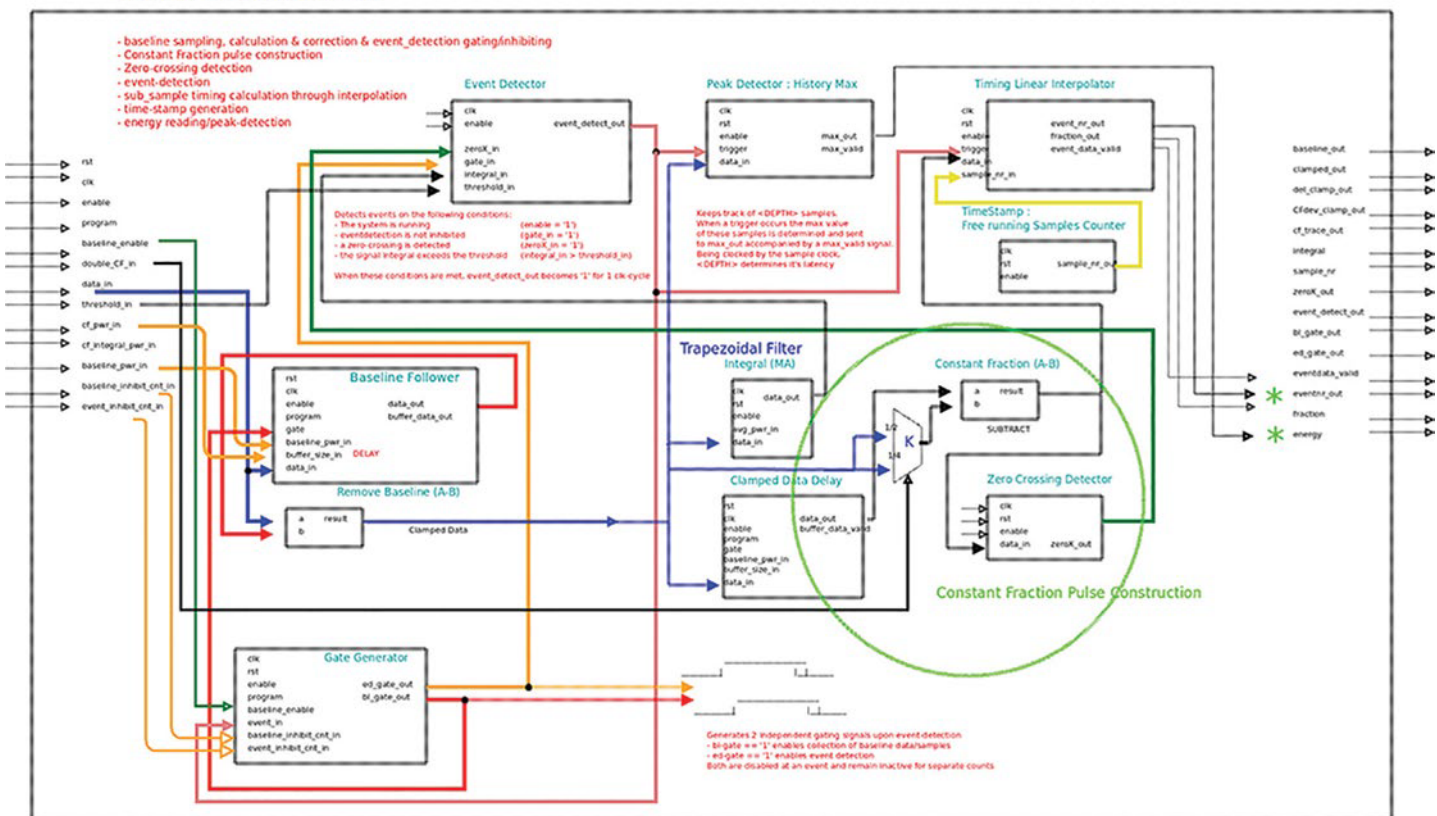


Figure 5: Feature extraction module.

averaged values of the flat top portion of the pulse (as seen in Figure 8). In order to detect the highest pulse level, which is contaminated by noise, a pulse detector is implemented by collecting a limited history of input signals. A timestamp is generated by means of a free running counter, and read upon arrival of the trigger signal. A linear interpolation is then used to determine a less arbitrary and more precise timestamp value. The zero-crossing indication is obtained by a simple algorithm which looks at a sequence of consecutive ‘one negative and two positive’ values. The time information is between two samples. A linear interpolation of four, eight or more interpolated points can give an even better approximated value.

Parametric values are set up by the user by means of several registers (see Figure 3) in order to fine-tune the behaviour and performance of the algorithm.

2.1.3 Simulations

Figures 6 to 8 below are the results of simulations performed using an open-source hardware description language simulator. The analogue signals are

a representation of digital values which, if represented only as numerical values, would have been less expressive of the dynamics of the signals.

The results of the MWD and the FEA are shown below.

Figure 6 shows an input signal which is a superposition of the exponential decaying waveform with a 140 us decay time (simulated pre-amplifier pulse). After the third step the noise level has been increased on purpose to generate a false detection of a timestamp and a corresponding energy value.

After having changed the threshold parameter (Figure 7), the false pulse in Figure 6 has been discarded. This means that tuning the digital algorithm can be as simple and effective as an analogue threshold discrimination circuit.

In Figure 8 a series of nearby pile-up events have been simulated. Pulses were correctly discriminated by the MWD FEA; timestamp and energy information have been generated.

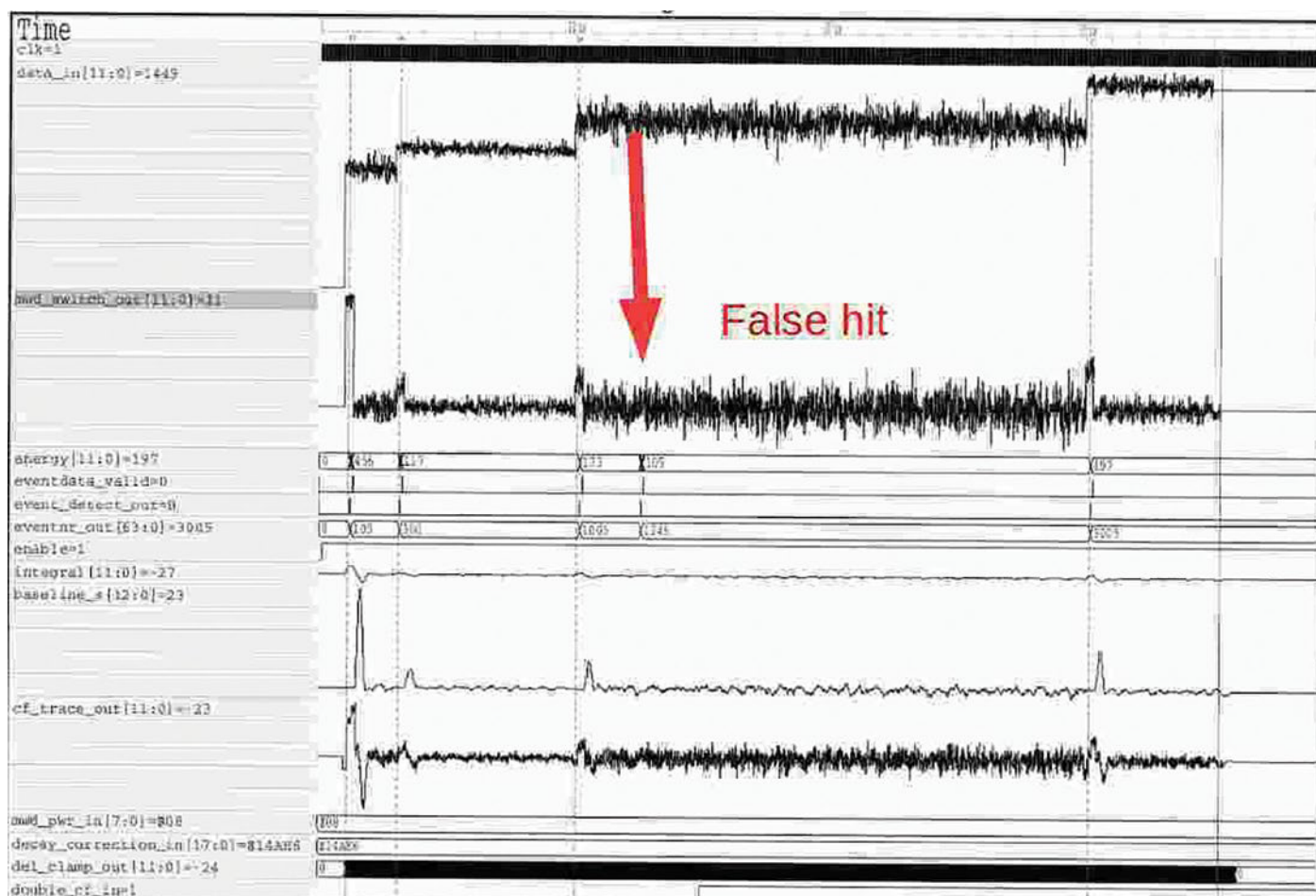


Figure 6: Simulation result No 1.

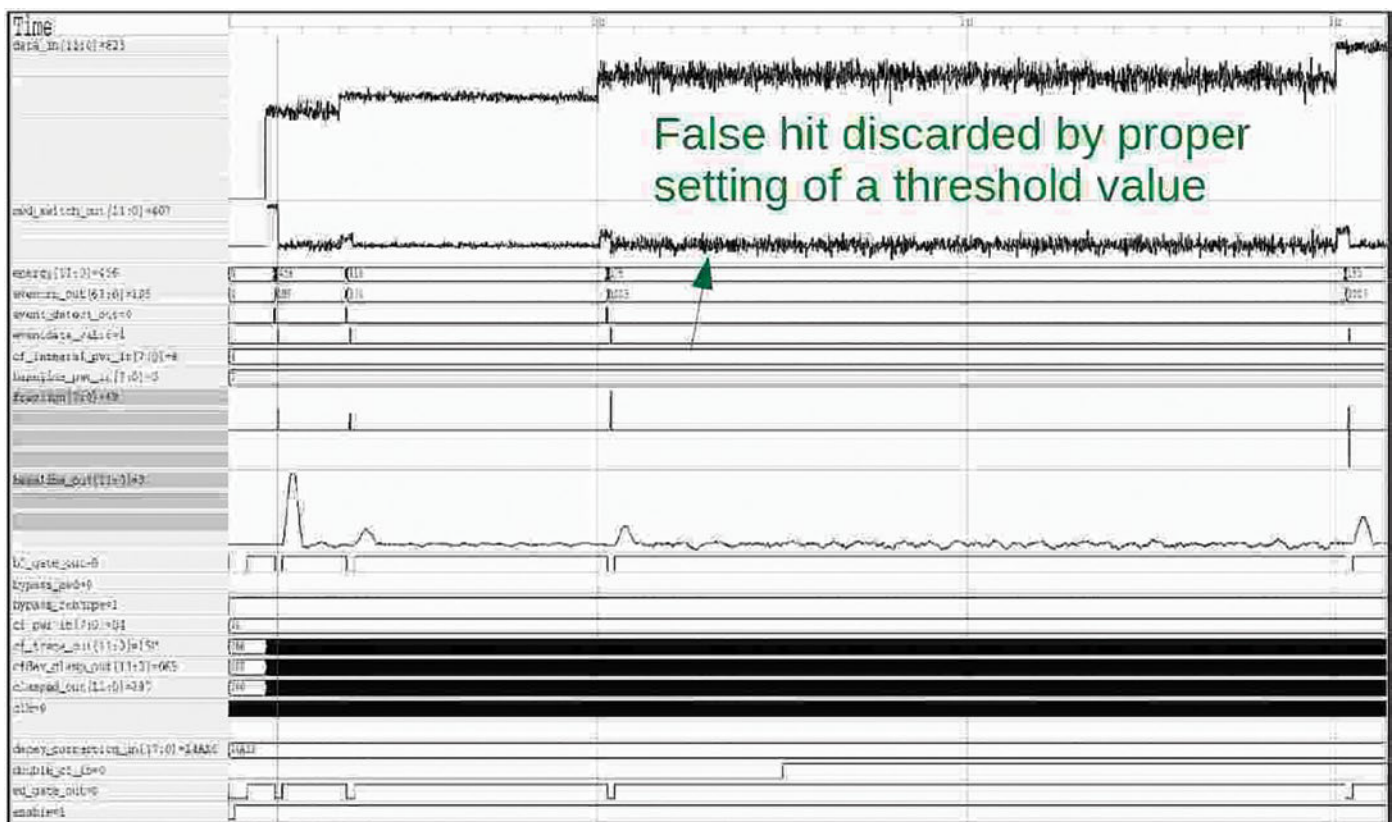


Figure 7: Simulation result No. 2.

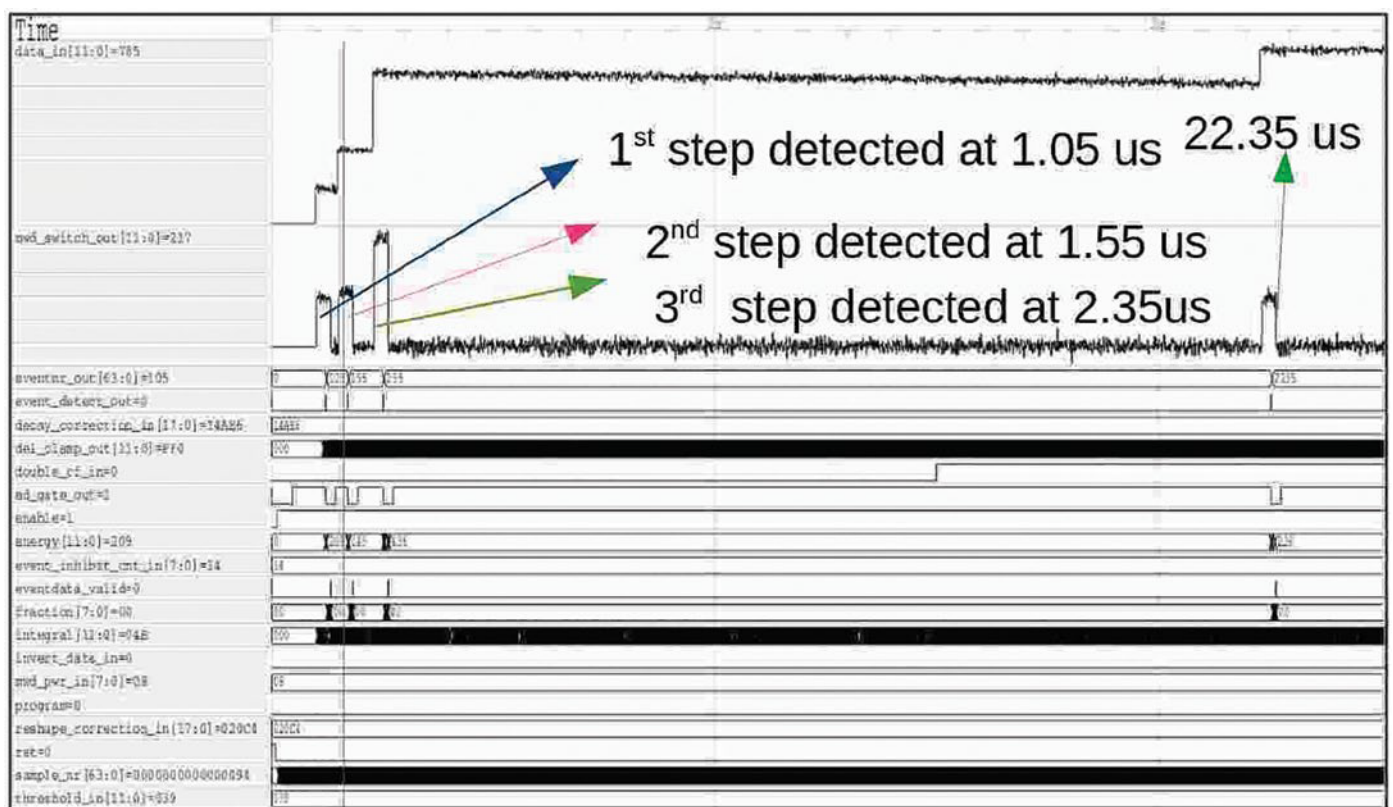


Figure 8: Simulation result No. 3.

3. Conclusion

At JRC we are working to improve the electronics chain in neutron counting systems for safeguards. This concerns all the steps from the charge collection pre-amplifier connected to neutron sensitive gas proportional counters to the measured frequency distributions of neutron detection events, as used typically in well-counters for neutron multiplicity counting.

We have presented elements of noise suppression methods used in the development of new pre-amplifiers/amplifier circuits. Also, the new list-mode devices developed at JRC to substitute the standard shift register analysers have been presented, and the data elaboration and diagnostics possible in these devices have been discussed. The main focus, however, was on the ongoing development of digitiser circuits we propose for replacing the traditional signal amplifier and digital signal formation following a neutron-detection event. The advantages of the digital approach are expected to be, first of all, better dead-time performance and pile-up rejection, but also much improved system diagnostics and lower costs. Tests are ongoing on a prototype digitiser board with eight input lines. The promising simulations show the feasibility of implementation, what is basically a digital filter, with potential for the substitution of the widely used analogue methods for neutron-pulse processing in safeguards.

An added advantage of the digital approach derives from the entire signal processing being completely parallelised starting from the single ${}^3\text{He}$ detector tube until the final step of data analysis. This offers the possibility that individual ${}^3\text{He}$ detectors can be moved between detector heads without affecting the electronics design, provided that the neutron-detection heads are purposely designed for easy removal of the tubes. A better utilisation of the ${}^3\text{He}$ tubes in this fashion could alleviate the present shortage of ${}^3\text{He}$.

4. References

- [1] National Semiconductor, *LVDS Owner's Manual*, fourth edition, 2008.
- [2] Georgiev, A., Gast, W. and Lieder, R. M., 'An analog-to-digital conversion based on a moving window deconvolution', *IEEE Transactions on Nuclear Science*, Vol. 41, No 4, 1994, pp. 1116-1124.
- [3] Wishbone B4, Wishbone System-on-Chip (SoC) Interconnection Architecture for Portable IP Cores (<http://www.opencores.org>).
- [4] Lemmnes, P. and Kavatsyuk, M., 'General-purpose pulse-processing algorithm' (http://opencores.org/project.pulse_processing_algorithm).
- [5] Gulyev, E., Kavatsyuk, M., Lemmens, P. J. J., Tambave, G. and Löhner, H., 'VHDL implementation of feature-extraction algorithm for the PANDA electromagnetic calorimeter', *Nuclear Instruments and Methods in Physics Research Section A*, Vol. 664, 2012, pp. 22-28.
- [6] Gulyev, E., 'Verification of a novel calorimeter concept for studies of charmonium states', University of Groningen, 2011.
- [7] Kavatsyuk, M., Gulyev, E., Lemmens, P. J., Löhner, H. and Tambave, G., 'Digital signal processing in the PANDA electromagnetic calorimeter for the Panda collaboration', KVI, University of Groningen, Groningen.
- [8] Graham, H. and Johnson, H., *High-speed Digital Design: A handbook of black magic*, Prentice Hall, Upper Saddle River, 1993.

Nuclear forensics via the electronic properties of particulate and samples

Robert B. Hayes, Ryan P. O'Mara, Fatma Abdelrahman

North Carolina State University, Nuclear Engineering Department
2500 Stinson Dr, Raleigh NC, 27695-7909
rbhayes@ncsu.edu

Abstract:

Recent research has shown how solid state dosimetry techniques can be used as a powerful tool in nuclear treaty verification. Using thermoluminescence, it has been shown that common bricks can serve as gamma ray spectrometers with 10% energy resolution for ^{241}Am [1]. Using optically stimulated luminescence (OSL), it has been shown that ^{137}Cs and ^{60}Co can be identified and imaged again using common bricks [2]. Likewise, surface mount resistors (such as in portable memory flash drives, credit cards or other electronics) are capable of recording dose approaching common background levels using these techniques [3]. Even imaging of weapons grade plutonium has now been accomplished using OSL; the extent to which this can be accomplished using the mineral particulate from smears and air filters is yet to be explored. Now that the theory has been worked out to use this science to carry out retrospective assay of uranium enrichment, the various applications for treaty verification are almost unbounded including retrospective assay of historical uranium enrichment [4]. Applications using electron paramagnetic resonance (EPR) have shown great promise [5] but new options will be explored here. This technology effectively puts low resolution imaging gamma ray spectrometers in every inhabited location on the planet throughout all time as insulator samples are ubiquitous in building materials, personal items and electrical circuit peripherals.

Keywords: Solid state dosimetry; Nuclear Forensics; Nuclear Safeguards; Luminescence; Magnetic resonance

1. Introduction

The main goal in nuclear forensics is to characterize radiological material with regards to its isotopic composition, provenance, age and/or history. The conventional tools applied within this field of study generally require direct access to the source material of interest, or remnants of that material. However, the ability to perform forensic analysis at a distance, whether spatially or temporally, would provide an attractive toolset for both nuclear nonproliferation and safeguards applications. The purpose of this work is to illustrate how solid state dosimetry (SSD) of small samples may soon allow for retrospective nuclear forensics analysis using commonly disregarded mineral material.

The principle mechanism in SSD is charge trapping by lattice defects in crystalline insulator materials. During irradiation, electrons liberated from atomic bonds may become trapped at lattice defect sites such that the population of trapped charges is proportional to the radiation dose received. Once trapped and in the absence of additional stimulation, the populations of trapped charges will be stable over very long periods of time. To the extent that the populations of trapped charges can be quantified and the dose response for the crystalline material can be characterized, then the dose to the material can be reconstructed. The ability to determine the doses received by crystalline materials allows for the possibility to characterize historical radiation environments. The two main methods used, in this work, to quantify material dose are luminescence dosimetry and electron paramagnetic resonance (EPR).

Luminescence dosimetry uses the light emitted by materials upon optical or thermal stimulation to determine the population of trapped charges in a previously irradiated material. Additionally, these methods are best suited to determining the doses to inorganic insulator materials, such as silicate or aluminum oxide ceramics. The utility of luminescence dosimetry for assaying radiological sources using ubiquitous materials has been well documented in the literature. [1-3] For example, using thermoluminescence (TL), it has been shown that common bricks can serve as gamma ray spectrometers with 10% energy discrimination for ^{241}Am at the 1 standard deviation level [1]. This is based determining the empirical mass energy absorption coefficient $\mu_{\text{en}}(E)$ from the exposure based on the measured dose depth profile in the materials. Knowing the material composition then allows determining what energy the exposure had to have to give the measured value(s) of $\mu_{\text{en}}(E)$. Using optically stimulated luminescence (OSL), it has been shown again with these methods that ^{137}Cs and ^{60}Co can be identified and imaged using common bricks [2]. Likewise, surface mount resistors (such as in portable memory flash drives, credit cards or other electronics) are capable of recording dose approaching common background levels using these techniques [3].

Electron paramagnetic resonance dosimetry uses resonant absorption of precisely tuned microwaves under an applied magnetic field to quantify the number of radiation-induced trapped charges. Unlike luminescence dosimetry methods, EPR is generally best suited for organic

insulating materials. EPR is also recognized as the gold standard for epidemiological dose reconstruction for populations exposed to anthropogenic external radiological sources [4]. Previous work with sucrose crystals has demonstrated detection limits ranging from 500 mGy [5,6] up to 1.5 Gy [7,8] to list a short sample from multiple studies.

By utilizing a combination of EPR and thermoluminescence dosimetry, it should be possible to characterize historic radiation environments in nearly every corner of the developed world. Additionally, extending these techniques to small sample sizes would allow for forensics analysis using particulate material fortuitously collected during routine air and smear sampling. For example, plume modelling can be used to reconstruct historical releases by distant nuclear facilities [10]. If the aerosolized particulates in such a release are composed of nonconducting materials, then these particles can in principle be used as dosimeters with solid state techniques such as luminescence and EPR. While current techniques focus only on chemical and isotopic signatures in such samples with the added potential to conduct morphological analysis, dosimetric analyses could be performed on the particulate matter that is generally discarded. Recent work has explored this potential to use ubiquitous dust particulate from smears and air filters as common dosimeters via luminescent techniques [11].

In the case of luminescence dosimetry, it has been shown in the literature that using specialized instrumentation and measurement protocols accurate dosimetric reconstructions can be performed on particulate matter the size of a single grain of sand. [12] Such sample sizes are what one might expect to collect on an air filter or environmental smear. Similarly, using sophisticated sample measurements protocols our technique allows precision of a few percent with tooth enamel [13] or alanine [14] which has been shown to improve detection limits by an order of magnitude over traditional techniques [15].

1.1 Complementary Techniques

As with any detector modality, the detection limit depends on background signal amplitudes. When using EPR and luminescent techniques, the background typically depends on sample age and its inherent solid state chemistry. This latter component will affect sensitivity, signal stability and even native interfering signals, which can include sample preparation effects.

While luminescence dosimetry has proven useful for dosimetric measurements on particulate matter, the ability to perform single grain EPR measurements remains to be demonstrated. For EPR, the decision limit for any dose is dependent on the minimum detectable spin density of the spectrometer system [16]. Under ideal conditions, the minimum detectable number of spins for a commercial X-band spectrometer is approximately 10^{12} [16]. Since the spin density in the sample is proportional to the radiation dose

received, it is likely that EPR dosimetry on small particulate samples would be relegated to only those samples with large doses. However, since many organic insulating materials tend to have very large saturation doses small aliquot EPR dosimetry may still be a viable option [17].

Most luminescence materials have a drastic light attenuation property such that exposure to ambient sources will cause the signal to decay drastically (having half lives on the order of hours) [18]. Consequently, for luminescence dosimetry analysis, environmental samples would ideally be collected from locations shielded from ambient light sources, such as underneath painted surfaces. Organic insulators often are not subject to the same light sensitivity and so may offer a more robust approach to scavenging dosimetric information from air samples and smears.

Despite the potential challenges inherent to luminescence dosimetry or EPR dosimetry, it is proposed here that having access to both will allow for robust characterization of historical radiation environments using scavenged materials.

2. Example Results

Given the intractable number of materials which are insulators to any extent, the literature reviews on common examples should be consulted for specific types if they have been evaluated [13,14]. A few new examples of potential interest in nuclear forensics carried out in our lab will be offered here but the full range of possibilities is expectedly yet to be explored.

The typical approach in solid state dosimetry techniques is to measure the initial dosimetric signal and then via subsequent irradiation to determine the sample sensitivity to radiation and so back extrapolate to the initial dose obtained by the sample prior to laboratory measurement. If the initial signal is measured as Si and then the sensitivity is signal intensity per dose given by the symbol S/IpD , then the sample dose estimate is easily obtained by the ratio $Si / S/IpD$. More generally this is done by additive irradiations where the subsequent measurements follow a linear trend, which is least squares fit, to back extrapolate to the initial dose.

2.1 Combined TL/OSL and EPR

Typical experimental configurations have been given elsewhere for luminescent and EPR parameters [18,19]. An example of the luminescent and EPR results from diatomaceous earth are shown in Figures 1 and 2 respectively [20]. The fit parameters from Figure 1 are given in Table 1. Note that when dose values become large (which is materially dependent), then the dose response is no longer linear but follows a saturating exponential profile as seen in figure 3. Here, the results were shown to be fairly insensitive to luminescence methods but offered the hope of new EPR properties very different from geological quartz samples.

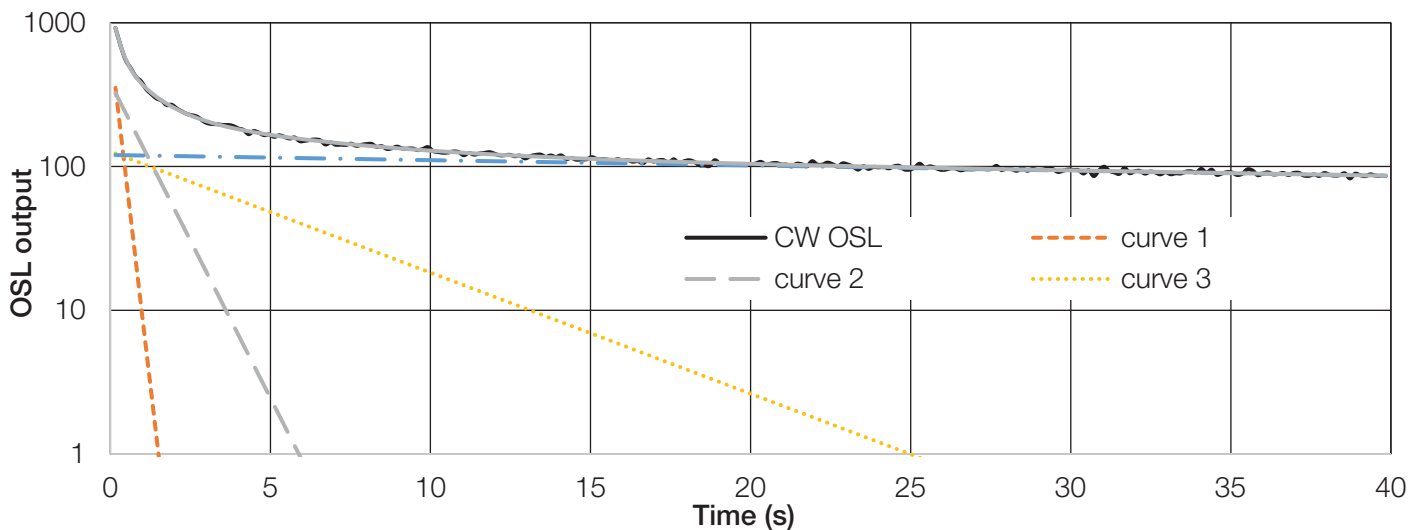


Figure 1: Deconvolved OSL spectrum from diatomaceous earth [20] where the measured signal is the continuous wave OSL (CW OSL) with fit parameters provided in Table 1. Note that the ordinate axis is logarithmic so all the fits are simple exponential decay curves.

Curve #	A amplitude parameter	A amplitude uncertainty	λ decay parameter	λ decay uncertainty
1	709	29	4.36	0.23
2	382	20	1.01	0.071
3	127.1	8.5	0.194	0.016
4	120.2	2.7	0.00834	0.00068

Table 1: Curve fit parameters from Figure 1 using the exponential model for each fit parameter being given by the functional form of $f(t) = Ae^{-\lambda t}$, where A is the amplitude parameter and λ is the decay parameter.

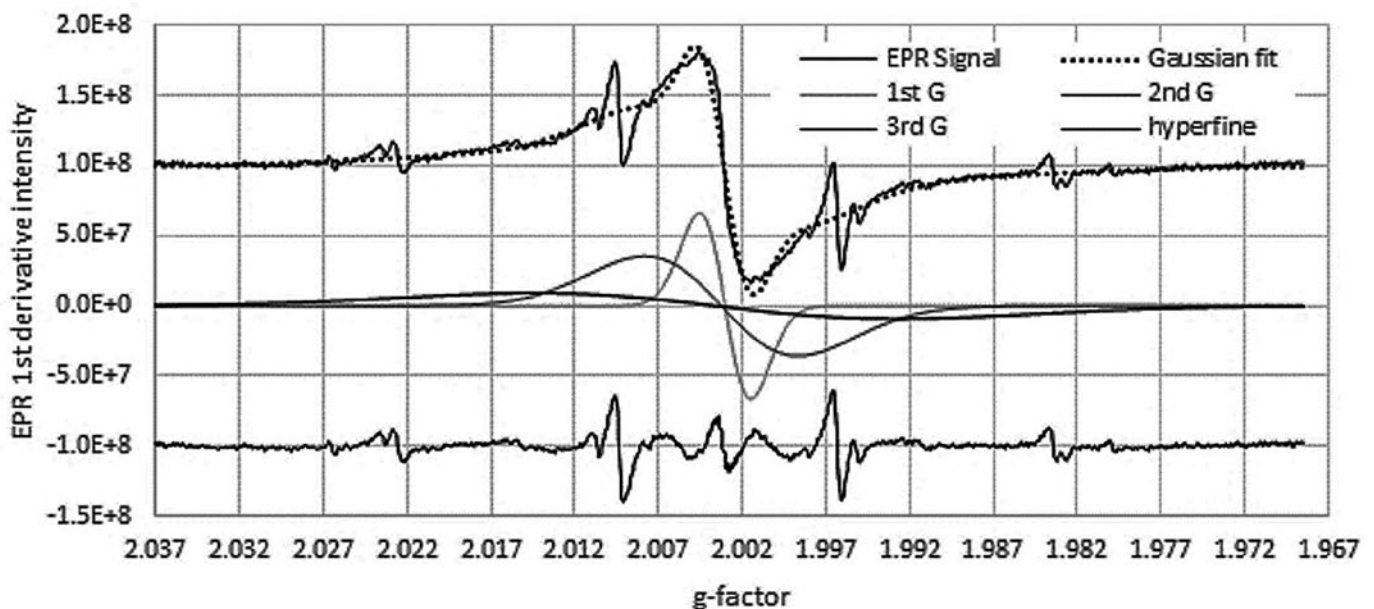


Figure 2: Deconvolved EPR spectrum from diatomaceous earth [20]. Various Gaussian components are deconvolved and shown in the central set being listed as 1st G, 2nd G and 3rd G, respectively. The residual unresolved spectral components are shown at the bottom as the hyperfine portion of the signal.

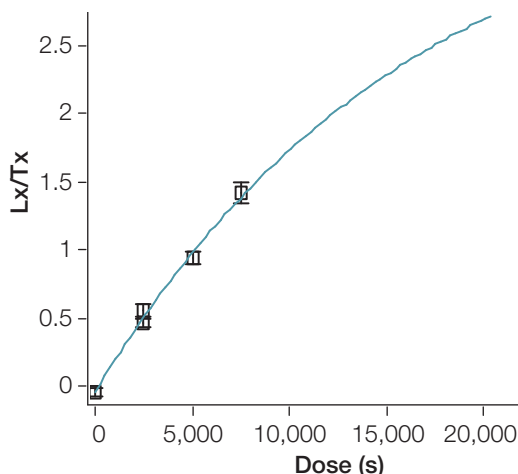


Figure 3: Example saturating exponential dose response shown as a function of additional exposure time in seconds. The functional form when trap centers are approaching maximum population results in a dose response following the functional $f(s) = k(1 - e^{-(s-E)/D})$ where E is the resultant dose estimate, k is the maximum signal amplitude at infinite dose and D is the saturation dose.

2.2 EPR

Sucrose is known to be an excellent EPR dosimeter having high sensitivity, low detection limits and long signal stability [8]. Using the same techniques previously shown to have drastically reduced the detection limits for alanine dosimetry using EPR [15], the results from Figure 4 were obtained using 0.5 g aliquots. Here, although a goniometer was not utilized the results demonstrate an 80 mGy standard deviation of the residuals. The rest of the curve fit parameters are shown given in the inset of the figure.

A measured dose response, such as that shown in Figure 4, is still in the linear range; therefore, the sample sensitivity can be taken to be the slope of the least squares fit. Coupling such a dose response function with an initial signal intensity allows the equivalent initial dose to be determined. Although these results were not obtained using

single sucrose granules, the linearity of the dose response out to 10 Gy is promising.

The intercept in Figure 4 represents the combined native organic signal and accumulated background radiation. If the signal were purely anthropogenic, the x -intercept of 150 mGy would be the resultant dose estimate for this sample. The standard error of the fit value 0.19 EPR counts per mGy represents the 1σ level for a 0.5 g sample based on a residual analysis. Taking a single grain of sugar to be approximately 0.6 mg, then the EPR response for a single grain would be expected to be near $0.19 \times 0.6 / 500 = 0.23 \times 10^{-3}$ EPR mGy $^{-1}$. To then just approach the variation seen in Figure 4 would require around a full Gy of radiation dose. Taking into account all combined errors otherwise ignored in this estimate and going to the 95% CL, the detection limit should be many Gy for a single grain. Even if difficulties prevent detection below 10's of Gy, this would still be within the needed to linear range of the dose response to accommodate single granule dosimetry by EPR as the linear range extends to the kGy range [21].

2.3 TL/OSL

A recent development of forensic interest is the potential to use common electronic components as dosimeters at the natural background level [3] similar to that done with sugar in section 2.2. The ability to discriminate doses at the level of environmental exposures has the potential to radically implement ubiquitous sensing. As an example, it was shown in [3] that simply using multiple electrical elements in a cell phone is sufficient to carry out energy spectroscopy sufficient to discriminate low energy gamma emitters from industrial or medical source typically having higher energies.

The concept for using differential attenuation in ubiquitous materials is effectively equivalent to that already used in radiation worker dosimetry. In both TL and OSL dosimetry, 4 separate luminescent elements are used with each being able to individually measure dose. These are placed

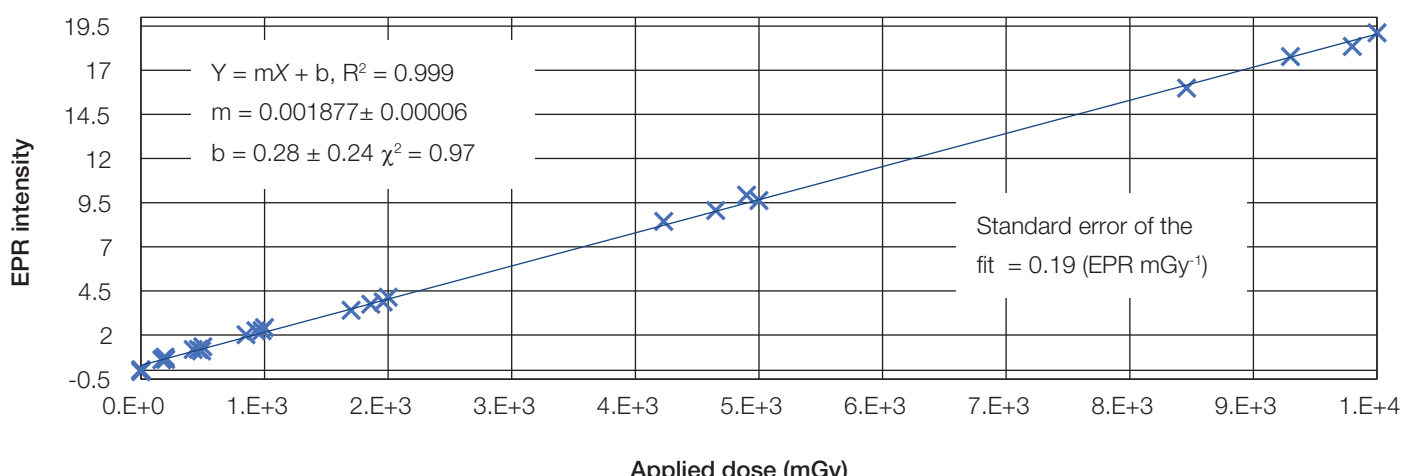


Figure 4: Dose response of commercial sugar granules using techniques initially developed for alanine EPR [13]. EPR values are shown in terms of peak to peak counts.

behind distinct attenuating materials such as tin, Mylar, copper and polyethylene (with the element behind the polyethylene being enriched in a neutron absorbing isotope). Using the resulting differential response of the 4 elements along with functional relationships among the same, algorithms can then discriminate between high energy gamma, x-ray, beta and neutron exposures allowing accurate worker dosimetry to be ascribed.

3. Analysis

The utility for developing technologies to determine historical doses to ubiquitous materials is exemplified in Figure 5. This generic bunker configuration would expectedly be under international treaty control requiring that the warheads remain in-place between successive inspections. If the entry controls are in any way spoofed, then the owner of these items could have deployed them intermediate to any treaty verification inspections. Utilizing these solid state dosimetry techniques, the dust particulate on the very walls of the bunker could determine if the ambient dose rate was consistent with the long-term placement of the warheads between successive inspections. Likewise, the bricks can provide age estimates as to whether any were new or replaced in any kind of spoofing attempt.

The application in forensics as proposed here is not a panacea of detection solutions. The measurement is only a single long-term acquisition. This means that a large dose rate source in motion (such as a spent fuel bundle) would appear as a distributed source along the path of the movement. If any imaging approach were attempted [2], then multiple samples would be required from well-defined locations.

In general, the method only provides some form of the product between dose rate and integration time (hence dose). If the time is known, then a dose rate or activity could be estimated. Conversely, if the source activity were known, then an integration time could be obtained. This in turn assumes intervening materials were known to account for shielding and scatter. Depending on operational knowledge, an upper bound may only be possible on a time window; this would then offer a lower bound on the source activity or dose rate giving rise to the resultant dose. All this of course assumes a single known, or assumed, source.

3.1 Caveats, limitations and considerations

As with any detector, SSD approaches have limitations although these vary greatly from those of electrically powered detector systems. Modern radiation detection systems have integration times ranging from seconds to days, where the integration time directly corresponds to the temporal resolution of that system. An SSD material would offer only a single measurement with an integration window typically being the lifetime of that material. The quartz in brick would provide the accumulated dose to that material all the way back to the time it was baked. Ambient quartz or feldspar from smears or air samples would give an OSL dose estimate back to the time it was zeroed based on exposure to sunlight or any other sufficiently intense optical photon source.

Depending on the material, non-radiogenic, native signals may exist and would need to be subtracted from the resultant measurements. Sample preparation can likewise induce interfering signals, which require identification and mitigation. To further complicate the approach, a number of factors can work to decrease the signal to noise ratios of these dosimetric materials. For example, internal



Figure 5: Nuclear weapons storage (creative commons license image).

radioactivity contributes to background signals not associated with the anthropogenic exposure of interest; time-dependent signal decay decreases the signal with increasing time from the event of interest; and variable sensitivity of sample materials complicates with determination of the minimum detectable limit of a given sampled material. All of these variables have to be properly understood and accounted for in order to provide precise dosimetric estimates from opportunistically scavenged sample material.

Perhaps the largest drawback to using SSD as a forensics technique is the overall throughput for obtaining results. Typical dose estimates from ubiquitous materials such as brick, wallboard (sheetrock or plasterboard) and confectionary range require days to weeks to produce. In this sense, the time commitment to obtaining quality results is comparable to modern radiochemistry and so does not allow rapid analysis unless quality is commensurately poor.

Other groups have proposed portable OSL systems [22] but without TL, they are of limited value in determining sensitivity, which severely limits their overall utility. Similarly, portable EPR systems have likewise been proposed but have also been shown to have very low sensitivity [23]. Currently, laboratory based SSD systems are required to obtain meaningful results which are now able to start approaching background levels.

3.2 Spoofing

As with any detector, surrogate sources could be envisaged, designed and constructed. Similarly, this detector could be annealed or made impotent. If an evasive actor were to heat all the walls around a source up to 500° C, then the TL/OSL/EPR signals would all be zeroed back as though it had just been created in the kiln. Alternatively, an actor could construct their walls out of conducting metal and keep the environment meticulously clean (dust-free) so as not to leave ambient dosimeters about. Even then, the lighting would require some form of insulation to enable workers to be productive without requiring miner's lamps to conduct operations.

Even an annealed wall will retain tell-tale SSD signatures if they are not uniformly heated to 500° C. Assuming this can be done, it would have to occur in such a way that heating the room itself did not leave evidence such as requiring all new wood, plastic and rubber peripherals as these would all combust or melt under such a kiln treatment. Still, removing a full brick may be reasonably rejected due to building integrity if reparative measures are not properly implemented.

Given the requirements inherent to spoof an SSD forensics approach, it would be prohibitively difficult to fully erase all evidence of noncompliant actions on the part of any nuclear state. While spoofing activities would add additional uncertainty to the forensic analyses presented above, it

should be noted that more advanced analysis methods exist that could be applied to such problems. In the worst case, a bounding analysis on gross dose estimates would likely be sufficient to determine if the environmental dosimetric records agree with operator declarations. Residual evidence of spoofing itself may be actionable without source reconstruction whatsoever but details would be specific to particular scenarios.

4. Discussion

The utility of measuring the electronic properties of non-conducting materials enables these to become effective dosimeters. Further, the techniques described herein are, in general, applicable to samples collected from bulk materials (i.e. bricks and tiles) down to single grain samples (aerosolized particulate matter). As one might expect, the information available varies with sample size (lower doses generally requiring more sample). As current particulate analysis protocols consider only chemical, isotopic and morphological properties, adding in electronic property characterization with TL, OSL and EPR can provide additional information previously overlooked.

For example, with bulk sample analysis, differential attenuation in the material provides a means by which the energy of the radiation field can then be obtained (albeit at a low effective resolution). Even using multiple samples from a gridded array offers the potential to reconstruct the location of the nuclear material (via inverse square and any shielding considerations) such that the technique can serve as a gamma camera [2].

On the other hand, combining SSD in particulate matter with plume reconstruction techniques may allow for forensic analysis at large standoff distances. To the extent that the atmospheric transport of nonconductive particulate matter mirrors the transport of other materials released by nuclear facilities, one can envision performing dosimetric analysis on particles released by such facilities. In this way, it may be possible to gather information about the activities being performed within. Realization of this capability would allow verification of nuclear operations from a distance, without the need to even step foot inside the facility itself.

As a general statement, most organic materials are better suited for EPR measurement. Alternatively, inorganic insulators tend to work better with TL and OSL characterization. TL and OSL do require the samples to be at least partially transparent to transport the recombination photons with OSL requiring the stimulation light to also penetrate the grains be analyzed. Most materials have some signal which can be measured with all methods but to widely varying sensitivity, linearity and native signal contributions from each such that initial testing or literature recommendations will often guide the user to a preferable measurement protocol. Even with this, particular variations

in a given material type could in principle warrant customization of any portion of the sample preparation approach and/or measurement sequence.

By combining the applications of EPR with TL and OSL, all insulator materials can be utilized. One drawback with common environmental materials is the potential for a large geological dose background. This can be partially mitigated using various techniques presented by others [24] although at the cost of decreased quality in the resulting dose estimate. However, given the variety in materials that this combination of techniques may utilize, there is reasonable likelihood that in any given sample, some useful material could be scavenged.

5. Conclusions

The potential applicability for SSD in nuclear forensics is effectively in its infancy. The realization that the electronic populations of ubiquitous, insulating materials can be used to reconstruct the gross position and energy source material, retrospectively, has implications which are lightly reviewed in this work. If the success of prior studies could be extended to particulate matter from environmental smears or air samples, then it would be possible to perform dosimetric assay for treaty verification without direct access to the facility. This would mark a significant improvement in the current suite of tools currently employed for treaty verification and nonproliferation.

6. Acknowledgements

7. References

- [1] O'Mara RB, Hayes RB. Dose deposition profiles in untreated brick material. *Health Phys.* **114**(4), 414-420, 2018.
- [2] Hayes RB, Sholom SV; Retrospective imaging and characterization of nuclear material. *Health Phys.* **113**(2), 91-101, 2017.
- [3] Hayes RB, O'Mara RP; Retrospective dosimetry at the natural background level with commercial surface mount resistors. *Radiat. Meas.* **121**, 42-48, 2019.
- [4] Hayes RB. Retrospective uranium enrichment potential using solid state dosimetry techniques on ubiquitous building materials *J Nuc Mat Mgmt.* (in press).
- [5] Alexander GA, Swartz HM, Amundson SA, Blakely WF, Buddemeier B, Gallez B, Dainiak N, Goans RE, Hayes RB, Lowry PC, Noska MA, Okunieff P, Salner AL, Schauer DA, Trompier F, Turteltaub KW, Voisin P, Wiley AL, Wilkins R. BiodosEPR-2006 Meeting: Acute dosimetry consensus committee recommendations on biodosimetry applications in events involving uses of radiation by terrorists and radiation accidents. *Radiat. Meas.* **42**, 972–996, 2007.
- [6] Wieser A, Goksu HY, Regulla DF, Vogenauer A; Limits of retrospective accident dosimetry by EPR and TL with natural materials. *Radiat. Meas.* **23**(2/3) 509-514, 1994.
- [7] Ding Y, Jiao L, Zhang W, Zhou L, Zhang X, Zhang L. Research on EPR measurement methods of sucrose used in radiation accident dose reconstruction. *Radiat. Prot. Dosim.* **138**(4), 393-396, 2010.
- [8] Belahmar A, Mikou M, Mamadou Saidou A, Bougrib M; EPR analysis of dosimetry properties of various organic materials for radiotherapy applications. *Physica Medica* **32**, 246, 2016.
- [9] Belahmar A, Mikou M, Mamadou Saidou A, Baydaoui RE; EPR spectroscopy investigations of some organic materials irradiated by electrons, in prospect of their use in radiotherapy. *Physica Medica* **44**, 14-15, 2017.
- [10] Hayes RB; Reconstruction of a radiological release using aerosol sampling *Health Phys.* **112**(4), 326-337. 2017.
- [11] Hayes RB, O'Mara RP; Enabling Nuclear Forensics Applications from the Mineral Particulate in Contamination Surveys. *Advances in Nonproliferation Technology and Policy Conference*, Orlando FL, Nov 12-15, 200-204, 2018.
- [12] Duller GAT, Bøtter-Jensen L, Murray AS and Truscott AJ. Single Grain Laser Luminescence (SGLL) Measurements Using A Novel Automated Reader. *Nucl. Instr. Meth. In Phys. Res. B.* **155**, 506-514. 199.
- [13] Hayes RB, Haskell EH, Barrus JK, Kenner GH and Romanyukha AA; Accurate EPR radiosensitivity calibration using small sample masses. *Nucl. Instr. Meth. A.* **441**, 535-550. 2000.
- [14] Hayes RB, Haskell EH, Wieser A, Romanyukha AA, Hardy BL and Barrus JK; Assessment of an alanine EPR dosimetry technique with enhanced precision and accuracy. *Nucl. Instr. Meth. A.* **440**, 453-461. 2000.
- [15] Haskell EH, Hayes RB and Kenner GH; Native signal subtraction, g-factor normalization and constant rotation goniometry are valid methods in EPR dosimetry. *Health Phys.* **77**, 472-475. 1999.
- [16] Rieger PH. *Electron Spin Resonance – Analysis and Interpretation*. Royal Society of Chemistry, Retrieved from <https://app.knovel.com/hotlink/toc/id:kPESRAI001/electron-spin-resonance/electron-spin-resonance>

- [17] Rank WJ and Schwarcz HP. Dose Response of ESR Signals in Tooth Enamel. *Rad. Meas.* **23**, 481-484. 1994.
- [18] Yukihara EG, McKeever SWS; *Optically Stimulated Luminescence: Fundamentals and Applications 1st Edition*. John Wiley & Sons, West Sussex, UK, 2011.
- [19] Ikeya M; *New Applications Of Electron Spin Resonance: Dating, Dosimetry And Microscopy*. World Scientific, Singapore, 1993.
- [20] Hayes RB, O'Mara RP and Hooper DA. Initial TL/OSL/EPR Considerations for Commercial Diatomaceous Earth in Retrospective Dosimetry and Dating. *Rad. Prot. Dosim.* 1-10, doi:10.1093/rpd/ncz013, 2019
- [21] Karakirova Y, Yordanov ND Sucrose as a dosimetric material for photon and heavy particle radiation: A review. *Radiat. Phys. Chem.* **110**, 42-50, 2015
- [22] Thomsen KJ, Bøtter-Jensen L, Jain M, Denby PM and Murray AS. Recent Instrumental Developments for Trapped Electron Dosimetry. *Rad. Meas.* **43**, 414-421, 2008.
- [23] Williams BB et al. A deployable *in vivo* EPR tooth dosimeter for triage after a radiation event involving large populations. *Rad. Meas.* **46**(9), 772-777, 2011.
- [24] Ikeya M. *New Applications of Electron Spin Resonance Dating, Dosimetry and Microscopy*. World Scientific Publishers, Singapore, 1993.

Production of particle reference and quality control materials

Timothy R. Pope¹, Bruce W. Arey¹, Mindy M. Zimmer¹, Michael DeVore II², Michael G. Bronikowski², Wendy Kuhne², Aaron T. Baldwin², Cristina Padilla-Cintron¹, Norman C. Anheier¹, Marvin G. Warner¹, Matthew S. Wellons², and Christopher A. Barrett¹

¹Pacific Northwest National Laboratory, Richland, WA 99354, USA

²Savannah River National Laboratory, Aiken, SC 29808, USA

E-mail: Chris.Barrett@pnnl.gov

Abstract:

Maintaining the superior performance of new analytical instrumentation and pushing the boundaries of ever-smaller particle analysis by methods such as secondary ion mass spectrometry (SIMS) has become limited by the availability of certified particle standards for calibration, quality control, and validation. To meet this growing demand for a reliable and universal approach to the generation of uranium particle reference material, the Pacific Northwest National Laboratory (PNNL) and Savannah River National Laboratory (SRNL) are collaborating on a joint venture that establishes a number of chemical pathways to the fabrication, purification, and stabilization of uranium particle material to within a fixed particle size range, and well-characterized isotopes. PNNL particle standards are designed and tailored to meet the criteria essential to the calibration and benchmarking of instruments used in both the non-destructive and destructive assay of particulate material, typically collected from environmental swipe sampling. Previous testing and optimization of this colloidal approach to particulate material has centred on tight size distributions, singular composition and density, uniform morphology, and tailored isotopic abundances. Extensive validation of this material has since been performed, both at the National Institute of Standards and Technology (NIST) and the International Atomic Energy Agency (IAEA), demonstrating its suitability for quality control needs of large geometry (LG)-SIMS analysis. Building on this momentum, the production of low-enriched uranium particle reference material, with specially tailored isotopes, has moved from development to full operation. Herein, various aspects of the production cycle will be discussed, including detailed accounts of the technical methodologies being employed, as well as insights into the sample characterization and acceptance testing requirements.

Keywords: particle; standards; uranium; safeguards, synthesis

1. Introduction

Trace analysis of particulate material collected on environmental swipe samples has long been a cornerstone in the IAEA's process of verifying member state compliance as

part of the Non-Proliferation Treaty (NPT).¹ The swipe samples collected by inspectors are taken from the surrounding environment within a nuclear site and then subjected to two common forms of measurement, namely bulk and discrete analysis. In the first case, the entire cotton swipe is digested and analysed with respect to U, Pu, and other elements present at ultra-low concentration levels. The latter approach takes aim at the precise isotopic analysis of individual U- or Pu-containing particles, with sizes ranging from 1-10 µm typically observed. Discrete analysis of individual particles generally entails the use of both scanning electron microscopy (SEM) and SIMS, both of which are regarded as non-destructive for swipe samples, as the swipe is not destroyed as part of the sample preparation process. By contrast, a swipe is completely consumed by bulk analysis using a combination of high-temperature ashing and acid digestion. While many different isotopic standards, commonly referred to as certified reference material (CRM), are available for destructive forms of assay, notably thermal ionization mass spectrometry (TIMS) and inductively coupled plasma mass spectrometry (ICP-MS), particle standards for SIMS analysis are far less common and more difficult to produce.²

In recent years, the IAEA has had limited success in maintaining a steady supply of particle-based standards from the European Commission - Joint Research Centre, Directorate G – Nuclear Safety and Security, Unit G.2 for Standards for Nuclear Safety, Security and Safeguards (JRC-Geel, formerly IRMM), mainly due to the fact that certified particle standards are atypical products for both IRMM, and the New Brunswick Laboratory (NBL) in the US. Because the IAEA requires a longer-term strategy for particle standards supply, production methods have been pursued at the Forschungszentrum Jülich (FZJ),³ as well as by several other member states partnered to the Network of Analytical Laboratories (NWAL).⁴⁻⁶ While many different technical approaches are being developed, all are constrained by the same stringent requirements necessary for useful particle standards for SIMS analysis. As an example, techniques for the generation of uranium-bearing particles should provide uniform particle morphology and density, narrow particle size distributions (~1 µm), singular chemical composition (oxides preferable), tailorabile isotopic profiles, and a demonstrated shelf-life of 1 year or more. Additional factors to be considered range from the relative structural

integrity of the particles subjected to mechanical forces such as sonication or micro-manipulation, to estimates on the rate of U leaching in different storage media.⁷ Of paramount importance is the ability of any proposed technique to continually produce unbiased, isotopic uniformity in each batch of material. By their very nature, particles can easily migrate through an environment and deposit across surfaces, which is the premise behind environmental swipe sampling. Consequently, steps to mitigate particle cross-talk must be fully integrated with the design and production of particle reference materials.

To this end, a new method and system of producing UO₂ particle reference material of a prescribed isotopic profile is described herein. This work is the culmination of collaborative efforts between PNNL and SRNL, under the support of the National Nuclear Security Association and the United States Support Program to the IAEA. The systematic approach laid out in this paper begins with the detailed formulation and blending of CRM to generate uranium material of a desired isotopic composition, followed by chemically transforming it into a suitable precursor form for colloidal synthesis. A tailored synthesis protocol for the generation of UO₂ particulate is then introduced, including parameters to optimize the technique for specific IAEA requirements. Finally, a thorough characterization of particle properties, including crystallinity, size, shape, and density, is reported. Further, an isotopic evaluation is performed by LG-SIMS, the mass spectrometry technique for which the particles were originally designed. It is hoped that the combined efforts of PNNL and SRNL reported herein demonstrate the viability of this new production process and its potential for delivering uranium oxide particles sourced from current CRM and tailored to the stringent criteria necessary for particle reference materials.

2. Uranium Feedstock Formulation

2.1 Isotopic Mixing

New QA/QC particulate reference materials may require the formulation of a unique uranium isotopic composition with a specific composition of four U isotopes (i.e. ²³⁴U, ²³⁵U, ²³⁶U, and ²³⁸U). For example, new reference materials may be designed to validate specific environmental sampling scenarios representative of typical nuclear operations, such as uranium enrichment and spent fuel reprocessing, among others. Manufacture of the desired uranium isotopic composition requires the mixing of uranium starting material with precisely known isotopic content, such as CRMs. CRMs are available commercially from multiple international organizations, both in Europe and the US, and have well-documented and published values for

each uranium isotope. Development of the specific mixing recipe for a new QA/QC material involves the reconciliation of available CRM feedstock, their respective expense of procurement, and a desire to minimize the number of CRMs used in a formulation.

Choosing a combination of isotopic standards to incorporate under the specified constraints can be categorized as a convex optimization problem,⁸ which can be solved in a variety of ways. In the optimization of isotopic standard mixing, we seek the best way to combine a set of n reference materials to meet a set of conditions set by the QA/QC material end user (i.e. the IAEA). These constraints are concerned with the content of ²³⁴U, ²³⁵U, and ²³⁶U and the balance of ²³⁸U. Note that minimizing the computational power necessary to solve the problem is an important consideration, as well as reducing the number of standards used within the mix. Additionally, a range of ratios must be considered for all possible CRM combinations. To date, several methods have been used to generate permutations of all possible mixes of uranium certified reference materials. Described below is the method utilized by initial work in this topic.

The primary method used was a brute force R-based program that created arrays to represent each standard. These were combined into matrices that were multiplied by a content matrix. The content matrix contained four columns that matched an isotopic composition value to each standard in the array. This multiplication generated a list of possible solutions, and such multiplications were performed over the entire problem space. Certain constraints were applied to the problem to generate a set of solutions. Figure 1 provides a visual representation of the possible combinations of all US commercially available uranium CRMs limited to combinations of ≤ 3 . For convenience, this plot is labelled in terms of the ²³⁵U enrichment, the ²³⁶U concentration, and the ²³⁵U/²³⁴U ratio. The data points represent $>10^6$ individual CRM combinations varied in both CRM selection and their ratios. In practice, we have found the 3D representation to be valuable in rapidly determining potentially impossible U isotopic composition targets. The solutions were manually screened, and <10 viable recipe candidates were selected based on factors mentioned previously. This method did not take advantage of programmatic methods to reduce problem complexity and improve computational efficiency. The selected CRM mixing recipes were always checked against two separate independent review calculations to verify the numerically accuracy. We found that a subsequent iterative discussion between the various stakeholders was invaluable to validate and down select the proposed recipes (plus their respective isotopic composition) to a single mixture.

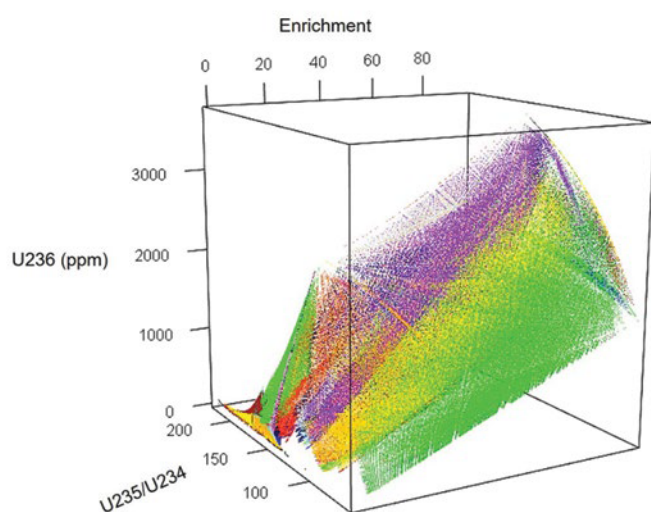


Figure 1: 3D plot of approximately 10^6 data points representing potential combinations of ≤ 3 CRM mixture isotopic compositions in terms of ^{235}U enrichment, ^{236}U concentration in ppm, and the $^{235}\text{U}/^{234}\text{U}$ ratio. Colours are for 3D illustrative purposes only.

Note that due to the proprietary nature of new QA/QC specimens for nuclear safeguards proficiency testing, feedstock and micrometre particle syntheses are discussed in a manner agnostic to specific isotopic compositions.

2.2 Chemical Manipulation

CRMs were obtained from the US Department of Energy, NBL Program Office. The mixing ratio and identity of specific CRM combinations was determined by the calculation method detailed earlier in this publication. The overall synthesis scheme is shown in Figure 2, which demonstrates the generic formulation of metal and/or oxide CRM feedstocks into a uranyl acetate product with tailored uranium isotopic content. Mixing of CRMs and subsequent synthesis of uranyl acetate were typically done on the gram scale to ease physical laboratory manipulations and minimize routine sources of measurement errors, such as with balances, pipettes, etc.

A typical uranyl acetate feedstock preparation starts with the dissolution of the CRMs, which are either uranium oxide or metal. Uranium metal rods are broken into pieces and placed in 8 mol/L HNO_3 to remove the oxide layer. After 30 minutes, the pieces are removed, rinsed with water and acetone, dried, and weighed.⁹ The pieces are then put into a fresh solution of 8 mol/L HNO_3 to dissolve and form uranyl nitrate ($\text{UO}_2(\text{NO}_3)_2 \cdot x\text{H}_2\text{O}$). The U_3O_8 CRMs are heated at 400 °C for 2 hours to drive off water in accordance with recommended practices. After cooling, the U_3O_8 was weighed and dissolved in 8 mol/L HNO_3 with heating at 60 °C to generate a second uranyl nitrate solution.

Portions of the two uranyl nitrate solutions were mixed based on a previously calculated recipe to generate

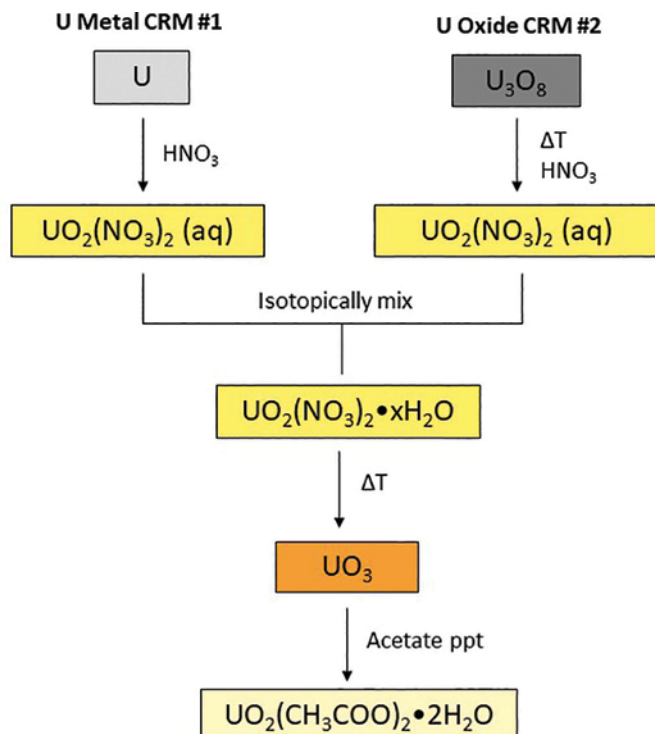


Figure 2: Prototypical chemical reaction and manipulation pathway for the dissolution of various CRMs, their mixing, and subsequent synthesis of uranyl acetate with predefined isotopic composition.

a uranyl nitrate solution with the desired isotopic composition. The product was subsampled and analysed by TIMS to verify the isotopic composition. The uranyl nitrate solution was heated at between 80 °C and 100 °C until dryness to form a nitrate solid salt of the isotopically mixed crystalline hydrate. Next, uranyl nitrate was heated at first at 120 °C to remove water and then at 400 °C for 2.5 hours to generate the gamma phase of UO_3 .¹⁰ The UO_3 was allowed to cool before being weighed and then a solution of dilute acetic acid was added and heated to 50 °C. The material dissolves and upon evaporation precipitates as uranyl acetate, which was filtered and washed first with cold dilute acetic acid and then with water.¹¹

The isotopically mixed uranyl acetate product was characterized by Raman spectroscopy, fluorescence spectroscopy, and powder X-ray diffraction (PXRD) to verify the material phase and identify any other potentially undesirable chemical phases (e.g. schoepite, uranyl carbonate, etc.). Once the acetate material phase was confirmed, the product was subsampled again and analysed with TIMS to confirm isotopic content. Uranyl acetate slowly degrades in ambient conditions by reaction with atmospheric moisture, and therefore, all product was stored in nitrogen-purged containers within double mylar containers that included desiccating capsules. All laboratory workspaces were rigorously cleaned between before and after synthesis of the CRM mixed uranyl acetate product to avoid contamination between batches.

3. Production & Processing of UO₂ Particle Standards

3.1 Reaction Procedure

A facile hydrothermal route for the phase-controlled synthesis of highly crystalline UO₂ particles was developed and tailored to meet the desired characteristics needed for the milligram synthesis of particle standards. The technique can be described as a scalable batch reaction, which offers greater batch-to-batch repeatability and can be easily tuned to vary the material yield within the order of a few milligrams, all the way up to 200 mg. Hydrothermal synthesis is a well-established method of synthesizing colloid particles using a combination of high temperature and pressure.¹² In this way, reaction mechanisms not achievable at standard temperature and pressure can be performed within the confinement of a Teflon-lined pressure vessel, as shown in Figure 3. The specific method described herein uses organic amines as both reducing agents and structure-directing ligands, further simplifying the synthetic procedure. In its acetate form, uranyl ions are found to readily complex with ethylenediamine, which then undergo a thermolysis reaction that triggers the nucleation and growth of UO₂ crystals. In using a sealed reaction vessel during heating and synthesis, considerations for safe operation and handling of radioactive material are streamlined, adding multiple layers of containment and providing a simple means of mitigating any batch-to-batch “cross-talk” between particles of different isotopic profiles.

For this study, UO₂ particles were synthesized by the following protocol: 0.05 mmol (20 mg) of uranyl acetate (UO₂(CH₃COO)₂·2H₂O) and deionized water (15 mL, 0.833 mol) are mixed to form a homogeneous solution under vigorous stirring. Once the uranyl acetate is completely dissolved, 8.5 mL of glacial acetic acid (CH₃CO₂H, 0.15 mol) is added and stirred for 20 minutes. To this yellow solution, 5 mL of ethylenediamine (C₂H₄(NH₂)₂, 75 mmol) is added dropwise under continuous stirring for 20 minutes. After

the potential of hydrogen (pH) equilibrates, a surfactant can be added to the solution as an additional growth-directing agent. The resulting solution is then sealed in a 25 mL Teflon-lined, stainless-steel autoclave and heated at 160 °C for 48 hours. After the heating step, the reaction vessel is cooled to ambient temperature, and the final product is washed with deionized water and isopropanol several times using bath sonication and centrifugation (4250 rpm) before being stored over isopropanol. A minimum of 5-7 washing steps are required to remove trace amounts of organic residue on the surface of the particles. Prior to washing with isopropanol, a 15-minute dilute acetic acid (0.1 mol/L) wash under bath sonication is performed to ensure the removal of any trace amounts of schoepite (discussed below).

3.2 Hydrothermal Synthesis

Under ordinary circumstances, UO₂ production for nuclear fuel comprises a series of chemical modifications followed by high-temperature annealing (>700 °C) of UO₃ under hydrogen atmosphere. While efficient, the process takes considerable effort and no small degree of risk when dealing with explosive gases. A hydrothermal synthesis, on the other hand, is a simple water-based approach that exploits the reduced nucleation threshold of crystalline UO₂ material when under pressurized conditions. By carefully controlling the starting conditions of the hydrothermal synthesis, it is possible to optimize the reaction further. One such optimization involves the reduction of schoepite, a hydroxide species that typically forms under basic conditions, in a range of pH 8-12. Schoepite has a characteristic two-dimensional morphology—distinct from the spherical shape of UO₂ particles—, which is correlated to its layered crystal structure that is comprised of alternating layers of uranium oxide and a hydrated hydroxide species of uranyl oxide. This phase of uranium has an undesired geometry, poor stability in ambient conditions, and a lower density than pure oxides of uranium (e.g. UO₂). While schoepite can be removed by bath sonicating dispersions in dilute acetic

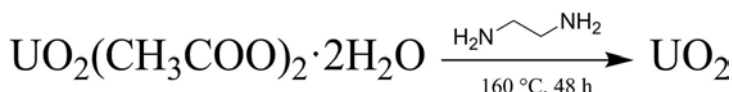
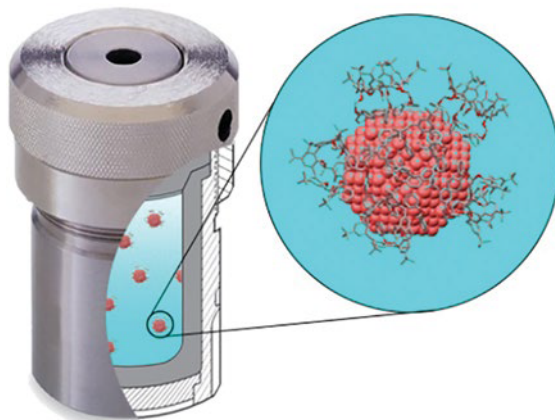


Figure 3: Hydrothermal reaction vessel comprised of a Teflon insert encased in a stainless-steel housing and the prototypical chemical reaction scheme for the synthesis of UO₂ particles.

acid, the UO_2 fraction is inadvertently damaged by surface etching. In a less-invasive attempt of mitigating schoepite, the pH of the starting solution can be systematically reduced by controlling the amount of acetic acid added to the initial solution. In this way, the production of UO_2 spheres increases to near 100% as the pH decreases to 7.5. Conversely, observations of any schoepite crystals rapidly diminished, with only trace amounts detected on rare occasion. It should also be noted that the schoepite reduces in size as the pH is decreased, visually indicating the unfavourable schoepite growth conditions in the lower, close to neutral, pH range. As the pH is adjusted to neutral and further to the acidic range (pH 6), neither schoepite nor UO_2 is produced, which is expected, as these phases are both oxide-based and are not stable under acidic conditions.

3.3 Crystal Growth & Post-Processing

During synthesis development, batches of UO_2 particles are screened using transmission electron microscopy (TEM) to evaluate the size, shape, and crystallinity of individual particles. Figure 4(A) and 4(B) show representative images of particles synthesized from a large-batch (200 mg), hydrothermal reaction. Most particles were found to have a spherical morphology, with size distributions shifting to larger diameters (1-3 μm) for reactions on the scale of hundreds of milligrams to lower diameters (0.5-1.5 μm) for smaller batches of material (10-20 mg). This level of size control was demonstrated by simply changing the starting precursor concentration while keeping reactor, solution, and reagent volumes constant. In this way, monomer

supply to evolving nuclei is far less abundant, which slows the crystal growth and reduces the average diameter of the resulting UO_2 particles. The corresponding selected area electron diffraction (SAED) pattern shown in Figure 4(B) seems to indicate that the particles are close to single crystal. However, as the diffraction spots are slightly skewed along a specific d-spacing, it is more likely that the particles are pseudo-polycrystalline. Such characteristic would suggest an orientated-attachment mechanism for crystal growth, which would follow that smaller nanosized crystals are first nucleated during the reaction and then agglomerate to further crystallize into larger micrometre-sized particles. In such an instance, nanocrystalline grains assume a preferred orientation that energetically favours attachment. Under tighter ligand and precursor control, it would be possible to synthesize single-crystal UO_2 particles with ideal density characteristics.

Given that the primary end use for these materials is directed towards particle standards for LG-SIMS, removal of all organic residue from as-synthesized UO_2 particles was another primary focus of this work. Many colloidal approaches use high concentrations of surfactant ligands and structure-directing agents, all of which lead to heavy deposits of carbon contamination and poor mass spectrometry measurements. While TEM has proved to be the workhorse instrument for particle screening, helium ion microscopy (HeIM) can be employed for its surface-sensitive imaging capability and capacity to identify any residual organic material. TEM is a transmission-based technique, and so lighter element materials are transparent when imaged by this

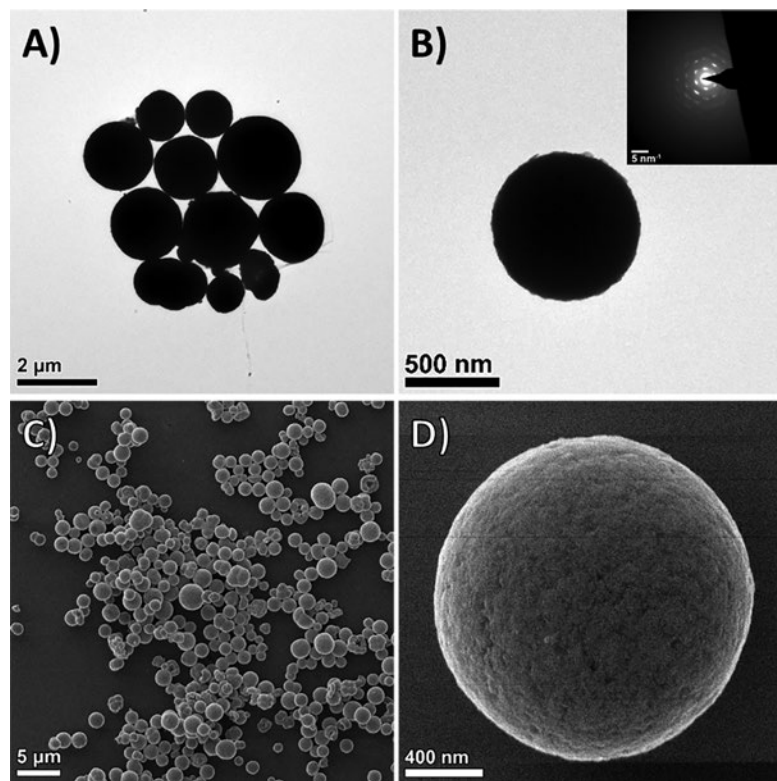


Figure 4: (A, B) TEM and (C, D) HeIM images of UO_2 particles post-processed with solvent washing.

approach. Electron-based microscopy, both the scanning and transmission variants, typically suffers from what is referred to as a high-interaction volume. This phenomenon arises because of the elevated accelerating voltage and current used to image a sample with electrons, which can reach up to 300 keV in the case of transmission systems. Consequently, the volume of sample releasing secondary electrons increases, and the resulting image can appear transparent and less representative of the surface topography. In the case of high-Z contrast material, the effect is suppressed; however, the low-Z organic residue, often encountered with colloidal synthesis, can be difficult if not impossible to fully observe. To gauge the level of "cleanliness" of our UO_2 particles, HeiLM is used to thoroughly evaluate samples washed with repeated amounts of isopropyl alcohol and deionized water. The end result, as portrayed in Figure 4(C) and 4(D), is well-defined particles in which the surface topography is clearly resolved, with no trace of organic residue detected.

4. Material Characterization & Validation

4.1 Particle Crystallinity and Size Distribution

Pure oxide of uranium, including UO_2 , UO_3 , and U_3O_8 , have extend storage times in both solution and powder form such that particulate materials meet the requirement to maintain a shelf-life of 1 year or more. PXRD analysis is employed to evaluate the chemical composition and crystal structure from the bulk product of each hydrothermal synthesis. In all cases, peak analysis of collected data matched to that of a fluorite crystal structure, indicative of UO_2 material. Over the course of many different variations

of hydrothermal synthesis, only UO_2 and schoepite were observed from the reaction of uranyl acetate and ethylenediamine. As can be seen in Figure 5(A), precisely tuning the pH of the starting mixture to 7.5 gives a single composition of UO_2 material. The sharp peak intensities of the observed diffraction pattern are typical of highly crystalline material and provide a useful means of estimating the average density of the particles.

Aliquots taken from milligram-sized (~20 mg) reactions of as-synthesized UO_2 particles are used to prepare a silicon planchet with concentrated areas of particles for imaging and size analysis. Multiple images are then collected at a consistent field of view (100 μm) so that a large population of particles can be measured for a representative estimate of the size distribution. Figure 5(B) summarizes the results from this analysis; however, it should be noted that a circularity filter was used during image processing to isolate particle agglomerations and instead focus on the measurement of discrete, individual particles. This commonly employed practice of size analysis mitigates the addition of spurious measurements to the overall distribution that might otherwise skew the results in one direction or the other. As can be seen from the plotted size distribution, the largest fraction of UO_2 particles (27%) are found to have a diameter in the range of 1-1.25 μm . In addition, approximately 55% of particles analysed fell within a size range of 0.5-1.25 μm , a metric mandated by the IAEA in their request for QC particle materials. Roughly 77% of the sample falls within the size range of 0.5-1.5 μm , which gives a corresponding mean diameter of 1.26 μm . However, the median diameter, measured at 1.19 μm , is likely a better reflection of the sample, given the slight downshift in the mean diameter due to

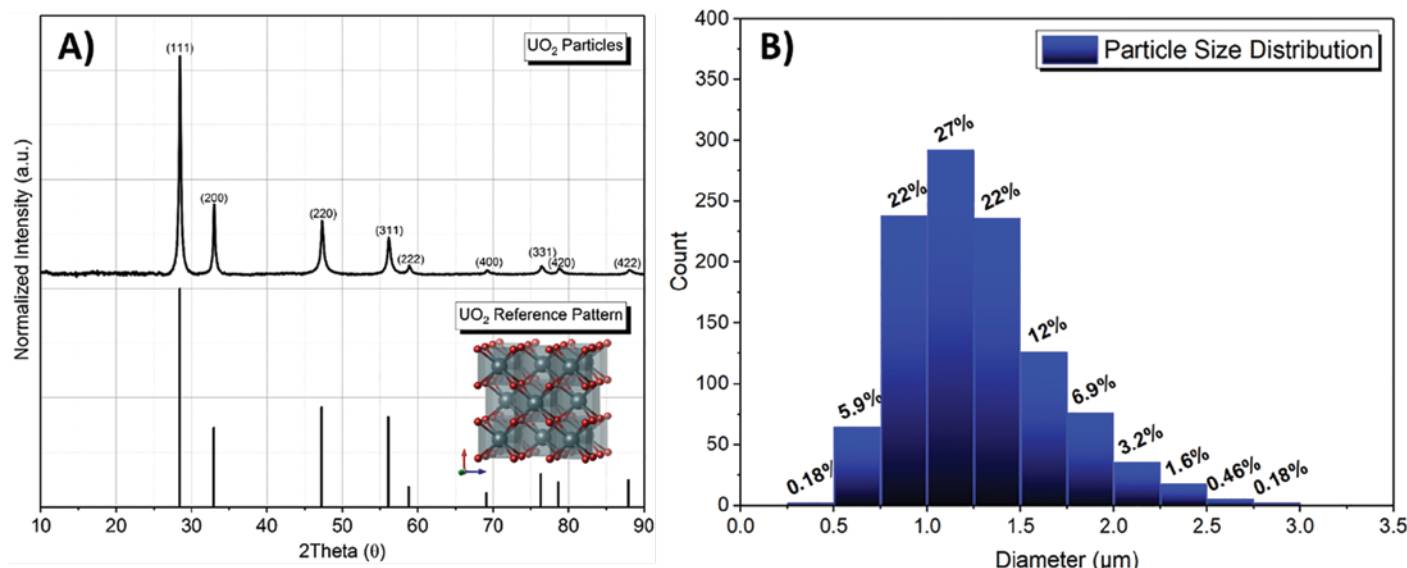


Figure 5: (A) PXRD data of the as-synthesized material, including the matching reference pattern of UO_2 (cubic/fluorite crystal structure, black droplines). (B) Size distribution of all U-containing particles.

a few larger particles in the 2.5-3 μm range, which constitute less than 1% of the total sample.

4.2 Microstructure and Density

While estimation of particle density can be qualitatively calculated from bulk PXRD, microstructural analysis of individual UO_2 particles is a more accurate means of quantifying density and other influencing factors such as porosity and void fraction. For this analysis, a method of particle encapsulation and focused-ion beam (FIB) milling is used to generate cross-sections for internal micro/nanostructural imaging. This process is accomplished by first depositing a thick layer of carbon via electron beam-induced deposition (EBID) that encompasses the entire particle. The surrounding layer of carbon encapsulates the particle, providing support during the FIB milling process and manipulation of the thin particle cross-section. Cross-sections are extracted from individual UO_2 particles and then mounted such that the inner surface of the particle can be imaged from a side-on perspective using SEM and STEM (Figure 6).

A representative set of images taken of a 1 μm particle is given in Figure 6. The results highlight near-uniform density expected for crystalline particles, with small amounts of porosity on the order of 4-6%. Cross-sectional images in Figure 6, captured with several different imaging modes, resolved only a minute number of nanosized pores, likely arising from the postulated crystal growth mechanism of orientated-attachment. Estimates for the measured particle void fraction and density were calculated using the theoretical density of single-crystal UO_2 (10.97 g/cm³) and the volume of a particle calculated from the diameter observed during SEM imaging. Calculations for the particle shown in Figure 6 were based on a measured diameter of 1.1 μm and a relative porosity of 4.5%, giving an estimated density of 9.23 g of U/cm³ (1.8×10^{10} U atoms). A lack of severe

porosity of the synthesized particles is an important result, as the theoretical density of the particles presented in this work is higher than that of other forms of uranium oxide, providing more uranium atoms per particle volume for mass spectroscopy applications.

4.3 Isotopic Profile

To facilitate end-user analysis and develop a capability for the selection of specific particles of interest, a technique akin to fission track TIMS can be used to prepare UO_2 particles on a specialized substrate.¹³ As a means of expediting the search routine normally employed to find uranium-bearing particles, a 500×500 μm grid (with letter and number reference markings) is etched into the surface of a vitreous-carbon planchet for particle placement at marked locations. Under SEM imaging, shown in Figure 7A, a nanomanipulator is then used to pick and place particles of interest to the patterned grid. The manipulator, housing a FIB-sharpened tungsten needle, can extract particles from the surface using localized carbon adhesion focused at a point of contact and then places them onto designated regions of a secondary substrate. Once deposited, the particle is held to the substrate via weak forces and can be analysed immediately or, alternatively, held in place via a small amount of deposited platinum (Figure 7B) for long-term storage or shipment. The patterned, vitreous-carbon planchet provides a referenceable grid location (Figure 7C) of each particle placed on the substrate, negating the need to run Automatic Particle Measurement software and expediting the overall measurement time. Additionally, this method provides the opportunity to directly image particles prior to and directly after SIMS analysis. Figure 7D shows a representative sample prepared on a laser-etched carbon planchet.

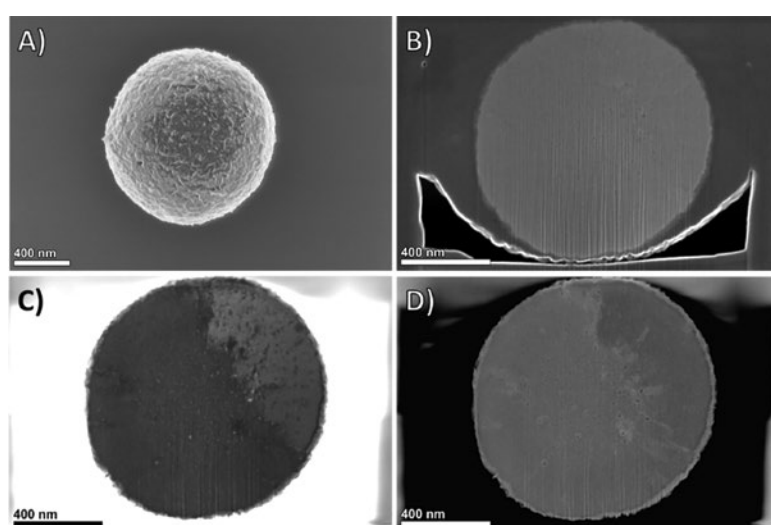


Figure 6: SEM images of (A) a 1 μm particle and (B) a FIB-milled cross-section of a carbon encapsulated UO_2 particle. (C) Annular bright-field and (D) annular dark-field images of the same cross-section.

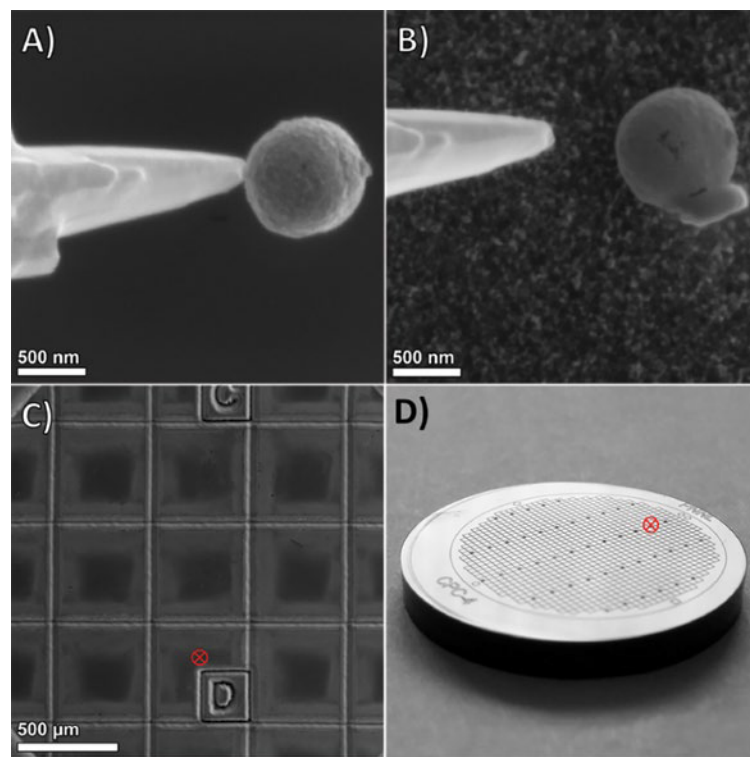


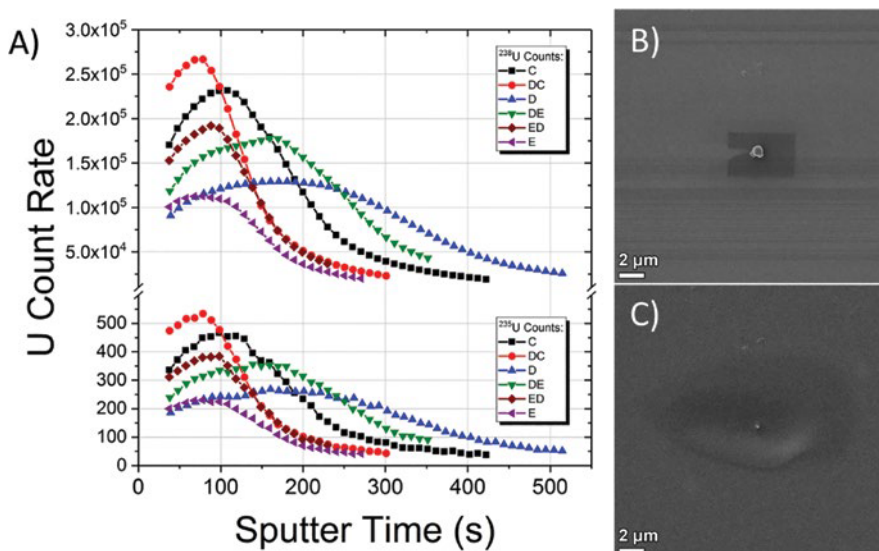
Figure 7: SEM images showing (A) the removal of a particle from a silicon wafer, followed by (B) placement on a carbon planchet at a (C) known marked location. (D) Optical image of the laser-patterned planchet.

To test the suitability of the particles to serve as standards in the environmental sampling program for IAEA Safeguards, prepared planchets are evaluated using a Cameca IMS-1280 Large Geometry SIMS. This is the same model that is used for particle measurements by most of the members of the IAEA NWAL. Analyses are performed with a focused primary ion beam of O^{2+} at an impact energy of 8 keV. The species detected are positive uranium ions at an energy of 10 keV. The primary beam current and raster-scanned area are adjusted depending on the specific analysis. Uranium-bearing particles are located by real-time scanning ion imaging over a $500 \times 500 \mu\text{m}$ area with the mass spectrometer tuned to ^{238}U . Bright particle images are easily visible against a uniform uranium background after a period of pre-sputtering. A selected target particle is centred on the ion optical axis by translation of the sample stage, and the raster size and beam current are adjusted to $10 \times 10 \mu\text{m}$ and 200 pA, respectively, for isotopic analysis. In this manner, isotopic measurements of all six particles picked and placed to a patterned substrate can be made, and the results processed to account for signal trending, detector dead time, isotopic mass bias, and hydride correction for ^{236}U . The results of these isotopic composition measurements are given in Table 1, along with the weighted averages and standard deviations. The measured isotopic variation among the particles is consistent with the internal measurement uncertainty for each particle, and is in

good agreement with the bulk analysis of the same material analysed by multi-collector ICP-MS.

Several individual particles were subjected to depth profile measurements by SIMS. Particles were selected in a similar manner to that described above for isotopic measurements, but they were analysed by monitoring the ^{238}U signal continuously as a function of time until the signal fell to about 1% of its maximum value, and then the integrated number of ^{238}U ion counts was determined. Two different types of profiles shapes (count rate vs. sputter time) are observed, as illustrated in Figure 8. One type, depicted by particles D and DE, shows a short increase in signal, followed by a gradual signal fall-off, with the entire profile lasting 300–400 seconds. Based on the previous analysis, this behaviour is characteristic of particles at or near a micrometre in size. The other type of profile, illustrated by particles DC and ED, shows an almost immediate onset of a roughly exponential signal decay, and the signal persists for a little less than 200 seconds. This behaviour is characteristic of much smaller particles or of a thin film of uranium. The first profile type contains much higher ^{238}U counts than the second profile, which is consistent with the smaller particle size measured by SEM. Following SIMS analysis, particles were re-imaged by SEM, where it was found that the depth profile analysis completely consumes the UO_2 , leaving behind only a small amount of platinum (from EBID) and a sputtered region of about 12 μm in diameter.

Sample	^{234}U	^{235}U	^{236}U	^{238}U	$\phi (\mu\text{m})$
E	0.00088	0.20330	0.00287	99.79295	0.675
ED	0.00062	0.20370	0.00300	99.79268	0.525
DE	0.00067	0.20339	0.00297	99.79296	0.725
D	0.00070	0.20405	0.00295	99.79229	0.850
DC	0.00068	0.20178	0.00309	99.79444	0.600
C	0.00073	0.20099	0.00275	99.79553	0.500
SIMS Average	0.00071	0.20287	0.00294	99.79348	0.645
1σ	0.00006	0.00121	0.00015	0.00122	
ICP-MS Average	0.000695	0.1984	0.00278	99.798	
1σ	0.000043	0.0004	0.00009	0.0003	

Table 1: Uranium isotopic composition of PNNL particles in atom percent.**Figure 8:** (A) The measured trends for count rate over sputtering time, and (B,C) SEM images of UO_2 particle (designated “DE”) before and after depth profile analysis by LG-SIMS.

5. Summary

To tackle the shortfall in particle reference material for nuclear safeguards activities, PNNL and SRNL have devised a multi-step production process to meet the stringent requirements mandated for uranium particle standards. SRNL have developed a unique means of generating tailored isotopic profiles derived from a computational matrix of different blending options available from current CRM inventories. It was also shown that a method of re-crystallising blended material into different chemical forms, more conducive to particle synthesis, could be used following the CRM mixing process. In this way, precursor material of

a desired isotopic profile could be prepared at SRNL and shipped in a form compatible with a given synthetic procedure. In the case of this study, uranyl acetate precursor was outlined for PNNL’s synthesis of uranium oxide (UO_2) particle standards, realised by a hydrothermal reaction technique. The colloidal chemistry approach developed at PNNL is tailored for the primary production of UO_2 , and the minimization of other uranium products—namely, schoroeite—and other morphologies. Optimization was accomplished through acid-base equilibrium chemistry (pH control), and control of reactant stoichiometry.

The bulk composition of the produced particles was examined by PXRD and SAED, with both analytical

techniques confirming the particles to be highly crystalline and of a single fluorite structural phase. Additionally, particle size analysis from TEM, SEM, and HeLM images showed that the isolated spherical particles had a size range of 0.5-1.25 µm for a typical synthesis of 20 mg batches. If particles could also be produced with much tighter control of particle size and in different size ranges, they could be suitable for other applications such as inter-laboratory comparisons and improvement of mass spectrometry measurement techniques. Using FIB and STEM analysis, observations were made of the internal structure of individual UO₂ particles, with measurements for the void fraction confirming low-levels of porosity (4-6%), and densities reaching near theoretical levels for UO₂ (9.23 g of U/cm³). UO₂ particle standards generated by hydrothermal synthesis afford much greater uranium densities compared with other oxide compositions, making them ideal candidates for particle standards analysis. Throughout each phase of the production process, a rigorous handling and cleaning protocol was continually maintained to ensure that batches of particles remained free of cross-contaminants.

Finally, a technique to select particles of specific size and morphology and place them on a laser-patterned grid of a vitreous carbon planchet for SIMS analysis was reported. This approach was then used in conjunction with a SIMS analysis to assess particle proficiency. Findings from the evaluation study of UO₂ particles suggests that in their present form they could be quite useful as QC samples that the IAEA could introduce to the NWAL as blind samples on cloth. The micrometre size range is typical of the samples that the IAEA collects, and for this purpose, they do not need to be monodispersed. To be useful on a continuing basis, they would need to be produced in batches of various enrichment levels with avoidance of cross-contamination and validation of the isotopic composition after production. It is advantageous that they are not bound to a medium during production and instead can be supplied in a vial for the IAEA to use as it sees fit.

6. Acknowledgements

The authors wish to thank the team at the IAEA Safeguards Analytical Laboratory for their expert advice and critical feedback throughout this work. The Pacific Northwest National Laboratory is operated for the U.S. Department of Energy by Battelle Memorial Institute under Contract No. DE-AC05-76RL01830. This work was sponsored by the U.S. Department of Energy, National Nuclear

Security Administration, Office of Nonproliferation and Arms Control, International Nuclear Safeguards program.

7. References

- [1] Boulyga, S.; Konegger-Kappel, S.; Richter, S.; Sangely, L. *J. Anal. At. Spectrom.* 2015, 30, 1469-1489.
- [2] Mathew, K. J.; Stanley, F. E.; Thomas, M. R.; Spencer, K. J.; Colletti L. P.; Tandon, L. *Anal. Methods*, 2016, 8, 7289-7305
- [3] Middendorp, R.; Dürr, M.; Knott, A.; Pointurier, F.; Ferreira Sanchez, D.; Samson, V.; Grolimund D. *Anal. Chem.* 2017 89 (8), 4721-4728.
- [4] Stoffel, J. J.; Briant, J. K.; Simons, D. S. *J. Am. Soc. Mass Spectrom.* 1994, 5, 852-858.
- [5] Erdmann, N.; Betti, M.; Stetzer, O.; Tamborini, G.; Kratz, J. et al. *J. Spectrochim. Acta, Part B* 2000, 55, 1565-1575.
- [6] Kips, R.; Pidduck, A. J.; Houlton, M. R.; Leenaeers, A.; Mace, J. D.; Marie, O.; et al. *Spectrochim. Acta, Part B* 2009, 64, 199– 207.
- [7] Middendorp, R.; Dürr, M.; Niemeyer, I.; Bosbach D. *ESARDA BULLETIN*, No. 54, June 2017
- [8] Boyd, S.; Boyd, S. P.; Vandenberghe, L.; Press, C. U., *Convex Optimization*. Cambridge University Press: 2004.
- [9] Lacher, J. R.; Salzman, J. D.; Park, J. D., *Dissolving Uranium in Nitric Acid. Industrial & Engineering Chemistry*. 1961, 53, 282-284.
- [10] Herrmann, W. A., *Synthetic Methods of Organometallic and Inorganic Chemistry* Georg Thieme Verlag: 1996.
- [11] Bagnall, K. W., *The actinide elements*. Elsevier Publishing Company: 1973.
- [12] Nkou Bouala, G. I.; Clavier, N.; Podor, R.; Cambedouzou, J.; Mesbah, A.; Brau, H. P.; Léchelle J.; Dacheux N. *CrystEngComm*, 2014, 16, 6944-6954.
- [13] Admon, U.; Donohue, D.; Aigner, H.; Tamborini, G.; Bildstein, O.; Betti M. *Microsc. Microanal.* 2005, 11, 354–362.

Nuclear archaeology: reconstructing reactor histories from reprocessing waste

Antonio Figueroa, Malte Götsche

Aachen Institute for Advanced Study in Computational Engineering Science
 Physikalisches Institut III B
 RWTH Aachen, Germany
 Schinkelstr. 2a, 52062 Aachen, Germany
 Email: figueroa@aices.rwth-aachen.de, goettsche@aices.rwth-aachen.de

Abstract:

Nuclear archaeology is a field dedicated to the reconstruction and quantification of the past production of fissile materials. As part of related research efforts, we examined in this study the possibilities and limitations of exploiting measurements of high-level waste to deduce parameters related to the operational history of reactors such as burnup. For the first stage of this project, we used high-fidelity reactor simulations to estimate spent-fuel compositions, and developed a surrogate model which can be used as a computationally less-expensive method to map combinations of input parameters to fuel compositions. This model gives us a better understanding of the challenges involved in solving the inverse problem of deducing the reactor history from waste measurements. A promising method to solve this inverse problem may be Bayesian inference, where prior existing information (e.g. a declaration by a state) can be taken into account, and waste measurements would be used to update this knowledge. This way, measurements may confirm the existing information, make it more accurate or identify inconsistencies which may indicate intentional or unintentional non-conformity of the declaration. For a proof of concept of the methodology, we examined in this study three simple scenarios in order to determine a few reactor parameters, given a hypothetical declaration by a state and a simulated measurement of the waste isotopic composition.

Keywords: nuclear archaeology; nuclear forensics; disarmament; verification; Bayesian inference

1. Introduction

While there is extensive experience from IAEA Safeguards in verifying both the correctness and completeness of nuclear material declarations issued by non-weapon states members of the Non-Proliferation Treaty, there is a lack of methods to verify nuclear material ‘baseline’ declarations, i.e. the first verified declaration a state makes upon entering an agreement. A solid understanding of fissile-material holdings is needed to achieve a meaningful degree of predictability and irreversibility of future arms-control initiatives. Speculations about unaccounted fissile-material stockpiles, possibly equivalent to hundreds of nuclear

weapons, could make progress in this area very difficult [1].

Most large-scale fissile-material production programmes were driven by a sense of urgency and typically shrouded in secrecy. It is generally believed that accounting for these military operations was poor. The fissile material production uncertainty is very large, and even states themselves have had difficulty reconciling production records with physical inventories. In the United States, for example, estimated plutonium acquisitions exceeded the actual inventory by 2.4 tons, but it is not clear whether this material ever existed [2]. For HEU, the US inventory difference is about 3 tons [3].

In addition to direct data on produced fissile materials, such records would contain operational information on the nuclear facilities. For the nuclear reactors, besides reactor and fuel designs, this would include data such as reactor power, fuel burnup and cooling time (which refers to the time elapsed since a specific production campaign occurred). In this paper we refer to these as operational parameters.

In order to obtain more accurate plutonium estimates, a first approach in reconstructing the production history is to perform reactor simulations using newer, more accurate codes than those used decades ago. One such recent code is SERPENT 2 [4], which takes the operational parameters as input and calculates the isotopic composition of the discharged fuel — including plutonium, but also fission products and actinides — as output.

Additionally, measurements in shut-down facilities can be taken to obtain complementary data. For example, experimental research has been done on taking moderator or structural material samples in reactors to independently deduce/reconstruct the amount of plutonium produced in these shut-down facilities [5,6]. This approach is known as nuclear archaeology.

However, what is still lacking is a systematic and integrated approach that ties together all available information — not only from measurements, but also from available records about the past fissile material production. Such an approach could be used to identify inconsistencies (for example between records and actual measurements),

reconstruct missing data from records using measurements, and quantify and reduce the uncertainties on the amount of produced fissile materials.

Here, we propose to use Bayesian inference for this purpose. To demonstrate the approach, we present a first and preliminary proof-of-concept study using a very simple scenario. This method is based on measuring high-level waste from reprocessing using mass spectrometry, as has been proposed for nuclear archaeology [7]. The high-level reprocessing waste contains nearly all fission products and actinides after dissolving the spent fuel. Accordingly, it contains a rich isotopic signature of past fuel cycle activities. The radioactive waste could therefore be used to estimate the operational parameters of the fuel cycle, such as fuel burnup or cooling times.

This approach would directly benefit states that apply it by providing a better understanding of their nuclear programme's history. Additionally, it could be used as a verification tool. For instance, in the case of a state declaring that a reactor was used for civilian purposes with high burnup, this method could prove whether a low burnup campaign for possible military purposes was run. Similarly, a reactor may have run for more time than declared, which could be detected by examining the cooling times.

While it is not clear whether the proposed approach could be applied to complex programmes, this study shows that it may be fit for use in small programmes of a complexity similar to the North Korean case, in which essentially only the Yongbyon reactor is the origin of the country's plutonium inventories.

Section 2 provides an overview of the theoretical background and methodology used in this study. In Section 3, the implementation of the approach is described. In Section 4, test scenarios and the practical application of the Bayesian framework are presented. Section 5 contains the results of the evaluated test scenarios and a discussion thereon, followed by conclusions and research outlook in Section 6.

2. Theoretical background

As described previously, the isotopic composition of high-level waste (\vec{y}_{obs}), which would be measured during verification activities, can be obtained from the output of reactor simulations. Our task is to solve an inverse problem. Indeed, we seek with our approach the input to those simulations — which we call forward simulations — the operational parameters (\vec{x}). Our forward simulations can then be thought of as a model that can compute $\vec{y} = f(\vec{x})$. Reactor simulations such as SERPENT 2 couple a Monte Carlo neutron transport routine with a fuel depletion routine [8]. Therefore, $f(\vec{x})$ cannot be described in a simple function that could perhaps be inverted analytically. In the following,

we explain how it can, however, be inverted using a numerical method.

2.1 Bayesian inference

Bayesian inference solves an inverse problem, by treating it statistically. It is particularly suited for inverting intractable and complex models, as is the case for reactor operations. Using Bayes' theorem, the posterior probability can be calculated, which is the probability distribution $p(\vec{x} | \vec{y}_{obs})$ that specific reactor parameter combinations \vec{x} (operational parameters) might have produced the measured isotopic composition of the high-level waste \vec{y}_{obs} (output). It is expressed as follows:

$$p(\vec{x} | \vec{y}_{obs}) \propto p(\vec{y}_{obs} | \vec{x}) \cdot p(\vec{x}) \quad (1)$$

where $p(\vec{y}_{obs} | \vec{x})$ is the likelihood, which is the distribution of probabilities that the measured isotopic composition would have been obtained by a specific combination of operational parameters. It is obtained by running a large number of forward-simulations to explore the space of possible operational parameters (parameter space) where the (simulated) output of each forward-simulation \vec{y} is compared to the (real) measured isotopic composition \vec{y}_{obs} . It is assumed that \vec{y} is normally distributed, hence

$$p(\vec{y}_{obs} | \vec{x}) = \prod_{i=1}^N \exp\left(\frac{-|y_{obs}^i - f_i(\vec{x})|^2}{\sqrt{2}\sigma_i}\right)$$

where the index i represents an isotope under consideration and σ_i is the corresponding uncertainty, which must be provided. It must include all sources of uncertainties: measurement uncertainties, model uncertainties, etc. The equation above requires that the isotopes chosen be independent of each other.

The particular benefit of the Bayesian approach is that prior knowledge can be included, which is given by manually formulating $p(\vec{x})$. Such prior knowledge could be, for instance, information from records of the production history and to which an uncertainty value can be assigned. According to Bayes' theorem, this prior information is then combined with the measurement to produce the posterior. Another advantage of this approach is that, due to its probabilistic nature, it allows for the propagation of uncertainties, so that uncertainties on the reactor parameter estimates can be obtained.

2.2 Markov Chain Monte Carlo and Gaussian process regression

The posterior is numerically constructed by exploring the reactor parameter space by evaluating different reactor parameter combinations \vec{x} . To choose these combinations we use Markov Chain Monte Carlo (MCMC). A Markov chain is a sequence of events constructed in such a way

that any given event \vec{x} is only affected by the immediately previous event [9]. MCMC is a class of algorithms that combine traditional Monte Carlo methods together with Markov chains in order to sample the posterior from a given probability distribution. In the present work, we have chosen to use the MCMC NUTS algorithm, which is a state-of-the-art algorithm in the context of Bayesian inference [10].

Using a high-fidelity reactor simulation, the exploration of the posterior can be computationally prohibitive, since depending on the number of parameters to be reconstructed, several thousands of simulations would be usually required for MCMC. Therefore, instead of directly running reactor simulations, we developed a surrogate model that accurately represents the high-fidelity model but can be evaluated much faster. Specifically, the model is based on Gaussian Process Regression (GPR) to approximate the results of the simulations.

GPR belongs to a class of interpolation methods with important applications on response surface approximation for complicated functions, in particular those of the ‘black-box’ type for which no analytical mathematical expression exists, as in our case. Unlike other regression methods using a particular function type or polynomial decomposition, the GPR performs a regression using a distribution over functions, which share assumptions on basic properties such as smoothness and differentiability [11]. These assumptions are codified through the use of covariance information of a set of parameter vectors (\vec{x}) with which the interpolation model is created. Such information is used under the hypothesis that parameter vectors that are close to each other correspond to isotopic vectors (\vec{y}), which

would be also be close to each other. Using this, GPR allows prediction of the value of the underlying function $\vec{y} = f(\vec{x})$ at non-simulated values \vec{x} [12].

Our surrogate model was created by running SERPENT 2 simulations using many different \vec{x} . The choices of \vec{x} have been obtained using quasi-Monte Carlo sampling. We used the Halton sequence, through which input parameter vectors can be generated from a deterministic sequence with low discrepancy [13].

3. Model and surrogate model implementation

As a proof-of-concept study, we implemented an infinite lattice model of the Savannah River Site K Reactor’s inner core using data from [14-18]. This reactor was designed for the production of weapons-grade plutonium, as well as tritium. It consists of a high-power heavy-water reactor operated almost continuously for a period of approximately five decades, along with four other similar reactors at the Savannah River Site with a maximum power of 2400 MWth. During the operation of this reactor, several fuel element designs were tested. The design implemented in this work is that of the Mark 15 uniform lattice fuel element, which uses an enrichment of 1.1 %. This design was chosen due to data availability and because it was the most efficient design ever tested [14].

Figure 1 shows the SRS-K Reactor implementation in SERPENT 2. To our knowledge, information on the spent-fuel concentrations, which could have served to validate the model, is not publicly available. Therefore, in order to assess the general quality of our model, we successfully verified that the evolution of the infinite multiplication factor

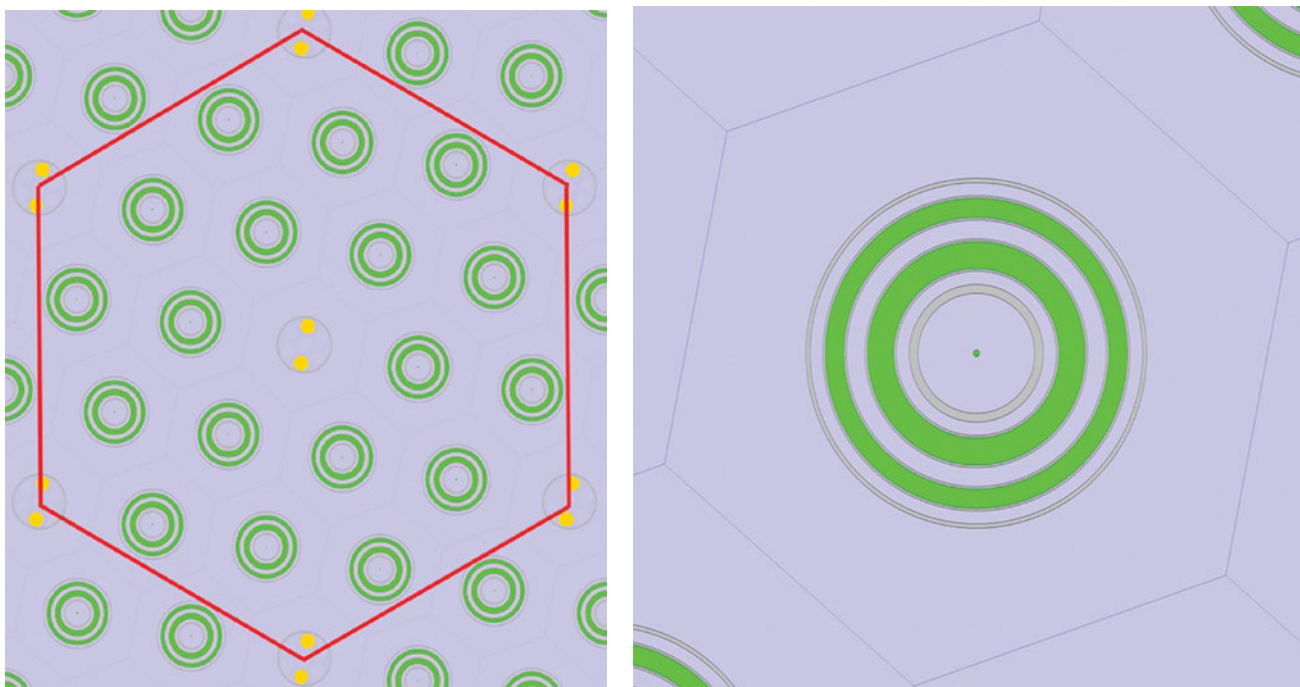


Figure 1: Mark 15, 2D – infinite lattice implementation (left). Detail of Mark 15 fuel element (right).

as a function of irradiation time was plausible, and that the energy-integrated reactor neutron flux ϕ and the fuel load calculated based on the SERPENT output agreed with the literature [14].

The operational parameters \vec{x} considered for the surrogate model are fuel burnup (B), cooling time (Ct), and power. In addition, enrichment values of around 1.1 % are selected within a range consistent with criticality considerations. To create the surrogate model, 1000 SERPENT 2 simulations were run. The ranges of the three operational parameters are shown in Table 1. These parameters obey operational limitations due to the reactor design and historical constraints. For each output isotope, we built a GPR model using the Scikit-learn library in Python [19].

The quality of the GPR surrogate models was studied through a chi-square two sample test, a standard test in statistical analysis [20]. For this, 6000 additional SERPENT 2 simulations were run and directly compared to the predictions of the GPR models at their respective test points. These results are shown in Table 2 with the corresponding symbols χ^2 – GPR/SERPENT and p – GPR/SERPENT, denoting the test statistic and the corresponding p-value. To gain deeper insight, a Gaussian fit of the errors between the model predictions and the simulations has been made. If the GPR surrogate model can reproduce SERPENT 2 simulations with good quality, then the errors should be normally distributed with zero mean. We analysed this fit again with the above test, calculating the χ^2 – Errors and its corresponding p – Errors values, also shown in Table 2. This table shows the calculated statistics for a selected group of isotopes. It can be observed that for these isotopes the GPR models describe the data well.

Power (MW)	Burnup (MWd/kg)	Cooling time (a)
600 – 2400	0 – 3	0 – 50

Table 1: Range of input parameters used in the SRS K reactor model. These values also correspond to the limiting values for the reliable reconstruction of these parameters.

	^{137}Cs	^{90}Sr	^{154}Eu	^{142}Nd	^{95}Mo
χ^2 – GPR/SERPENT	0.81	0.67	0.30	0.28	0.16
p – GPR/SERPENT	0.93	0.95	0.98	0.99	0.99
Mean – Errors	6×10^{-6}	6×10^{-5}	4×10^{-6}	2×10^{-6}	6×10^{-5}
Std - Errors	3×10^{-4}	6×10^{-4}	3×10^{-5}	2×10^{-5}	6×10^{-4}
χ^2 – Errors	5.92	7.31	11.14	7.47	10.01
p – Errors	0.43	0.50	0.52	0.88	0.44

Table 2: Above: Results of a chi-square test, comparing the isotopic concentrations calculated by SERPENT and GPR. Below: Gaussian fit parameters and goodness-of-fit analysis for the GPR model errors relative to SERPENT 2 simulations. Mean and standard deviation are given in absolute units. Results of a chi-square test of normality are shown. Typically, one would assume both chi-square tests to be successful if $p > 0.05$, which is clearly the case. Therefore, the GPR models describe the data with a high likelihood.

Our study aims at examining whether fuel burnup and cooling time can be reconstructed using ^{137}Cs , ^{154}Eu , ^{95}Mo , ^{142}Nd and ^{90}Sr , assuming that the power and the enrichment are known. These isotopes were chosen because of their good sensitivity to the two parameters. This was assessed by a variance-based sensitivity analysis calculating Sobol indices [21]. Scatterplots illustrating reactor-simulation results for these isotopes are presented in Figure 2.

In an actual application, one would study isotope ratios. If the proof-of-concept can be demonstrated with individual isotopic concentrations, we hypothesise that it should also be feasible with isotopic ratios, as the underlying mathematical principles would remain the same.

4. Proof of principle – scenarios

Our basic study focuses on a very limited plutonium production scenario, obtained from a single reactor and for which discharging and reprocessing of fuel occur only once or twice. The high-level waste is then stored in a single tank. Similar conditions are believed to represent the situation in North Korea, when IAEA inspectors conducted on-site-inspections on reprocessing waste samples after the state joined the Non-Proliferation Treaty [22].

To solve the inverse problem, first, \vec{y}_{obs} must be calculated by choosing specific values of \vec{x} that are used as input to SERPENT 2. The software package PyMC3 [23] is then used in order to calculate the posterior(s). The algorithm has no knowledge of the originally chosen values \vec{x} , but reconstructs them based on \vec{y}_{obs} . For each scenario we have used 2×10^5 posterior evaluations. We consider a successful reconstruction only if the maximum probability of the posterior distribution is close to the chosen values.

To summarise, Figure 3 illustrates in a schematic way the steps of the methodology that we propose in order to verify and reconstruct reactor operational histories under the above-described scenarios.

Three scenarios were studied.

1. A single fuel batch has been reprocessed, the burnup and cooling time are unknown but the power is known (1018 MW). Uniform probability distributions of the two parameters are used as a prior, i.e. giving equal probability for the parameters within a range defined by minimum and maximum values $U[min, max]$ (see Table 3). A vector y_{obs} for the isotopes ^{137}Cs , ^{154}Eu and ^{95}Mo is calculated. We assume that all isotopic concentrations carry an uncertainty (σ_i) of 10 %. This is an upper bound estimate that we use, as a detailed uncertainty assessment has not been conducted for this feasibility study.

2. The same scenario as above, but assuming more precise prior information, for example from authenticated records that had been produced during the past reactor operations, resulting in narrower ranges of the uniform prior (see Table 3).
3. Two batches (\bar{y}_i^{obs}) with different burnup values are assumed. The waste produced is stored in the same tank, resulting in the isotopic composition \bar{y}_{mix} . In this case, uniform priors are also considered for both burnups, covering the span of possible model values. The mass ratio α of the two batches must then also be reconstructed:

$$\bar{y}_{mix} = \alpha \bar{y}_1^{obs} + (1 - \alpha) \bar{y}_2^{obs}$$

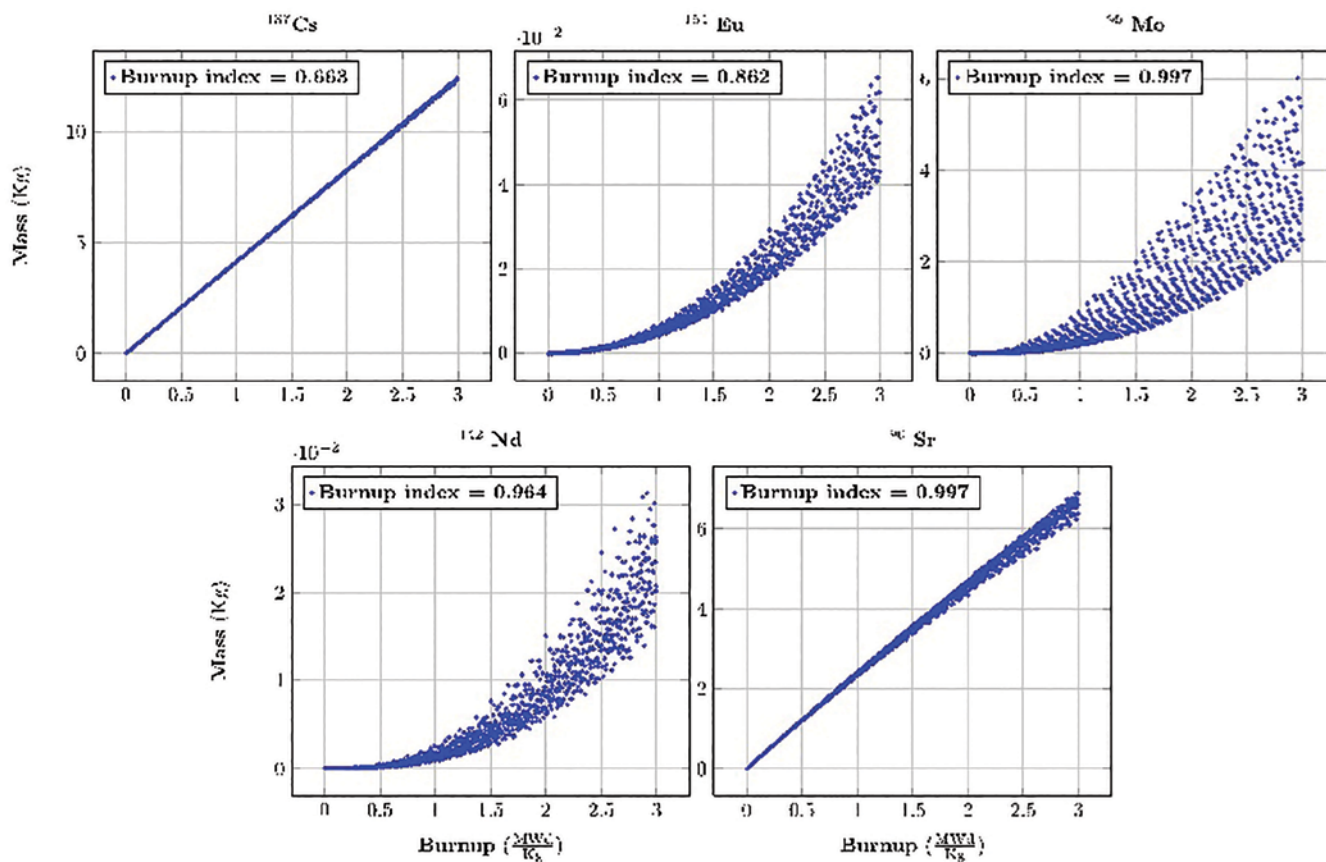


Figure 2: Scatterplots of selected isotopes as a function of burnup. The values serve as the basis for calculating the Sobol sensitivity indices, which are indicated in each plot. These plots are one-dimensional projections of simulation results using SERPENT 2 for different parameter combinations of power, burnup and enrichment.

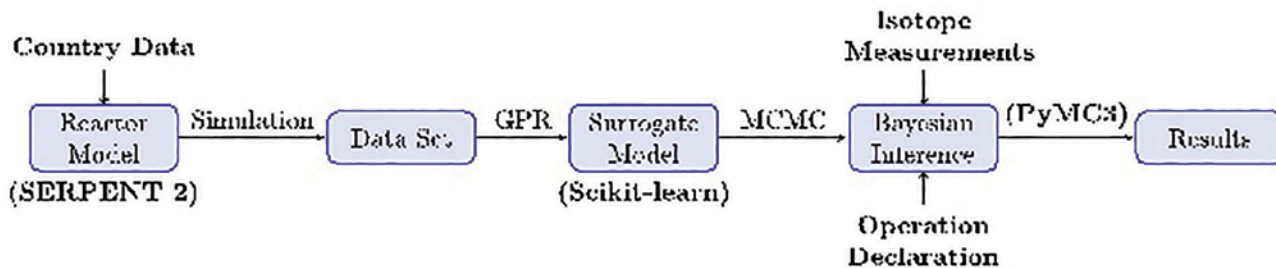


Figure 3: Workflow of the reactor history reconstruction methodology. The respective software packages are indicated in parentheses.

this scenario, the power is also 1018 MW and the cooling time is 29.6 years. A vector \bar{y}_{mix} for the isotopes ^{137}Cs , ^{154}Eu , ^{95}Mo , ^{142}Nd and ^{90}Sr is calculated, and the assumed uncertainty (σ_i) of the isotopic concentrations is now 5 %.

Scenario	Burnup (MWd/Kg)	Cooling time (Years)	Mixing ratio (α)
Scenario 1	$U[0,3]$	$U[0,50]$	-
Scenario 2	$U[1.65,1.95]$	$U[27,31]$	-
Scenario 3	$U[0,3]$	-	$U[0,1]$

Table 3: Comparison of priors for all scenarios.

5. Results and discussion

5.1 Scenario 1: Reconstruction of burnup and cooling time with uninformative prior

The results for scenario 1 are shown in Table 4 and Figure 4, in which we observe a well-defined, non-pathologically shaped joint posterior distribution. By examining Table 4, it can be assessed that the burnup and cooling time parameters are reconstructed with reported relative uncertainties of 5 % and 6 %, respectively. Quantifying the uncertainties of the estimates is an important advantage of using the Bayesian approach. The estimated mean values lie within 0.1 % of the true values used to compute the measurements vector.

Parameter	True value	Posterior mean	Posterior std	Relative uncertainty
Burnup (MWd/Kg)	1.793	1.790	0.091	5 %
Cooling time (years)	29.6	29.7	1.8	6 %

Table 4: Scenario 1, summary of the parameters and results. True values refer to the values used to obtain the vector of simulated measurements y_{obs} .

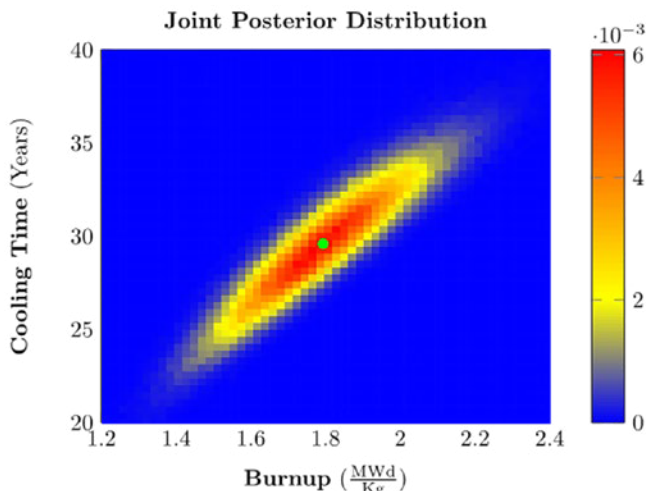


Figure 4: Normalised posterior distribution for scenario 1. The correct solution is indicated in green.

5.2 Scenario 2: Reconstruction of burnup and cooling time with a constrained prior

The results for scenario 2 are shown in Table 5 and Figure 5, which demonstrate that having/using a constrained prior allows the spread of the posterior distribution to be reduced. On the one hand, this occurs by limiting the space of possible solution values and cutting values inconsistent with the uniform prior. On the other hand, and more importantly, the probability distributions fall more steeply around the maximum likelihood. The uncertainties of the reconstructed burnup and cooling time are 2.8 % and 3.3 %, respectively. This demonstrates the important role of the priors in the Bayesian approach, with constrained prior(s) reducing the uncertainties of the operational parameters.

Parameter	True value	Posterior mean	Posterior std	Relative uncertainty
Burnup (MWd/Kg)	1.793	1.799	0.050	2.8 %
Cooling time (years)	29.6	29.8	1.0	3.3 %

Table 5: Scenario 2, summary of the parameters and results. True values refer to the values used to obtain the vector of simulated measurements y_{obs} .

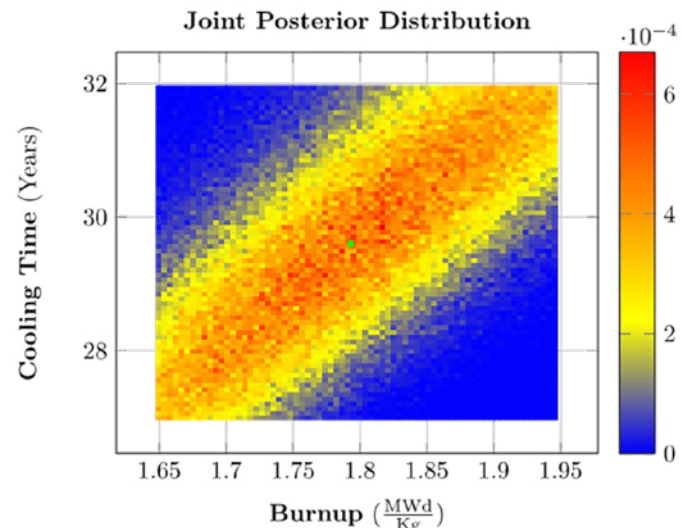


Figure 5: Normalised posterior distribution for scenario 2. The correct solution is indicated in green.

5.3 Scenario 3: Reconstruction of burnup values of a mix of two batches

The results for scenario 3 are shown in Table 6 and Figure 6. As observed in the two previous scenarios, the reconstructed posterior is again well defined, with both burnup values successfully estimated. Although the burnup values are close, they can be clearly distinguished in their reconstructed posteriors. The estimated uncertainty for Burnup 1 is 18.6 %. For Burnup 2 and the Mixing Ratio, the estimated uncertainties are 7.6 % and 26.9 %, respectively. In this scenario the uncertainties are much larger

than in the previous one. We believe that this could be caused by the limited choice of isotopes under analysis. The absolute standard deviations of the posterior for both burnups are similar. This results in larger relative uncertainties for *Burnup 1* than *Burnup 2*. Also, please note that an uncertainty of 5 % was assumed for the isotopic concentration, as opposed to the 10 % used for the previous scenarios. With larger uncertainties here, the uncertainties of the posterior increase further. More research is to be done in order to study the sources of the posterior uncertainties and the selection of a more appropriate set of isotopes for the reconstruction of mixtures.

Parameter	True value	Posterior mean	Posterior std	Relative uncertainty
Burnup 1 (MWd/Kg)	0.800	0.874	0.163	18.6 %
Burnup 2 (MWd/Kg)	1.825	1.776	0.135	7.6 %
Mixing ratio	0.410	0.367	0.099	26.9 %

Table 6: Scenario 2, summary of the parameters and results. True values refer to the values used to obtain the vector of simulated measurements y_{obs} .

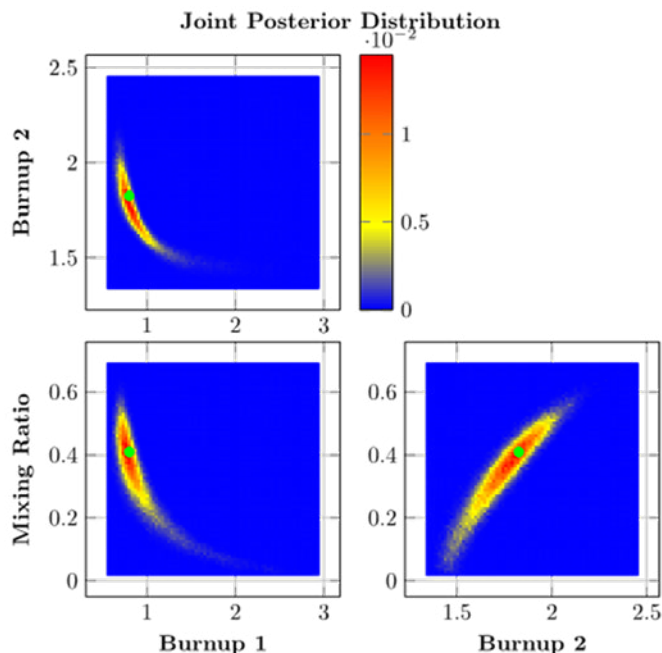


Figure 6: Normalised posterior distributions for scenario 3. The correct solution is indicated in green.

6. Conclusions and outlook

With this study, we have successfully demonstrated the possibility of reconstructing reactor operational parameters using isotopic samples of reprocessing waste in combination with reactor simulations and operational knowledge within a Bayesian inference framework. This enables the simultaneous reconstruction of both burnup and cooling time, along with the estimation of the uncertainty of these

parameters given the available knowledge. These uncertainties were obtained assuming that the uncertainties of the measured isotopic concentrations were around 5-10 %. A detailed uncertainty quantification study is required for a better understanding of the uncertainties of isotopic concentrations. We assume 5-10 % uncertainty is an upper bound.

Further research will include full-core reactor simulations and a systematic study of isotopic ratios to be used in the analysis. Due to various processes in waste tanks such as precipitation, which can affect different elements in different ways, one has to use ratios of isotopes that behave similarly in the waste tank for this analysis, so that such processes do not influence the analysis. Nevertheless, this study is valid as the mathematical principles (i.e. the feasibility of a surrogate model, and Bayesian inference) and expected uncertainties are the same or similar in both cases.

While we have focused on simple scenarios, any real nuclear programme would likely be more complex than the three cases considered in this study. In particular, the number of reprocessed batches, each with varying operational parameters, would be larger. However, in the case of small nuclear programmes, this larger list of parameters might still be reconstructed, as a much larger set of isotopes than those presented here could be considered in the analysis. However, this would clearly not work for large programmes such as those conducted in Russia or the United States. In these cases, strategies must be found to reduce the number of parameters to be reconstructed. This is called model reduction, a classic topic in computational science [24], which in our case could possibly involve grouping a number of batches together and describing them by average parameters, among other methods, to bring about conclusions about the history of a mixture of reprocessing waste batches.

In addition, in the case of complex nuclear programmes, this methodology could help in the reconstruction of information, especially when a portion of the existing records is missing or has become corrupted. Further research is needed, however, to explore this possibility.

Finally, future work in this field should focus on the examination of the method behaviour when information is inconsistent, for instance when a civilian programme with high burnup has been declared, but low burnup campaigns were run, or when the declared history is incomplete, for instance when a programme is older than declared.

7. Acknowledgements

We thank Martin Frank (KIT) and Florian Wellmann (RWTH) for their expertise in Bayesian inference, Gaussian Process Regression and inverse problems. This work has been funded by the Volkswagen Foundation.

8. References

- [1] Glaser, A. and Götsche, M., 'Fissile material stockpile declarations and cooperative nuclear archaeology', in Podvig, P., *Verifiable Declarations of Fissile Material Stocks: Challenges and solutions*, United Nations Institute for Disarmament Research, 2016.
- [2] US Department of Energy, *The United States Plutonium Balance, 1944-2009*, 2012.
- [3] International Panel on Fissile Materials, *Global Fissile Material Report 2010*, 2010.
- [4] Leppänen, J., Pusa, M., Viitanen, T., Valtavirta, V. and Kaltiaisenaho, T., 'The Serpent Monte Carlo code: Status, development and applications in 2013', *Annals of Nuclear Energy*, Vol. 82, 2015, pp. 142-150.
- [5] Gesh, C. J., *A Graphite Isotope Ratio Method Primer — A method for estimating plutonium production in graphite moderated reactors*, Pacific Northwest National Laboratory, Richland, Washington, 2004.
- [6] de Troullioud de Lanversin, J., Götsche, M. and Glaser, A., 'Nuclear archaeology to distinguish plutonium and tritium production modes in heavy water reactors', *Science and Global Security*, Vol. 26, Nos 2/3, 2018, pp. 70-90.
- [7] Götsche, M., de Troullioud de Lanversin, J. and Tietsche-Jaensch, H., 'Examining Reprocessing Waste to Help Estimate Past Plutonium Production', 58th Annual INMM Meeting, 16-20 July 2017, Indian Wells, California.
- [8] Cacucci, D., *Handbook of Nuclear Engineering*, Vol. II, Springer Verlag, 2010.
- [9] Gaugnic, P. A., *Markov Chains: From theory to implementation and experimentation*, John Wiley & Sons, 2017.
- [10] Gelman, A. and Hoffman, M., 'The no-U-turn sampler: adaptively setting path lengths in Hamiltonian Monte Carlo', *Journal of Machine Learning Research*, Vol. 15, 2014, pp. 1593-1623.
- [11] Rasmussen, C. E. and Williams, C. K. I., *Gaussian Processes for Machine Learning*, Massachusetts Institute of Technology, 2006.
- [12] Jones, D. R., 'A taxonomy of global optimization methods based on response surfaces', *Journal of Global Optimization*, Vol. 21, No 4, 2001, pp. 345-383.
- [13] Loyola, D. G., Pedergnana, M. and Gimeno Garcia, S., 'Smart sampling and incremental function learning for very large high dimensional data', *Neural Networks*, Vol. 78, 2016, pp. 75-87.
- [14] Cochran, T. and Arkin, W., *Nuclear Weapons Data-book*, Vol. III, Ballinger Publishing Company, 1984.
- [15] Cozzuol, J. M. and Griggs, D. P., 'TRAC L Reactor Model: Geometry review and benchmarking', Savannah River Laboratory, 1990.
- [16] Savannah River Laboratory, *The Savannah River Site at Fifty*, Savannah River Laboratory, 2000.
- [17] White, A. M., 'MCNP photon transport benchmarking calculations performed at SRP', Annual Meeting of the American Nuclear Society at Atlanta, GA, E. I. du Pont de Nemours and Co, 1989.
- [18] Hamm, J. L. L. and McAllister, J. E., 'Uncertainties affecting BOSFN for the Mark 15 assembly', Savannah River Laboratory, 1983.
- [19] Pedregosa, F., Varoquaux, G., Gramfort, A., Michel, V., Thirion, B., Grisel, O., Blondel, M., Prettenhofer, P., Weiss, R., Dubourg, V., VanderPlas, J., Passos, A., Cournapeau, D., Brucher, M., Perrot, M. and Duchesnay, E., 'Scikit-learn: machine learning in Python', *Journal of Machine Learning Research*, Vol. 12, 2011, pp. 2825-2830.
- [20] Barlow, R. J., *Statistics: A guide to the use of statistical methods in the physical sciences*, John Wiley & Sons, 1999.
- [21] Saltelli, A., Ratto, M., Andres, T., Campolongo, F., Cariboni, J., Gatelli, D., Saisana, M., and Tarantola, S., *Global Sensitivity Analysis: The primer*, John Wiley & Sons, 2008.
- [22] Albright, D., Berkhout, F. and Walter, W., *Plutonium and Highly Enriched Uranium 1996*, Oxford University Press, 1997.
- [23] Salvatier, J., Wiecki, T. V. and Fonnesbeck, C., 'Probabilistic programming in Python using PyMC3', *PeerJ Computer Science*, 2016, 2:e55, doi:10.7717/peerj-cs.55.
- [24] Schilders, W. and van der Vorst, H., *Model Order Reduction: Theory, research aspects and applications*, Springer Verlag, 2008.

Verification of spent fuel inside dry storage casks using fast neutrons

Young Ham, Shivakumar Sitaraman, Phil Kerr

Lawrence Livermore National Laboratory
Livermore, CA 94550
Ham4@llnl.gov

Abstract:

Verification of spent nuclear fuel assemblies within dry storage casks has been a major technical challenge for the safeguards regime for decades. Multiple significant quantities of plutonium are present in a single cask, and spent fuel diverted from the dry storage can be potentially used for nuclear weapons or nuclear terrorism. The amount of spent fuel in dry storage casks is rapidly increasing and is expected to triple in one or two decades. Conventionally, spent fuel accountancy in dry storage relies on containment and surveillance approaches, and there are no reliable technical means to re-verify the casks content once a breach in the continuity-of-knowledge occurs or an intrusion is suspected. Application of non-destructive assay methods is significantly limited by close packing of assemblies in storage configuration and extensive shielding that prevent reliable evaluation of gamma-ray and neutron signatures on the periphery of the cask. Although multiple solutions have been investigated in the past, none of them worked properly. This problem remains as the priority for the IAEA Spent Fuel Verification and Monitoring Programs and national regulatory authorities.

The Lawrence Livermore National Laboratory research team has developed a novel approach to address the verification issue of spent fuel in dry storage casks. A modeling and experimental study investigates a spatially-dependent fast- and epi-thermal neutron flux distribution measured at the top surface of the dry storage cask. The neutron intensity pattern is collected over a grid within a specified energy range, resulting in a set of images that characterize the assembly loading configuration. If a gross defect is present (due to an assembly diversion), the neutron map image unambiguously exhibits a strong deviation from the expected distribution. The project is evaluating a number of candidate fast neutron detectors and conducting a parametric design study for a prototype instrument. It is expected that this verification methodology can be adapted to a variety of spent fuel cask configurations: from typical metal/concrete enclosures for above-ground interim storage to metal capsules designated for deep geological disposal.

Keywords: spent nuclear fuel; dry cask storage; fast neutron spectroscopy; stilbene; liquid scintillator

1. Introduction

Spent fuel in dry storage is vulnerable to diversion, and there are currently no technical means to re-verify the contents of dry storage casks, once seals attached to the dry storage casks are damaged or inadvertently removed from a closed cask. The difficulty arises as no useful gamma rays or neutrons from the inner spent fuel seem to penetrate to the outer side surface where measurements can be performed. Multiple studies in the past based on measuring thermal neutrons or gammas have failed to satisfy IAEA requirements [1-3]. Active interrogation methods using conventional external gamma or neutron sources also are impossible to sufficiently detect diversion because they cannot reach the innermost spent fuel assembly. Although cosmic muons can penetrate through the dry storage casks, use of cosmic muons to address the problem would be very challenging in a real world due to its size (difficult to place between dry storage casks), the extremely long data acquisition time (~3 months per one dry storage cask), difficulty in data interpretation, etc. [4]. This problem of re-verification of the integrity of spent fuel inside dry storage has been one of the most technically challenging problems for many decades facing the IAEA as well as other international safeguards communities such as EURATOM or ABACC, and it remains the top priority for the IAEA Spent Fuel Verification and Monitoring Project, one of the top priority R&D needs in the IAEA R&D Plan (T.1.R6), and one of the immediate objectives under Development and Implementation Support Programme for Nuclear Verification 2018-2019 [5,6].

Lawrence Livermore National Laboratory has embarked upon developing a novel methodology for verification of spent fuel inside dry storage casks through detailed modeling. The verification concept to be developed is based upon collecting and analyzing fast/epi-thermal neutrons coming from the top surface of the dry storage casks. When a set of data is collected with an energy selective/sensitive neutron detector on a grid pattern at the top surface of the dry storage cask, the data can produce a neutron image with epi-thermal neutrons or fast neutrons depending upon what type of neutron is used for data acquisition. In the case of diversion of one or more spent fuel assemblies, the neutron image is expected to show deviation from the typical neutron image. Simulated scenarios using MCNP have demonstrated this behavior.

Having collected the neutron signals from the multiple locations above the subject Dry Storage Cask, one does not rely upon a method of using past measurement results, known as the “fingerprinting” method, because the measured profile can show the diversion in a very clear visual manner.

The first part of this report describes the development of a verification concept by modeling a realistic dry storage cask, and performing Monte Carlo radiation transport calculations. The Castor V/21 dry cask that can hold 21 PWR spent fuel assemblies was selected for this purpose. The second part describes laboratory experiments that support the verification concept performed using a Cf252 source and a stilbene fast neutron detector with Castor V/21 measurement geometry.

2. Monte Carlo modeling

Simulations were performed for a limited set of scenarios using the Monte Carlo N-Particle Transport code (MCNP) [7]. Spent fuel neutron and gamma sources were estimated for PWR 17x17 fuel from an operating reactor. Castor V/21 was selected for our modeling study partially for the reason that Castor type casks are widely used throughout the world, and much of its design information was available in the open documents. More than 1,300 Castor type casks have already been loaded and stored in sites all over the world.

2.1 Spent fuel source term evaluation for Monte Carlo Techniques

Source terms for PWR spent fuel assemblies (SFA) were generated with data obtained from discharged fuel from an actual nuclear power plant. Detailed data on the plant operating conditions were obtained in order to obtain realistic source spectra and isotopics.

Pin by pin burnup estimates were available for a few SFAs. Using this information and the average assembly burnup, pin by pin relative burnup levels were calculated. The average pin power can also be calculated using the assembly average power derived from the power plant data.. Based on these two parameters, the average power generated by each pin was determined. The total irradiation time was obtained by combining the pin power, the absolute pin burnup and the mass of heavy metal in each pin.

Using these data, calculations were performed with a general purpose burnup and decay code, ORIGEN-ARP[8], for each specific burnup using the fuel composition based on the initial enrichment of the SFA . Using the pin power consistent with a burnup level, the initial fuel was burned to that level in discrete time steps over the total number of days of the fuel cycle. A run was made to attain each desired burnup level and decayed to obtain spectra in a 47 group structure for neutrons and 20 group structure for gammas at

various cooling times. The neutron source terms included contributions from both spontaneous fission and (α, n) events. Neutrons produced by subcritical multiplication were accounted for during the radiation transport process. The isotopics (actinides as well as fission products) consistent with the specific burnup were also obtained for various cooling times. All ORIGEN runs were based on the mass contained in one fuel rod.

SFAs with uniform burnup and real assemblies with non-uniform burnups can be composed using this set of data. In the case of this specific 17x17 SFA, several sets of data were obtained. Given below are two sample sets of data: at 35 GWd/t at 20 years cooling time and 56 GWd/t at 17 years cooling time.

For a spent fuel assembly that is at least 2 years old since its discharge, the neutron source is dominated by spontaneous fission from Cm244 which has a half life of 18.1 years, and to a lesser extent from Pu240 with half life of 6561 years. Although the (α, n) component is one to two orders of magnitude less than the spontaneous fission component, the (α, n) component was still included in the LLNL analyses in the estimation of neutron source. Ignoring the neutron source signal from Cm242 with half-life of only 0.5 years is perfectly acceptable as most of this isotope has decayed away by the time the spent fuel assemblies are transferred into dry storage casks. In the unlikely event that spent fuel less than 2 years old is placed into the dry storage cask, the neutron source from Cm242 cannot be ignored. Thus, the overall spectrum resembles that from a fission source. The normalized spectra at burnups of 56 GWd/t and 35 GWd/t are provided below in Figure 1. The two figures are overlapping.

2.2 MCNP modeling with dry storage cask (CASTOR V/21)

The CASTOR V/21 cask was selected for its wide use, and availability here in US for experimental validation of the proposed verification method. The cask is licensed to contain irradiated 14 x 14, 15 x 15 and 17 x 17 PWR fuel assemblies with Zircaloy fuel rod cladding. Total assemblies allowed per cask is less than or equal to 21. A picture of V21 is shown in Figure 2.

Table 1 shows information and parameters of Castor V/21 used for MCNP modeling. MCNP input information used in the modeling was presented in the form of cross-sectional images of a Castor V/21 DSC that holds 21 17x17 PWR spent fuel assemblies and 21 detectors in Figure 3. One can observe the 290 mm thick primary lid and 90 mm thick secondary lid. Those two lids are dominant shielding material for neutrons coming out of the spent fuel assemblies. In order to optimize computer runtime, 21 detectors with 9.76 cm thick polyethylene (from now on poly in this paper) were placed near the top surface of the DSC. The thickness of the poly was restricted by the need to prevent an overlap with

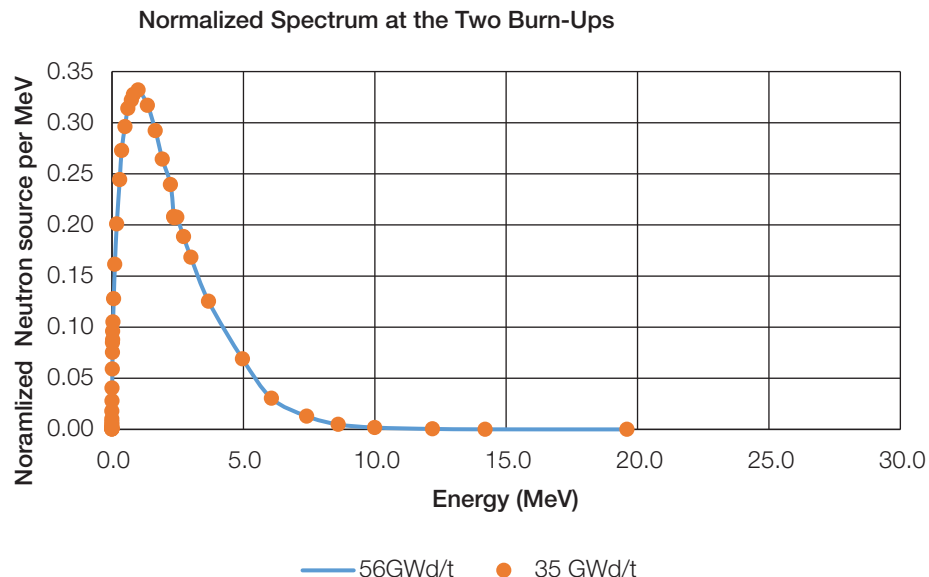


Figure 1: The normalized neutron source spectra used for the MCNP modelling study for both 35 and 56 GWd/t. The two spectra are overlapping.

adjacent detectors in the MCNP model. In actuality this restriction will not apply if only one detector system will be used, allowing the poly thickness to be different. Multiple detectors used simultaneously will obviously have limits on the poly thickness. Every detector was placed directly above the center of the PWR spent fuel assembly. Figure 4 shows a close up view of the axial cross-sectional image in which one can observe fuel rods with plenum region as well as the top nozzles, and the poly (blue region) wrapped detectors (wide black region inside the poly and centered on each SFA).



Figure 2: Picture of Castor V/21 which can accommodate PWR 15x15, 16x16 and 17x17.

Parameter description	Dimension
Overall length of cask	4.866 m (192.4 in)
Cross-sectional diameter of the cask body	2.4 m (94.5 in)
Side wall thickness	37.9 cm (14.9 in)
Length of cask cavity	4.154 m (163.5 in)
Diameter of cask cavity	1.527 m (60.1 in)
PWR spent fuel used	Burnup: 50.76 MWd/kg Cooling time: 17 years
Primary lid thickness	29 cm (11.4 in) stainless steel
Secondary lid thickness	9 cm (3.5 in) stainless steel
Detector cylinder	1 inch radius and 10 cm high
Detector shielding	9.76 cm thick poly
Number of histories in MCNP	9×10^8
Variance reductions applied	Source biasing Geometry splitting
Energy bins used for tally	.4 eV, .5 MeV, 1 MeV, 2 MeV, 5 MeV, 10 MeV, 20 MeV

Table 1: Information and parameters of Castor V21 used for MCNP

With MCNP input parameters described above, two cases were studied in order to investigate the proposed concept of using different neutron energy ranges to detect the diversion of a spent fuel assembly. One case was run with the dry storage cask filled with all 21 spent fuel assemblies. Every spent fuel assembly had a burn-up of 56 GWd/t and 17 years of cooling time. Another case was run with the same condition but with the center assembly replaced with a dummy stainless-steel assembly. This means that the detector 2001 (see Figure 5) would be directly above the diverted spent fuel assembly.

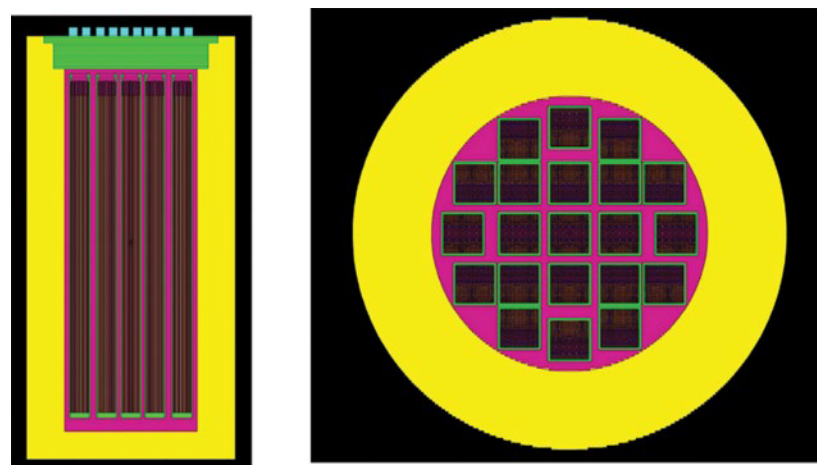


Figure 3: Cut away views of fully loaded CASTOR with 21 17x17 PWR spent fuel assemblies as modeled in MCNP.

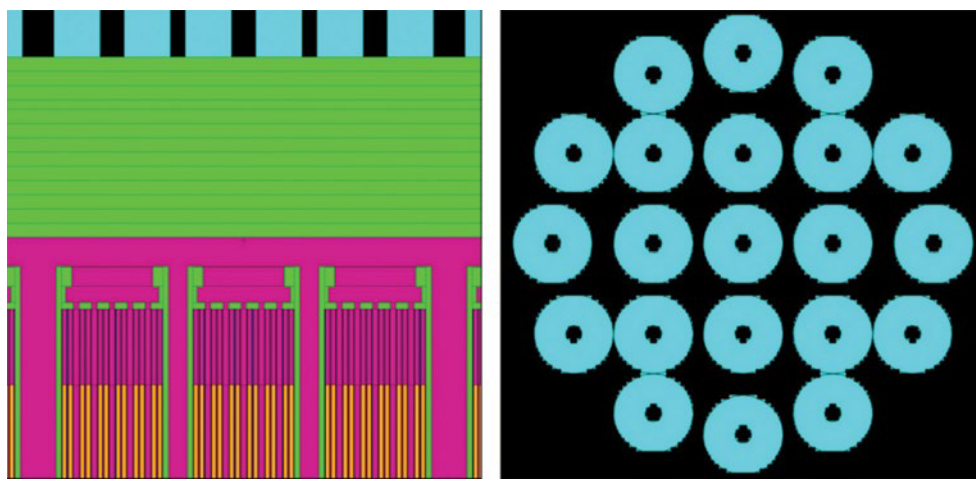


Figure 4: Close up cross-sectional view of MCNP set up. The neutron detectors with poly around them are positioned on the top surface of the CASTOR 21. Every detector is located directly above the center of the PWR spent fuel assembly.

2.3 MCNP Results and Discussions

The MCNP results were tabulated using the format shown in Figure 5 below. The left image indicates the five detectors used to generate the flux profile. The numbers in the right image indicate the number used to designate each detector (tally region) where the flux was calculated. Figure 6 shows the MCNP results in a 2D surface plot. The left plot of Figure 6 is obtained for the case of non-diversion whereas the right plot is for the case of diversion where the center assembly was replaced with a dummy stainless steel assembly. Note that how the center part of the surface plot deviated from the non-diversion case.

Table 2 presents the tally results at the 5 detectors in the center vertical line of the basket (see Figure 5) as a function of neutron energy with all 21 spent fuel assemblies whereas Table 3 presents the results when the center

assembly (corresponding to detector 2001) is replaced with a dummy stainless-steel assembly. Figure 7 shows the vertical tally profiles, i.e., detector tally through 2003-2002-2001-2004-2005, as the energy tally bin increases. One can observe a cosine-like shape for the case of no diversion. (The last plot in Figure 7, which corresponds to the tally for the neutron energy 10-20 MeV, did not show a cosine-like shape as the statistical uncertainty for that value was too high. You can find this information in Table 4.) Note how the vertical tally profile obtained with a diversion (orange line) deviates further from the profile with no diversion (blue line) as neutron energy increases. In particular, the profiles with the neutron energies above 1 MeV can visually demonstrate the case of a diversion. This profile method can be a powerful tool as the methodology detects a diversion and it does not require earlier measurement for comparison as in the fingerprinting method.

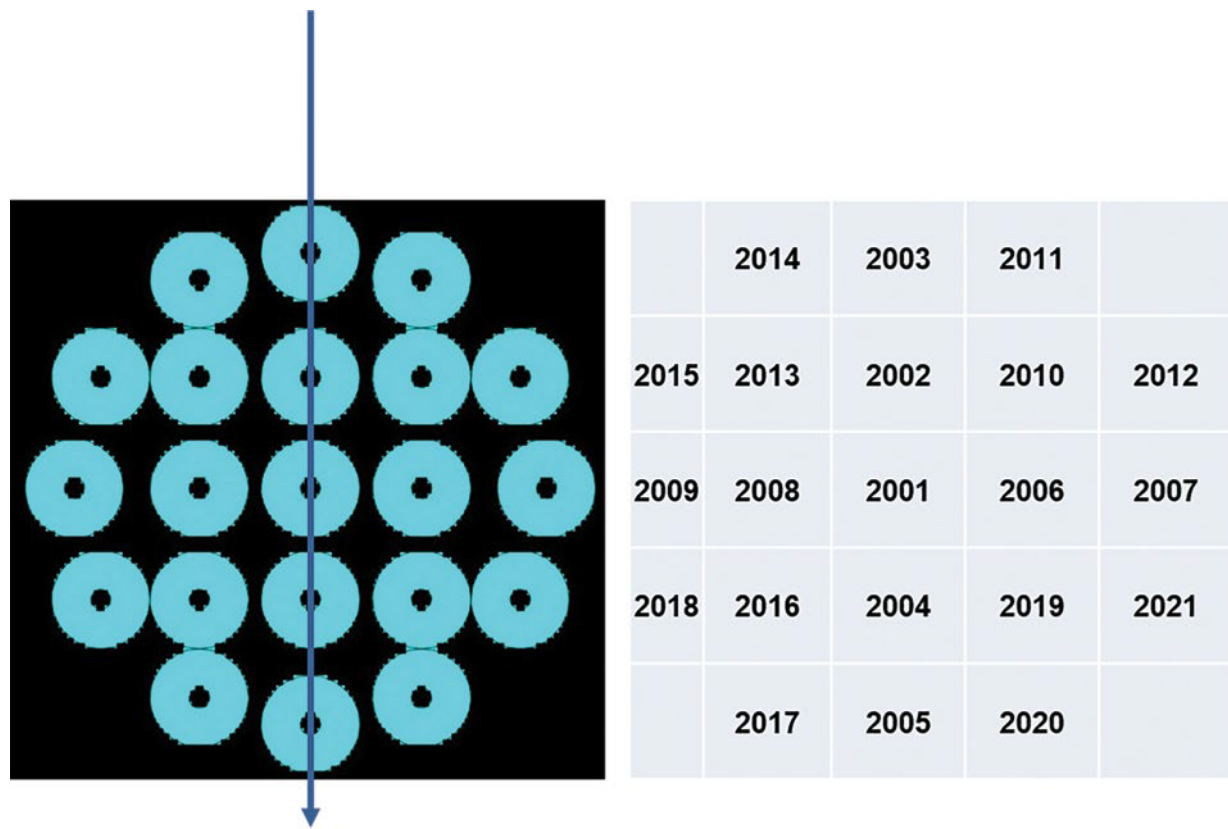


Figure 5: The left figure indicate how data were read and shown as a graph later for easy analysis and results presentation. The numbers in the right figure indicate neutron tally (detector) number which is essentially relative neutron flux.

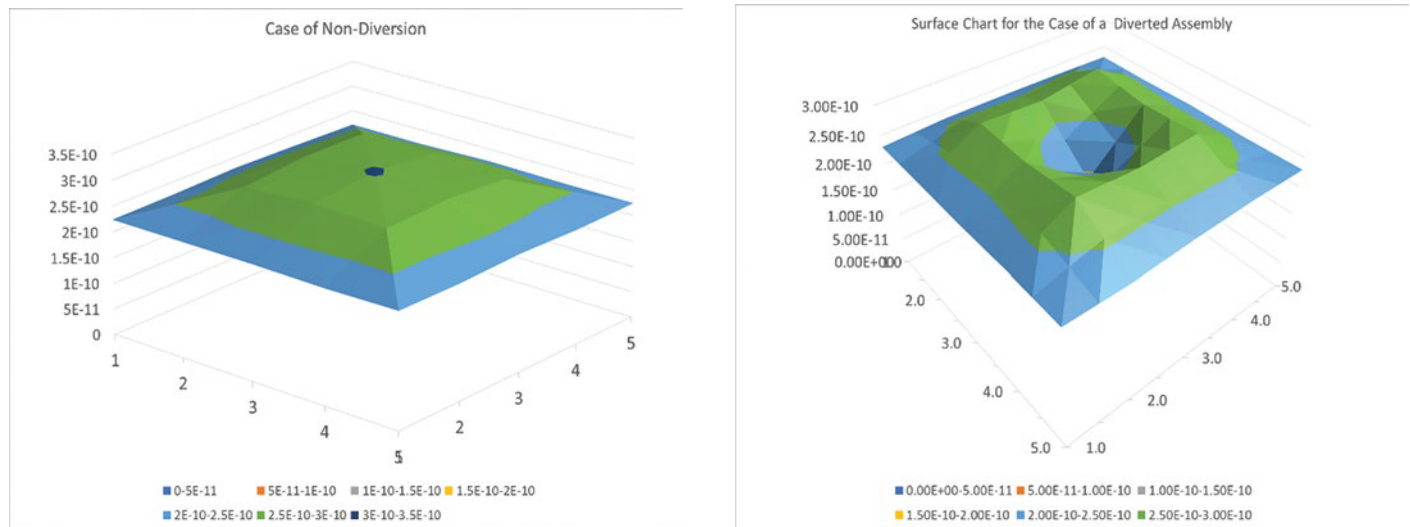


Figure 6: The left figure is obtained for the case of non-diversion. The right figure is for the case where the center assembly was replaced with a dummy stainless steel assembly. Note the deviation in the center in the right figure.

Table 4 shows the neutron tally at the detector 2001 for the case of non-diversion as well as the case with the diversion of an assembly at the center. While the neutron detector tally decreases exponentially with increasing energy, the difference in the flux between the non-diverted and diverted case increases with increasing energy. The amount of deviation, ϵ , is defined as $\epsilon = (\text{neutron tally with no diversion} - \text{neutron tally with diversion of an assembly that is subject to verification}) / \text{neutron tally with no diversion}$

The deviation is a useful quantitative indicator of the diversion of an assembly. The amount of deviation was plotted in terms of neutron energy in Figure 8. For example, if one uses a neutron detector that measures neutron energy in the 2-5 MeV, the relative difference would be 36.4%

It is important to note that the tally used in the MCNP simulation did not account for detector efficiency as the choice of the ideal fast neutron detector to be implemented in the verification tool has not been determined yet.

Neutron Energy	Tally (Detector) Data for fully intact assemblies				
	2003	2002	2001	2004	2005
0 - 0.4 eV	4.16E-07	5.84E-07	6.29E-07	5.83E-07	4.16E-07
0.4 eV - 0.5 MeV	3.80E-07	5.34E-07	5.75E-07	5.33E-07	3.80E-07
0.5-1 MeV	1.38E-08	1.96E-08	2.10E-08	1.95E-08	1.37E-08
1-2 MeV	1.92E-09	2.65E-09	2.76E-09	2.64E-09	1.92E-09
2-5 MeV	2.24E-10	2.88E-10	3.02E-10	2.92E-10	2.26E-10
5-10 MeV	3.05E-11	3.85E-11	3.95E-11	3.83E-11	3.07E-11
10-20 MeV	1.74E-12	2.00E-12	2.14E-12	2.34E-12	1.93E-12
Total	8.12E-07	1.14E-06	1.23E-06	1.14E-06	8.11E-07

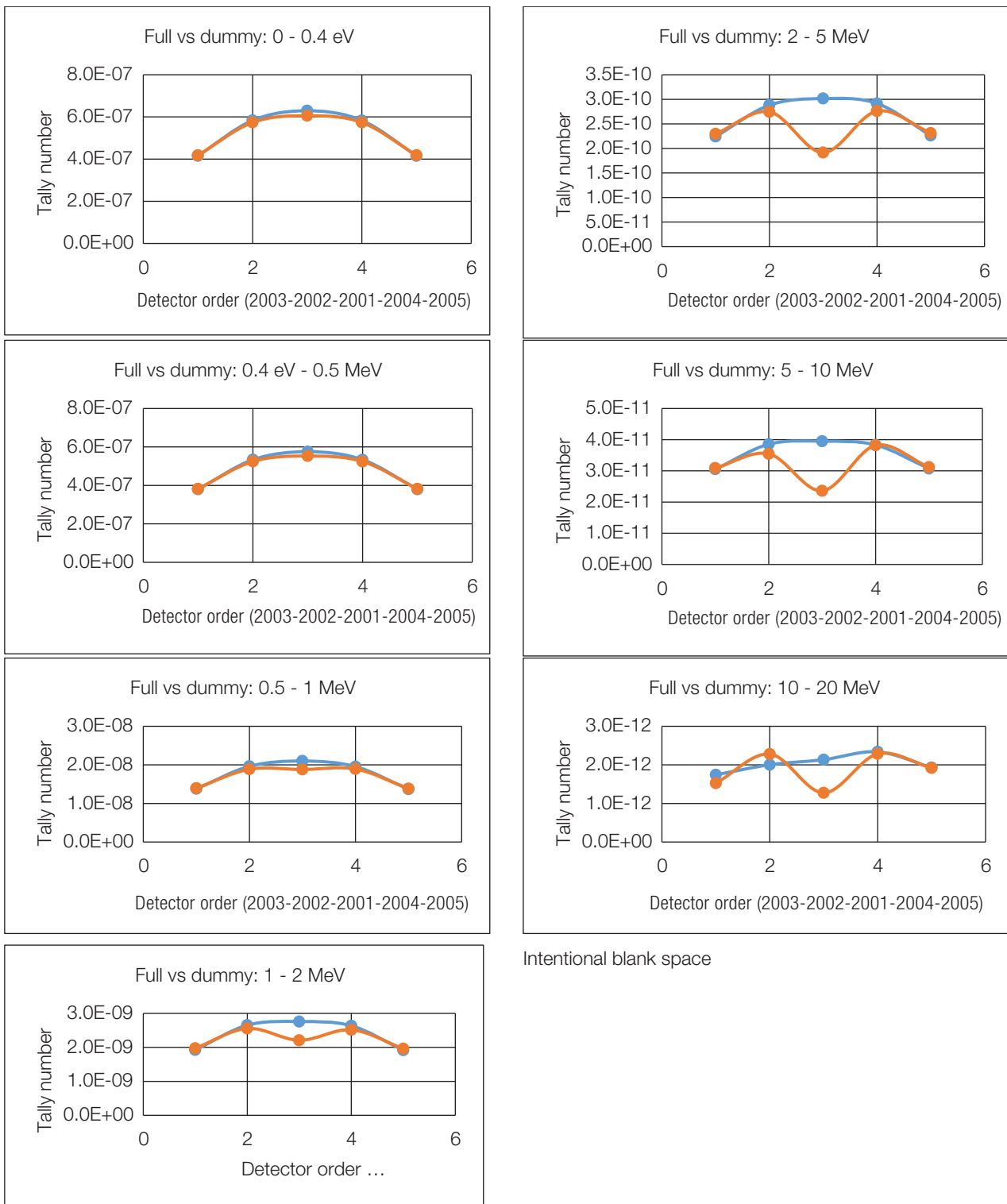
Table 2: Tally at vertical center 5 detectors as a function of neutron energy with full intact assemblies.

Neutron Energy	Tally (Detector) Number for missing central assembly (2001)				
	2003	2002	2001	2004	2005
0 - 0.4 eV	4.18E-07	5.74E-07	6.06E-07	5.74E-07	4.18E-07
0.4 eV - 0.5 MeV	3.82E-07	5.25E-07	5.53E-07	5.24E-07	3.82E-07
0.5-1 MeV	1.40E-08	1.89E-08	1.88E-08	1.89E-08	1.38E-08
1-2 MeV	1.97E-09	2.56E-09	2.21E-09	2.52E-09	1.96E-09
2-5 MeV	2.30E-10	2.75E-10	1.92E-10	2.76E-10	2.31E-10
5-10 MeV	3.09E-11	3.55E-11	2.36E-11	3.82E-11	3.12E-11
10-20 MeV	1.52E-12	2.28E-12	1.28E-12	2.29E-12	1.92E-12
Total	8.16E-07	1.12E-06	1.18E-06	1.12E-06	8.16E-07

Table 3: Tally at vertical center 5 detectors as a function of neutron energy with the center assembly replaced with a dummy stainless-steel assembly.

Cell	2001 (Full)		2001 (Diverted)		Deviation (ϵ)
Neutron Energy (MeV)	Tally	Error	Tally	Error	
0 - 0.4 eV	6.29E-07	0.07%	6.06E-07	0.07%	3.66%
0.4 eV - 0.5	5.75E-07	0.07%	5.53E-07	0.08%	3.83%
0.5-1	2.10E-08	0.24%	1.88E-08	0.25%	10.5%
1-2	2.76E-09	0.55%	2.21E-09	0.76%	19.9%
2-5	3.02E-10	0.89%	1.92E-10	1.21%	36.4%
5-10	3.95E-11	2.12%	2.36E-11	3.13%	40.3%
10-20	2.14E-12	8.55%	1.28E-12	14.24%	40.2%
Total	1.23E-06	0.07%	1.18E-06	0.07%	3.90%

Table 4: Neutron intensity, the tally at detector 2001, for the case of non-diversion and the case with the diversion of an assembly at the center. Relative difference can be interpreted as deviation.



Intentional blank space

Figure 7: Vertical tally profiles, i.e., detector tally through 2003-2002-2001-2004-2005, as the energy tally bin increases.- The blue curve is the cask with all 21 assemblies and the orange curve is when the center assembly has been replaced with a stainless steel dummy assembly.

3. Experiments

An experiment was set up in the laboratory to validate the verification concept as a precursor before doing actual validation measurements at a dry storage cask site. The measurement geometry was arranged to mimic the data acquisition for the dry storage measurement environment (see Figure 9.) For the experiments, a stilbene detector, was selected as one of the several fast neutron detectors to be studied, to obtain fast neutron signals due to their high efficiency, commercial availability in large sizes, and good characterization of gamma discrimination by use of pulse shape discrimination (PSD). As stilbene is known to be very responsive to gamma rays, PSD application to the measured data is critically important to assess neutron signals. The PSD method is based on the difference in the decay time of fluorescence emitted within an organic scintillator as a result of a reaction

between the ionizing particle and the scintillator. The fluorescence decay time for heavy particles, such as protons, or neutrons is much longer than that of electrons.

The data acquisition system, shown in figure 9, consists of a Fast Comtec MPA-3 four channel multiparameter system, and a Mesytec MPD-4 pulse shape discriminator unit. The MPD-4 unit examines the time structure of the electrical pulse from the PMT to discriminate between neutrons and gamma rays that interact with the stilbene scintillator.

As shown in Figure 9, a 4-inch diameter, 2-inch deep stilbene was used to collect one set of data when the Cf252 was placed directly below the detector in the center of the collimator space (position 1), and another set of data when the Cf252 placed at the off-collimator position (position 2). The detector was placed at 8.5 cm above the top surface of the

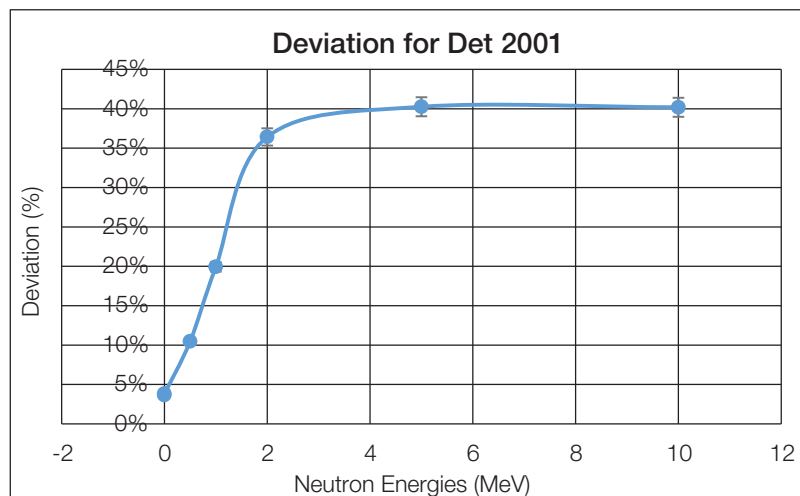


Figure 8: Deviation for detector 2001 in terms of neutron energy. Note how the deviation increases rapidly as neutron energy increases. Here deviation shows the degree of deviation from the case of non-diversion.

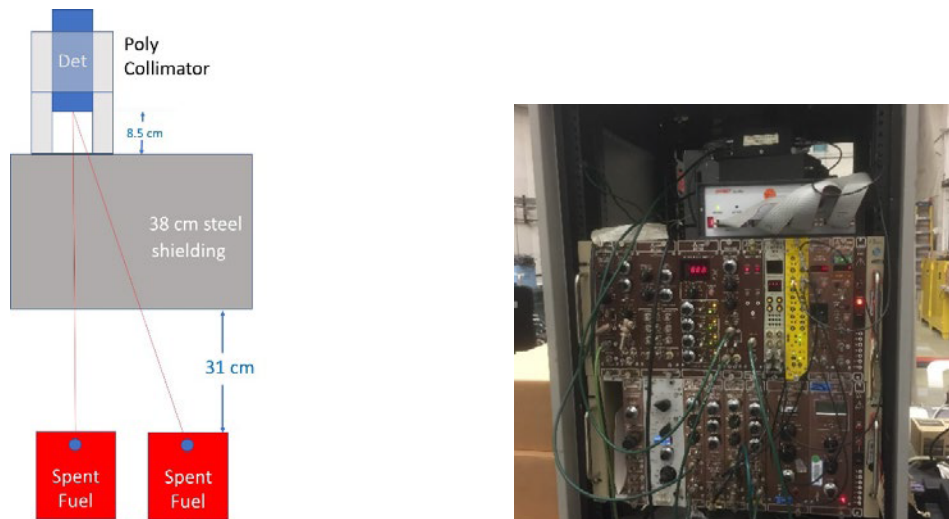


Figure 9: Experimental set up and data acquisition electronics. The two red boxes indicate the position and dimension of spent fuel assemblies in the dry storage casks in scale, although no spent fuel was used in the actual measurements. The two blue circles represent the Cf source position. The picture on the right shows the Fast Comtec MPA-3 four channel multiparameter system on the top, and a Mesytec MPD-4 pulse shape discriminator unit in the NIM bins.

steel inside the cavity of a poly collimator. Each set of data was collected over a measurement time of 1 day. The distance between the two Cf252 source positions was set to be at 27.75 cm representing actual pitch of two adjacent SFAs on the center line of two SFAs as stored in the Castor cask.

4. Results and data analysis

PSD plots obtained with the stilbene scintillator using PSD electronics for the case of a Cf252 source placed directly below the detector and the source at the off-collimator position are shown in Figure 10. The neutron signals were attenuated by 38 cm of steel which is the thickness of the Castor V/21 lids. The upper neutron band signals were well separated from the lower gamma band signals.

Note that in the PSD plots in Figure 10, the neutron signal bands contain energy information, but they do not represent the direct neutron energy information. Thus, the

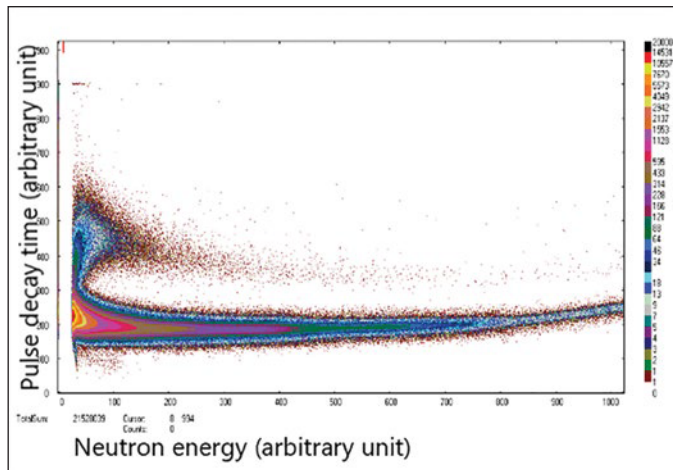


Figure 10: PSD plots obtained with the stilbene scintillator using PSD electronics for the case of Cf source placed directly below the detector and the source off the collimator position. The radiations were attenuated by 38 cm of steel. The upper neutron band signals were well separated from the lower gamma band signals.

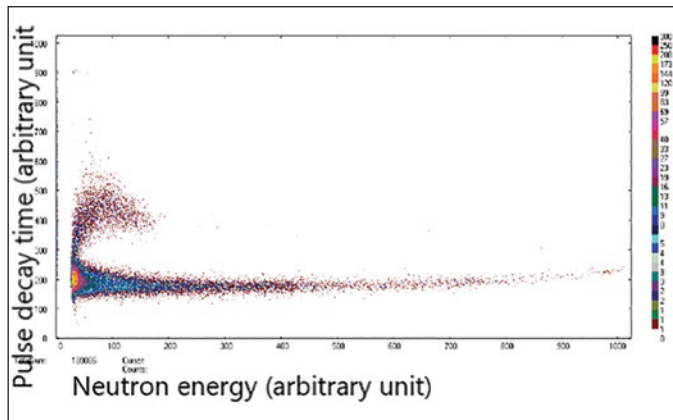
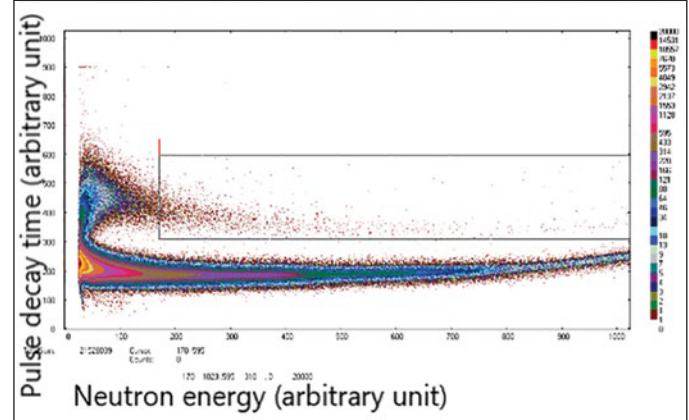
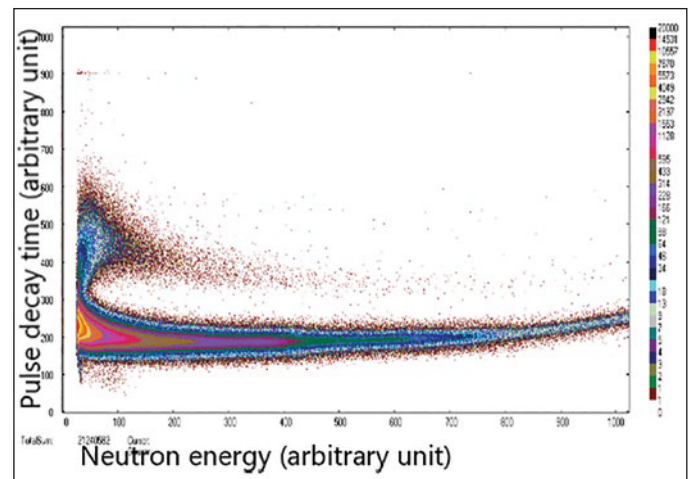


Figure 11: PSD plot in the left obtained with the stilbene scintillator using PSD electronics and DD 2.4 MeV neutrons. Note that there is a distinctive end of neutron band, showing a feature that can be useful to separate neutron signals. The information is used to select a rectangular ROI that predominantly has neutrons with energy greater than approximately 2.4 MeV. An example of ROI selection is shown in the right plot.

PSD plots cannot be treated as neutron energy spectra requiring unfolding of the PSD plots. As the process of unfolding spectra requires substantial effort and is perhaps cumbersome to apply for verification, a method was explored for the PSD plots to be directly applicable for verification. As our verification methodology requires information on the energy of neutrons that come into the detector, particularly, the energy threshold of 1 MeV or 2 MeV in the measured spectra produced by poly-energetic neutron source, i.e. spent fuel, an effective neutron calibration method is needed. One approach that was adopted is making use of a D-D neutron generator knowing that it produces near monoenergetic neutrons at approximately 2.4 MeV.

The left plot in Figure 11 shows the PSD plot produced by stilbene with the use of a D-D 2.4 MeV neutron generator. Observe a distinctive end of neutron band that ends in near channel 170, a feature that can be useful to separate



neutron signals below 2.4 MeV for the data obtained with poly-energetic neutron source such as Cf252 or spent fuel. Using this piece of information, the region of interest (ROI) was selected to capture neutrons above 2.4 MeV from the PSD plots obtained at two source positions (see the right plot in Figure 11.)

The neutron counts in the ROIs were found to be 8051 +/- 1.2% and 5753 +/- 1.3% with background subtraction respectively for source position 1 (on collimator axis) and position 2 (off collimator axis). This corresponds to a difference in neutron signals by 27.7%. The amount of deviation in the actual V/21 arrangement is difficult to estimate with this value alone as all assemblies contribute to the total counting, and due to the difference in source geometry and source strength between Cf252 and actual spent fuel assemblies. However, substantially measurable difference in the neutron strength is expected in the case of a diversion of an entire assembly. The experimental result will be improved by selecting a smaller diameter stilbene, a thicker collimator and the optimal position of the detector. Further experiments are in progress.

The results obtained in these experiments showed that verification of spent fuel inside dry storage casks is possible by use of stilbene and a simple 2.4 MeV energy threshold method. The results are also consistent with MCNP modeling results, although a direct comparison of the experimental results with the MCNP modeling results was not possible due to different geometry and the inability of using actual spent fuel in the experiments in the lab environment. Besides the stilbene, several different types of fast neutron detectors are also being explored as a potential fast neutron detector to be a part of the verification system for spent fuel in dry storage casks. Preliminary data using a liquid scintillator, EJ-309, showed similar results as those from the stilbene detector.

5. Conclusions

A novel methodology was proposed and validated by simulation and laboratory experiments to address the long unsolved technical problem of verification of spent fuel inside dry storage casks. The verification concept uses an energy selective neutron detector measuring neutron signals on a grid pattern at the top surface of the dry storage cask. In the case of diversion of one or more spent fuel assemblies, the neutron image is expected to show a deviation from the typical neutron image. The verification method is intuitive, easy to interpret, and does not rely upon any past measurement results. Simulated scenarios using MCNP have demonstrated this capability. Simplified laboratory experimental results using Cf252 and a stilbene scintillator showed that the proposed methodology is indeed very promising.

6. Acknowledgements

This work was sponsored by the US Department of Energy, National Nuclear Security Administration, Office of Nonproliferation and Arms Control, International Nuclear Safeguards program, and performed under the auspices of the US Department of Energy by Lawrence Livermore National Laboratory under Contract DE-AC52-07NA27344.

7. References

- [1] Ziock, K., Vanier, P., Forman, L., Caffrey, G., Wharton, J. and Lebrun, A., 'The feasibility of cask "fingerprinting" as a spent-fuel, dry-storage cask safeguards technique', UCRL-TR-215943, 2005.
- [2] Jayson Wharton, C., Seabury, E. H., Caffrey, A. J. and Winston, P. L., *Summary Report: INL CDCIS cask scanner testing at Doel, Belgium*, 2013.
- [3] Santi, P. A., Browne, M. C., Freeman, C. R., Parker, R. F. and Williams, R. B., 'Initial measurement of BN-350 spent fuel in dry storage casks using the dual slab verification detector', LA-UR-10-03849, 51st INMM Annual Meeting, Baltimore MD, 2010.
- [4] Durham, J. M., Poulson, D., Bacon, J., Chichester, D. L., Guardincerri, E., Morris, C. L., Plaud-Ramos, K., Schwendiman, W., Tolman, J. D. and Winston, P., 'Verification of spent nuclear fuel in sealed dry storage casks via measurements of cosmic-ray muon scattering', *Physical Review Applied*, Vol. 9, No 4, 044013, 2018.
- [5] International Atomic Energy Agency, STR-385, *Research and Development Plan*, Vienna, 2018.
- [6] International Atomic Energy Agency, STR-386, *Development and Implementation Support Programme for Nuclear Verification 2018-2019*, Vienna, 2018.
- [7] Werner, C. J. (ed.), *MCNP Users Manual — Code Version 6.2*, Los Alamos National Laboratory, 2017.
- [8] Reardon, B. T. and Jeesee, M. A. (eds), *Scale Code System, Version 6.2.3*, ORNL/TM-2005/39, Oakridge National Laboratory, 2018.

Development and examination of a proliferation trade risk metric

Adam Attarian, Peter Heine, Amanda Sayre

Pacific Northwest National Laboratory
1100 Dexter Ave N Seattle, WA 98148
Email: peter.heine@pnnl.gov
PNNL-SA-143116

Abstract:

A Proliferation Trade Risk metric has been calculated for each country represented in a publicly-available global trade dataset. This metric, comprising both direct and indirect proliferation trade risk components, represents the risk that each country's proliferation-relevant exports will go to a designated set of proliferation threat countries. This metric can serve to prioritize non-proliferation export control capacity building engagement. Further, within such engagement, the decomposition of the proliferation trade risk metric can identify specific industrial sectors and trade relationships of greatest importance for outreach and enforcement measures. Finally, these supply-side perspectives can be complemented by threat-based profiles identifying the most important suppliers to each threat country.

Keywords: export controls; trade analysis; non-proliferation; outreach; capacity building, risk management

1. Introduction

In 2018, the US National Nuclear Security Administration's International Nonproliferation Export Control Program (IN-ECP) replaced the qualitative trade-based metrics used in its engagement planning process using the publicly available trade data that underlies the Strategic Trade Atlas developed jointly with the European Commission's Joint Research Centre.¹ [1,2]. A Proliferation Trade Risk metric was developed which can be calculated from the BACI data given a set of proliferation threat countries and a set of proliferation-relevant goods. Proliferation Trade Risk was calculated using six countries identified as WMD threats by the 2019 National Intelligence Strategy [3], the 2017 National Security Strategy [4], and the 2018 Nuclear Posture Review [5]. Specifically, these were China, Iran, North Korea, Pakistan, Russia, and Syria, but the methodology can be used for other sets of countries or goods of concern as appropriate for various threat assessments. At the time this metric was developed, it was computed using BACI

data for the year 2016 but has since been computed for each year between 1995 and 2016 inclusive.

The Proliferation Trade Risk metric is demand-driven, meaning that trade flows are scored based on their importance to the recipient of the trade rather than the supplier, as will be shown in the Methodology section of this paper below. This can have surprising results, where trade flows seeming small to a supplier may represent significant proliferation trade risk because they constitute a large fraction of a threat country's imports of that commodity, or a large fraction of the imports into an intermediary which is also an important direct supplier of that commodity to one or more threat countries. Once computed, the analysis can support engagement prioritization decisions, and deconstructing the components of the metric can suggest highest risk trade flows and industrial sectors on which to focus risk reduction efforts.

2. Methodology

Given a set of designated proliferation threat countries of concern, a Proliferation Trade Risk (PTR) score can be computed for each country in the BACI dataset. The Proliferation Trade Risk score for each country is a measure of the risk that the country's proliferation-relevant exports² will go to a threat country, directly or indirectly. As such, it comprises two terms: Direct Proliferation Trade Risk (D) and Indirect Proliferation Trade Risk (I). Note that proliferation-relevant trade represents the types of goods most likely to include export-controlled items, but it does not necessarily indicate trade in controlled items. For example, trade in commodities classified as pumps is most likely to include export-controlled pumps, but most pumps are not export controlled. The intent is not to identify specific trade flows of proliferation interest, but to identify the regular trading relationships with the greatest proliferation risk.

¹ This BACI dataset, which is used extensively in academic trade analyses, is a statistical elaboration of UN COMTRADE that reconciles import and export declarations to enhance the completeness and reliability of the data. http://www.cepii.fr/cepii/en/bdd_modele/presentation.asp?id=1

² Proliferation-relevant trade excludes goods classified under Harmonized System (HS) chapters unlikely to correspond to proliferation-relevant commodities, such as agricultural products, wood products, fossil fuels, apparel, etc. While proliferation trade risk can be calculated using any basket of goods, this analysis used trade classified under HS Chapters 28 and 29 (chemicals), 75 (aluminum), 76 (nickel), 81 (other/exotic base metals), 84 (machinery), 85 (electronics), and 90 (measurement and test equipment). These selections are configurable and easily modified as needed.

2.1 Direct Proliferation Trade Risk (D)

The Direct Proliferation Trade Risk posed by a supplier country is a measure of the risk that the country's proliferation-relevant exports will go directly to a threat country. It is a demand-driven metric calculated as the sum of the fraction of each threat country's proliferation-relevant imports that come from the supplier.

$$D_{\text{supplier}} = \sum_{\text{threat countries}} \frac{V_{\text{supplier}, \text{threat country}}}{V_{\text{threat country}}} \quad (1)$$

where

$V_{\text{supplier}, \text{threat country}}$ is the value of proliferation relevant trade exported from the supplier to the threat country and $V_{\text{threat country}}$ is the total value of proliferation relevant trade imported by the threat country.

2.2 Indirect Proliferation Trade Risk (I)

The Indirect Proliferation Trade Risk posed by a supplier country is a measure of the risk that the country's proliferation-relevant exports will go indirectly to a threat country via one or more intermediary countries. Intermediate countries are identified in the data as countries receiving proliferation-relevant goods from the supplier and exporting proliferation-relevant goods to threat countries. It is calculated as the sum of the fraction of each intermediary country's proliferation-relevant imports coming from the supplier multiplied by the intermediary country's Direct Proliferation Trade Risk (D), which captures the risk that proliferation-relevant goods exported by that country would go to a threat country.

$$I_{\text{supplier}} = \sum_{\text{intermediary countries}} \frac{V_{\text{supplier}, \text{intermediary}}}{V_{\text{intermediary}}} D_{\text{intermediary}} \quad (2)$$

Thus, exports from a supplier to a potential intermediary only contribute to Indirect Proliferation Trade Risk if that intermediary also exports proliferation-relevant trade directly to threat countries, and the contribution is proportional to the fraction of the intermediary's imports coming from the supplier and the threat countries' imports coming from the intermediary.

2.3 Computation

The Direct and Indirect Proliferation Trade Risks can quickly and efficiently be calculated using matrix algebra with the BACI dataset. To facilitate computation, we construct a matrix v_{ij} with column i and row j where each entry is the total value of proliferation relevant trade from export country i to import country j . The total value of proliferation relevant trade V for a given threat country is simply the sum of that country's column in the trade matrix and is represented by a column vector with N entries. Using matrix index notation, equations (1) and (2) become

$$D = v[:, coc] \times (1/V[coc])^T, \quad (3)$$

$$I = (v \times (1/V)) D, \quad (4)$$

where \times denotes element-wise multiplication and coc denotes the column indices corresponding to the countries

of concern. The direct trade risk vector D is then zero for all countries except countries of concern, whereas I is fully populated for each country assuming relevant trade. The PTR is given as the sum of I and D .

2.4 Known issues

While BACI attempts to reconcile incomplete or missing trade reports, the data is inherently noisy. Some countries report many thousands of import and export records per year, while other countries provide only sporadic and sparse reporting. This methodology becomes very sensitive when total reported proliferation-relevant imports into a country are small. Because the total value of proliferation relevant trade is in the denominator, when this value is small, relatively small trade flows can generate large proliferation trade risk scores. In general, this appears to be a strength of the methodology, as it successfully highlights small but unusual trade flows that may indicate import and re-export to threat countries via intermediaries. In addition, trade with intermediary countries with zero Direct Proliferation Trade Risk ($D = 0$) offers no additional Indirect Trade Risk, even though those intermediary countries may have non-zero indirect trade risk. This "second-order risk" (i.e., the risk of trade flows to threat countries via multiple intermediaries) is currently ignored, but preliminary investigation indicates this has only small impacts on the results.

3. Results

Figure 1 shows the computed Proliferation Trade Risk scores over time, and Figure 2 shows normalized Direct and Indirect Proliferation Trade Risk scores for each country in the BACI dataset for the year 2016. China (CN) had the highest Direct and Indirect Proliferation Trade Risk by far. A cluster of four countries, Germany (DE), South Korea (KR), Japan (JP), and the United States (US), represented the next level of Proliferation Trade Risk.

Excluding these top 5 risks, Figure 3 shows more clearly the raw Direct and Indirect Proliferation Trade Risk scores for the remaining countries for 2016. Of these, the United Arab Emirates (AE), Italy (IT), Turkey (TR), and India (IN) were the top Direct Proliferation Trade Risks, while Malaysia (MY), Singapore (SG), Vietnam (VN), Italy (IT), France (FR), Thailand (TH), the Netherlands (NL), the United Kingdom (UK), and the Philippines (PH) had the highest Indirect Proliferation Trade Risks. Italy (IT) was high on both measures, indicating significant direct exports to threat countries and significant exports to intermediaries with significant exports to threat countries.

In Figure 3, a third cluster of countries found to have elevated Proliferation Trade Risk includes Russia (RU), Belgium (BE), Switzerland (CH), Czech Republic (CZ), Austria (AT), Poland (PL), Hong Kong (HK), Spain (ES), Sweden

PTR over time

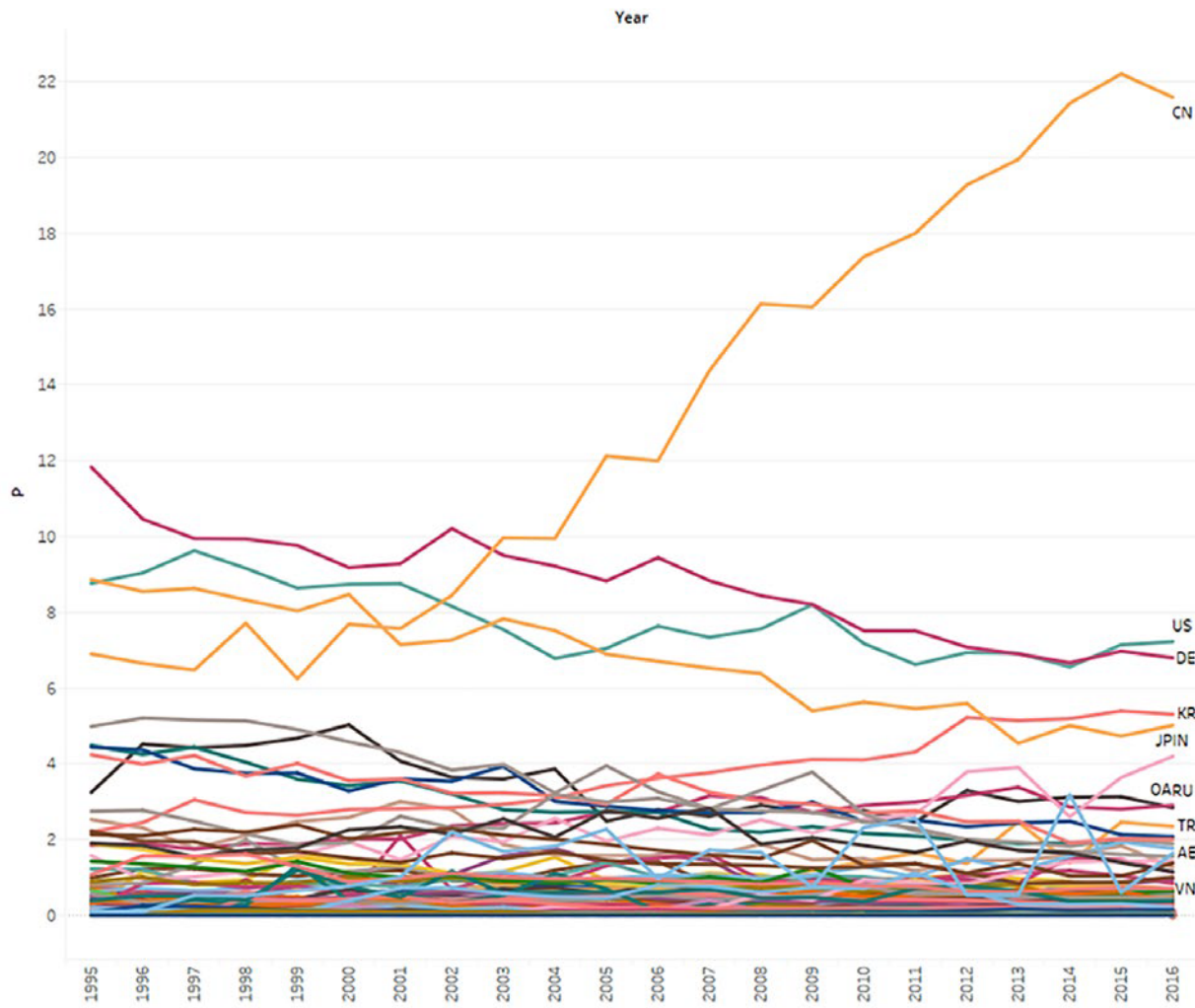


Figure 1: Proliferation Trade Risk over time.

Direct and Indirect Proliferation Trade Risks

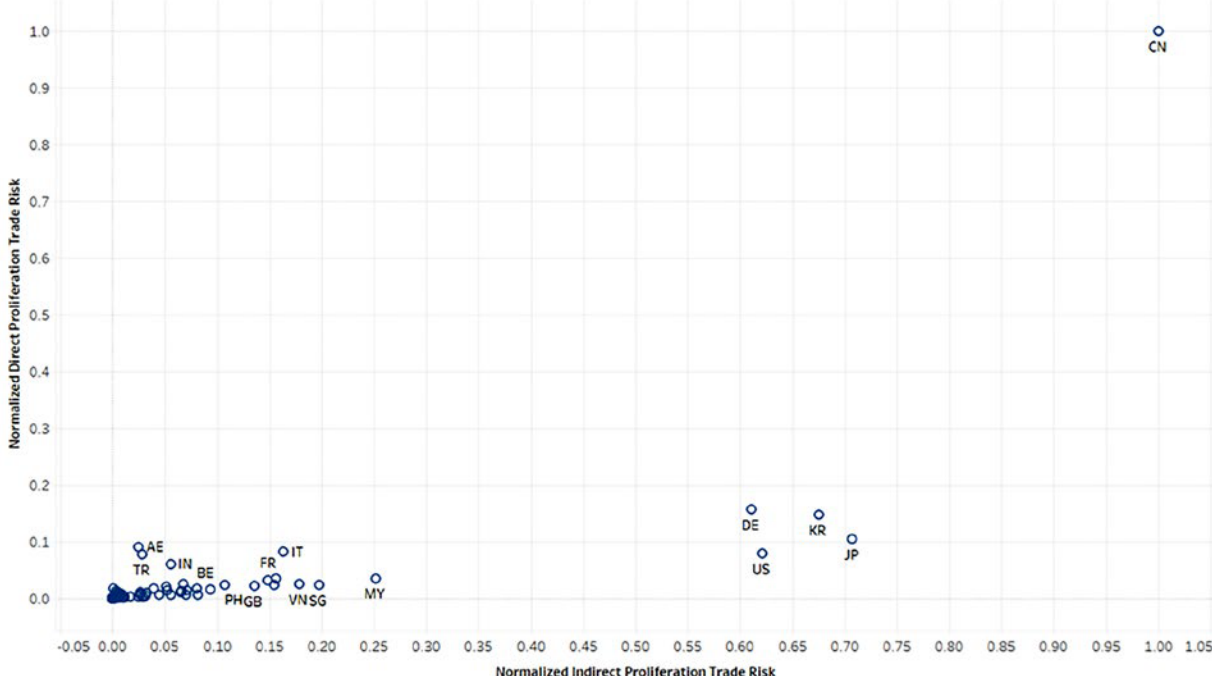


Figure 2: Normalized Direct and Indirect Proliferation Trade Risks for 2016.

Direct and Indirect Trade Risks **excluding CN, DE, KR, JP, and US**

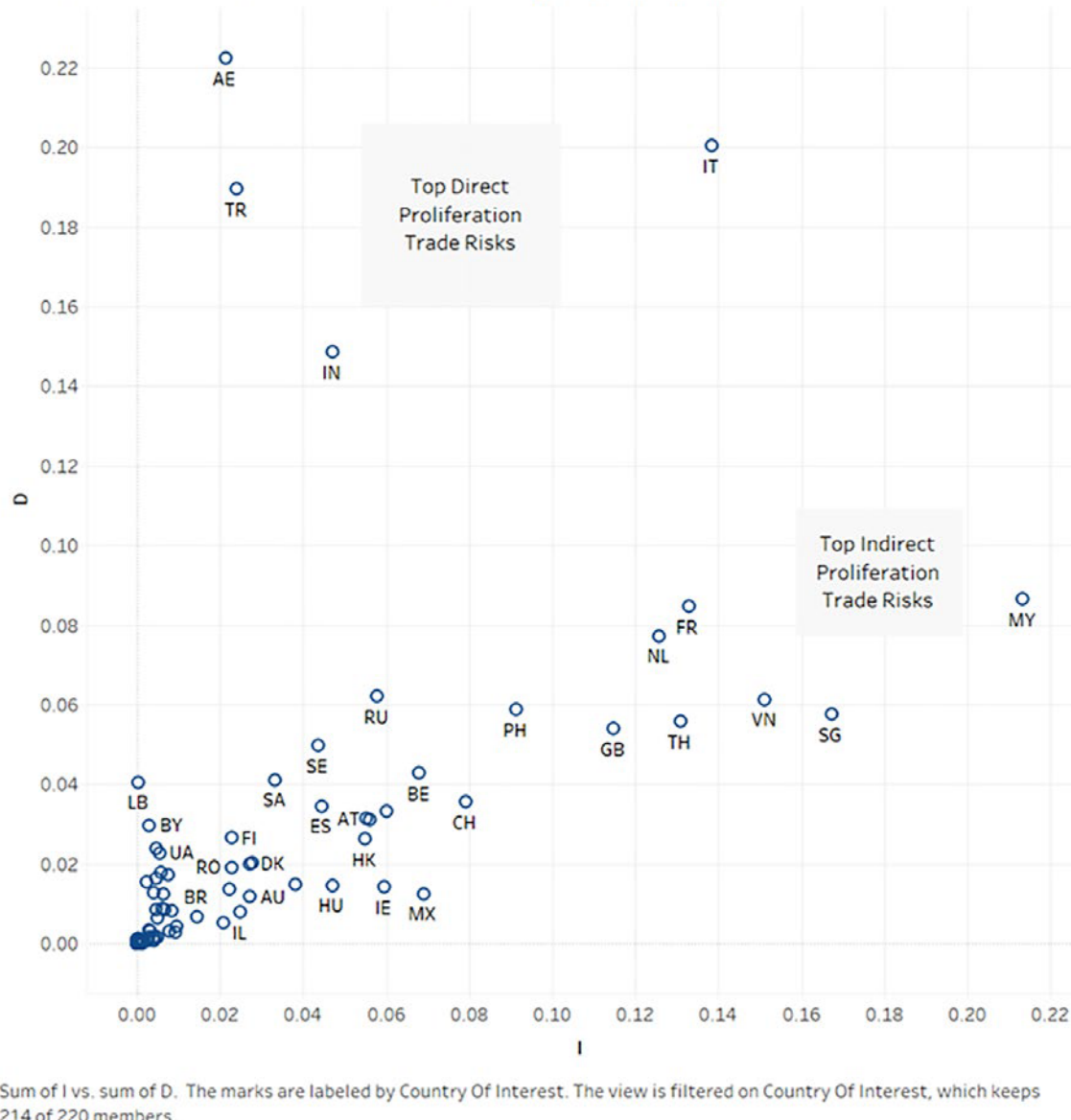


Figure 3: Direct and Indirect Proliferation Trade risks for 2016, excluding China, South Korea, Germany, Japan and the United States.

(SE), Saudi Arabia (SA), Canada (CA), Finland (FI), Indonesia (ID), Denmark (DK), Belarus (BY), and Lebanon (LB).

4. Decomposition of Proliferation Trade Risk for individual countries

In addition to providing an overall scoring mechanism for ranking and comparing countries, these computations also provide a means for better understanding the specific proliferation risks faced by individual supplier or intermediary countries. For example, the Proliferation Trade Risk for Jordan (JO) can be broken down as shown in **Figure 4**, which shows the contributions of each export destination to Jordan's Proliferation Trade Risk score. It shows that Jordan's Proliferation Trade Risk derives primarily from direct exports of proliferation-relevant goods to Syria (SY) and Pakistan (PK), followed by indirect trade risk from proliferation-relevant exports to

India. Syrian imports from Jordan make a large contribution to Jordan's Proliferation Trade Risk score not because they represent a large share of Jordan's exports, but because they represent an important share of Syria's proliferation-relevant imports (see Figure 10). Such decompositions of Proliferation Trade Risk can be generated for any country of interest.

In addition, the data supports further decomposition of these proliferation trade risks by commodity type. The breakdown of Jordan's proliferation trade risk by industrial sector, depicted in **Figure 5**, shows that the risk comes predominantly from metals exports (to Syria and Pakistan), accounting for approximately 70% of Jordan's proliferation trade risk. Chemicals represent approximately 25% of proliferation trade risk from exports to China, India, Syria, and Iran. Equipment exports account for a minor share of proliferation trade risk, primarily from equipment exports to Syria.

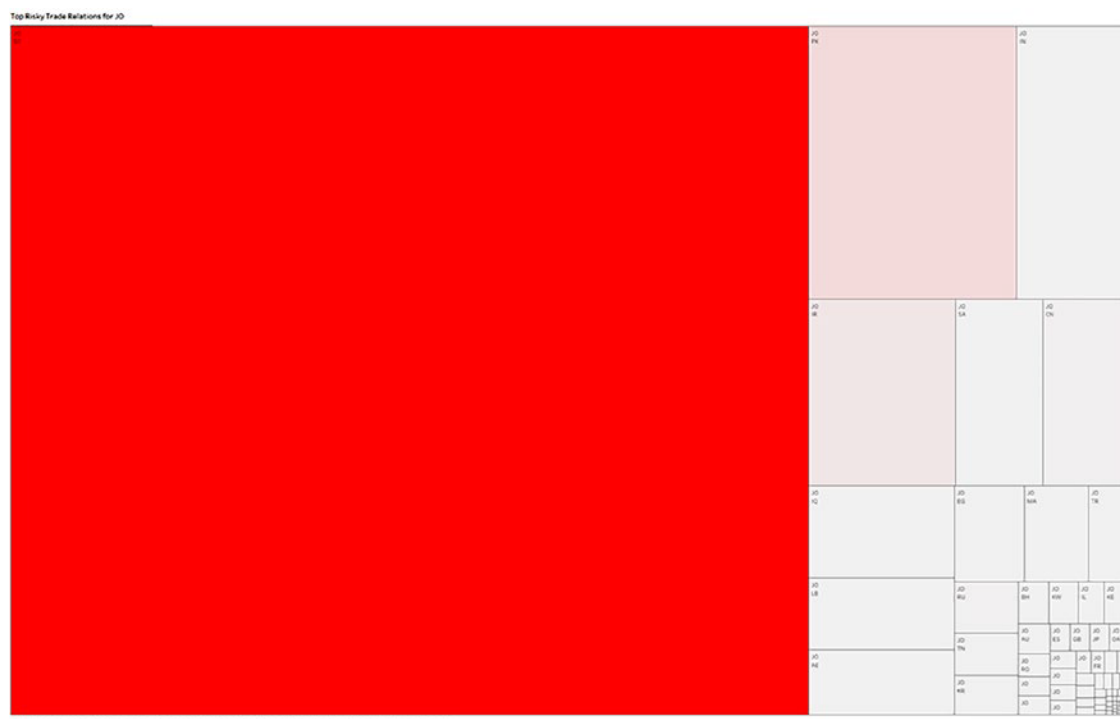


Figure 4: Tree-map representing Jordan's proliferation trade risk by trading partner.

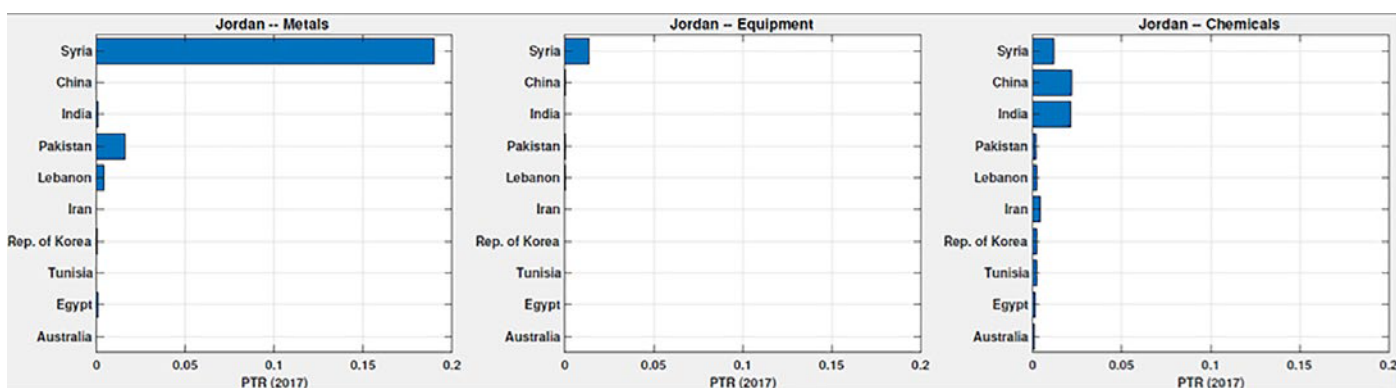


Figure 5: Jordan's Proliferation Trade Risk profile by industrial sector.

Figure 6 digs deeper into Jordan's metal trade to Syria. The top portion shows that Jordan's major metal export is aluminum (HS Chapter 76). Of this, less than 2% is exported to threat countries (shown in red). However, looking at the bottom portion of Figure 6, Jordan's exports represents a significant fraction of Syria's imports; Jordan is Syria's fourth largest supplier of Aluminum (shown in blue). This is a small trade flow for Jordan, but an important one for Syria, which is what the Proliferation Trade Risk metric measures.

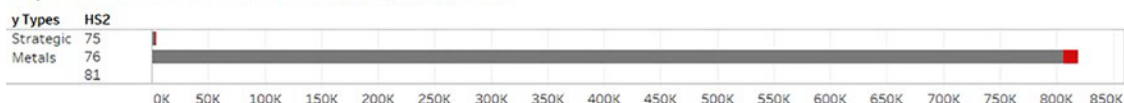
It is also possible to use this methodology to rank the proliferation trade risk of imports to an intermediary country, and to decompose that trade risk by supplier and commodity type. Figure 7 shows the highest Proliferation Trade Risk scores arising from exports to Jordan based on their potential for re-export to threat countries. This suggests, for example, focusing transshipment control efforts on shipments of metals from United Arab Emirates, China,

Saudi Arabia, Bahrain, South Korea, and Qatar; shipments of chemicals and equipment from China and chemicals from Saudi Arabia.

5. The big picture

Figure 8 brings together the overall ranking and comparison among countries with the breakdown of each country's risky trade relationships all on the same scale. The first block at the top left represents China's Proliferation Trade Risk and is subdivided to show the relative contributions arising from China's export destinations. The block at the lower left similarly represents South Korea's Proliferation Trade Risks, and so on. The colour scale indicates the relative magnitude of Direct Proliferation Trade Risk while the size of each area represents the total Proliferation Trade Risk (Direct plus Indirect).

Exports from Jordan to All for 2015, 2016, 2017



Imports to Syria from All for 2015, 2016, 2017

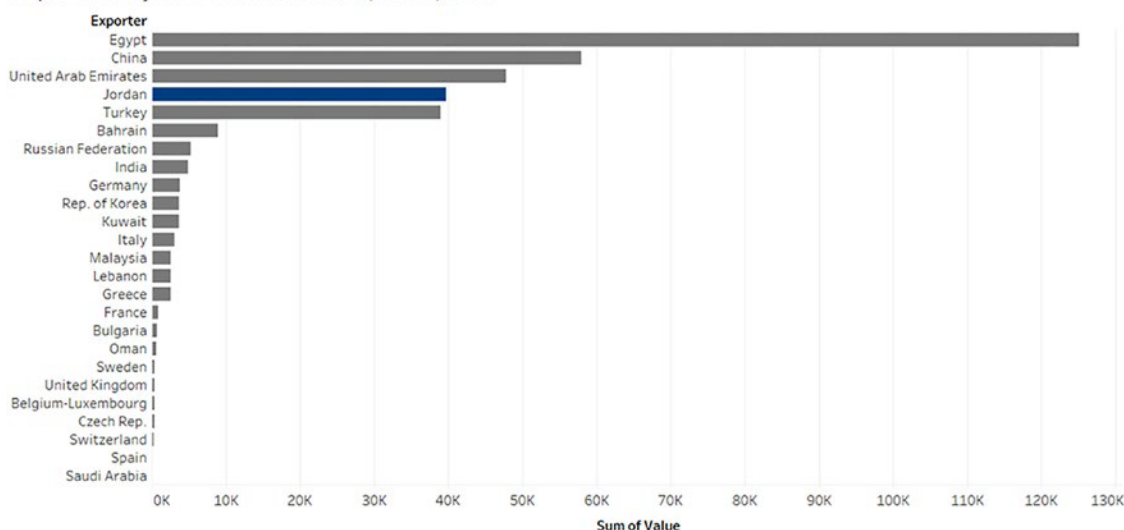


Figure 6: Jordan's exports of metals to Syria and Syria's imports of metals from all suppliers.

Threat PTR decomposition for Jordan

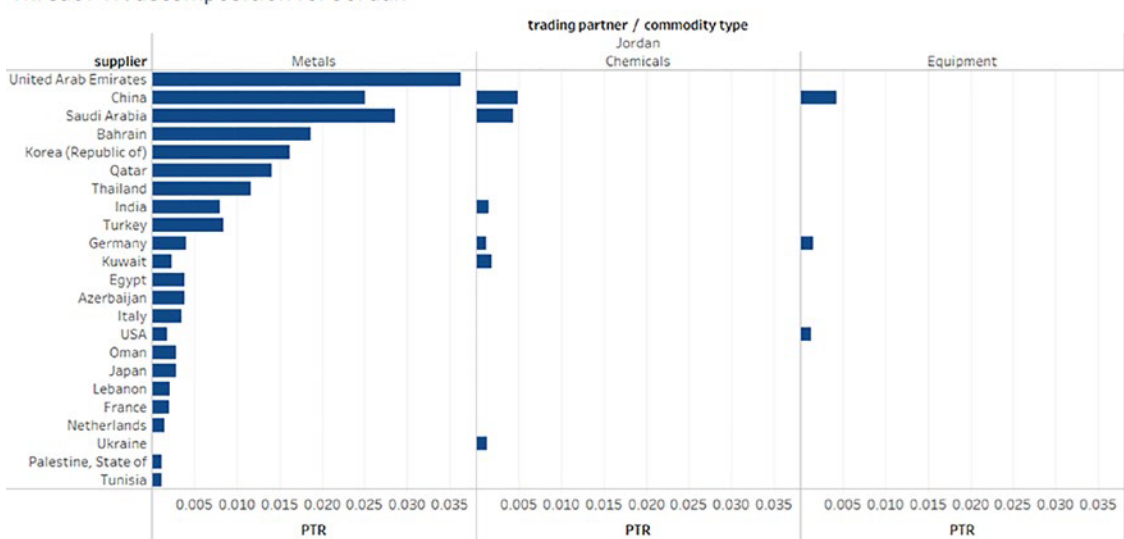


Figure 7: Import risk profile for Jordan.

top risky trade relations

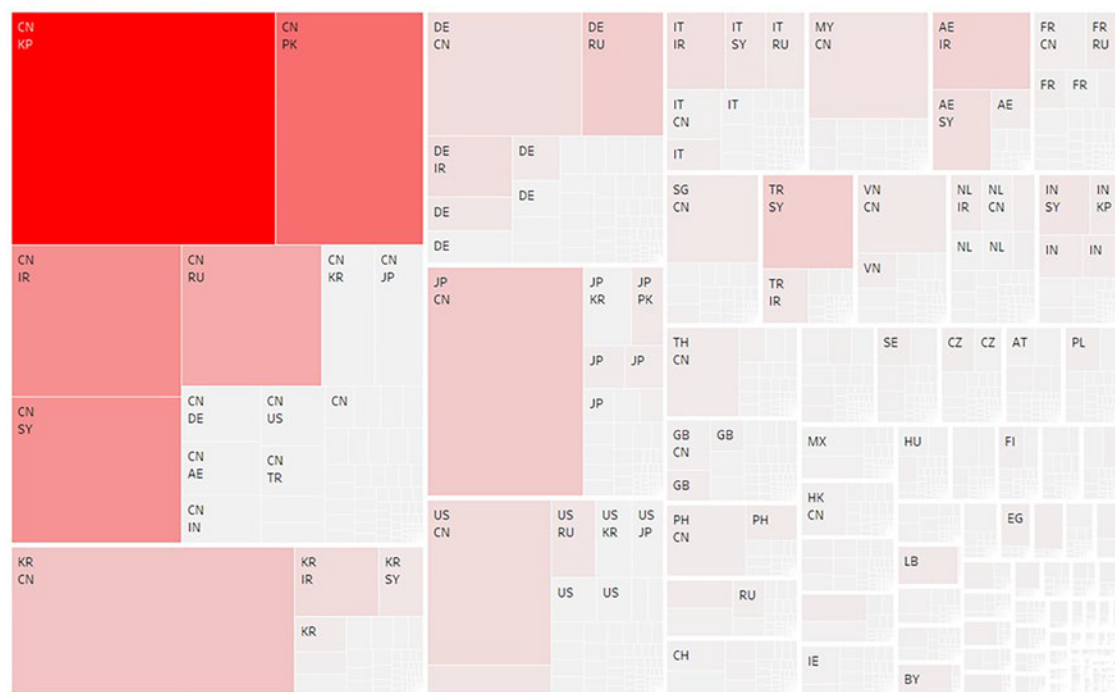


Figure 8: Global Proliferation Trade Risks.

top risky trade relations* excluding CN, KR, DE, JP, US

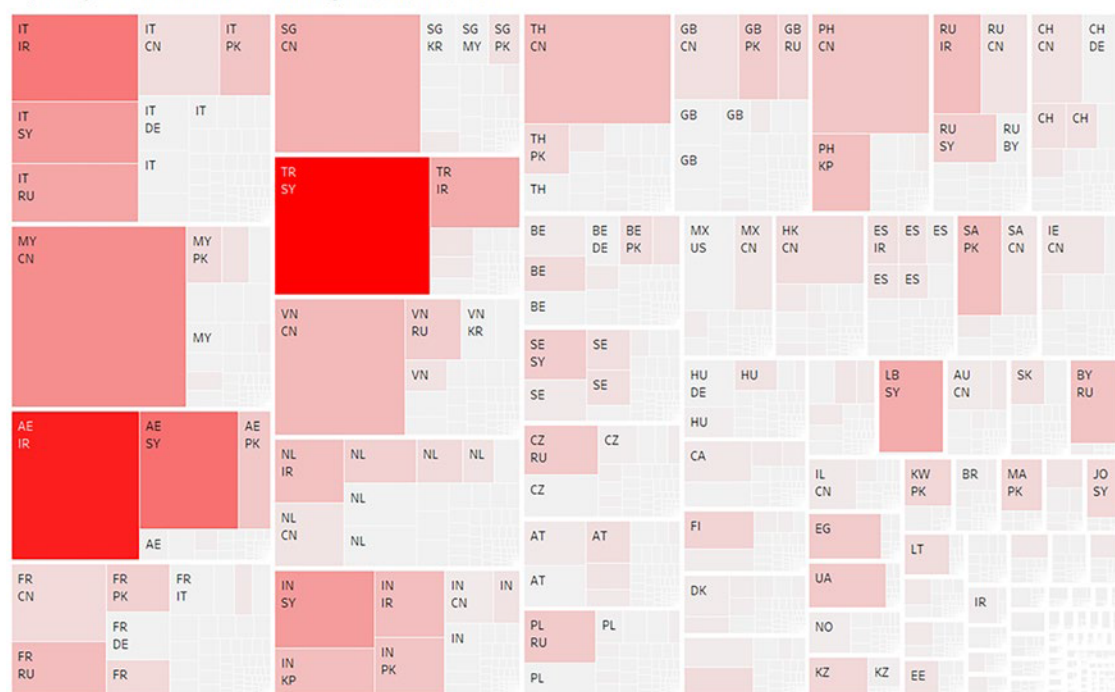


Figure 9: Global Proliferation Trade Risks excluding China (CN), South Korea (KR), Germany (DE), Japan (JP) and the United States (US).

As was done in Figure 3, Figure 9 repeats the previous figure but excludes the top 5 Proliferation Trade Risks to show the remaining countries more clearly.

6. Threat perspective

The calculations can also be used to view proliferation-relevant trade from the perspective of the designated threat countries. Based on the original PNNL study, the figures that follow show the top suppliers of proliferation-relevant trade to each of the designated proliferation threat countries [1].

Syria's (SY) most important suppliers based on Proliferation Trade Risk were China (CN), Turkey (TR), United Arab Emirates (AE), India (IN), Italy (IT), South Korea (KR), Lebanon (LB), and Germany (DE).

Iran's (IR) most important suppliers based on Proliferation Trade Risk were China (CN), United Arab Emirates (AE), South Korea (KR), Germany (DE), Italy (IT), Turkey (TR), Russia (RU), and India (IN).

Pakistan's (PK) most important suppliers based on Proliferation Trade Risk were China (CN), the United States (US), Germany (DE), Japan (JP), Saudi Arabia (SA), Italy (IT), India (IN), United Arab Emirates (AE), and the United Kingdom (GB).

DPRK's most important suppliers based on Proliferation Trade Risk were China (CN), India (IN), and the Philippines (PH).

China's (CN) most important suppliers based on Proliferation Trade Risk were South Korea (KR), Japan (JP), the United States (US), Germany (DE), Malaysia (MY), Singapore (SG), Vietnam (VN), and Thailand (TH).

Russia's most important suppliers based on Proliferation Trade Risk were China (CN), Germany (DE), the United States (US), Italy (IT), France (FR), South Korea (KR), Belarus (BY), Japan (JP), Poland (PL), Czech Republic (CZ), and Ukraine (UA).

7. Conclusion

The Proliferation Trade Risk metric was developed to help prioritize non-proliferation export control capacity building engagement and to tailor that engagement to maximize risk reduction. Beyond this purpose, the metric can help inform any country's export control efforts. The decomposition of the proliferation trade risk metric can identify specific industrial sectors and trade relationships of greatest importance for outreach and enforcement measures. These supply-side perspectives can also be complemented by threat-based profiles identifying the most important suppliers to each threat country.

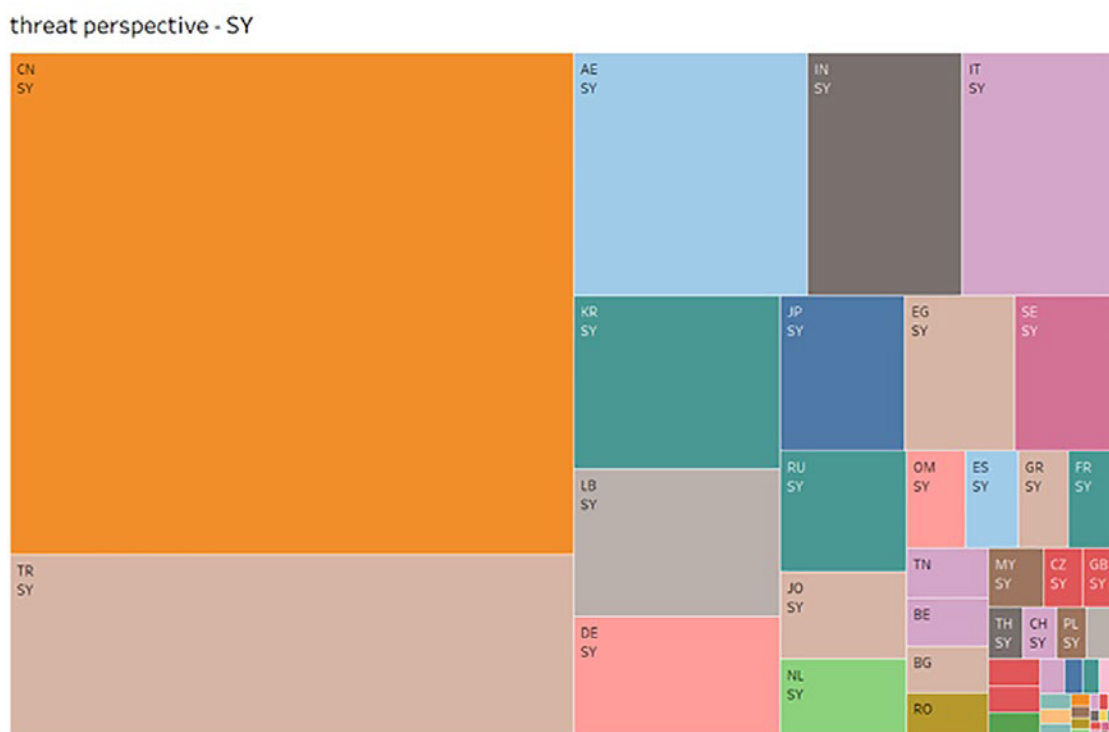
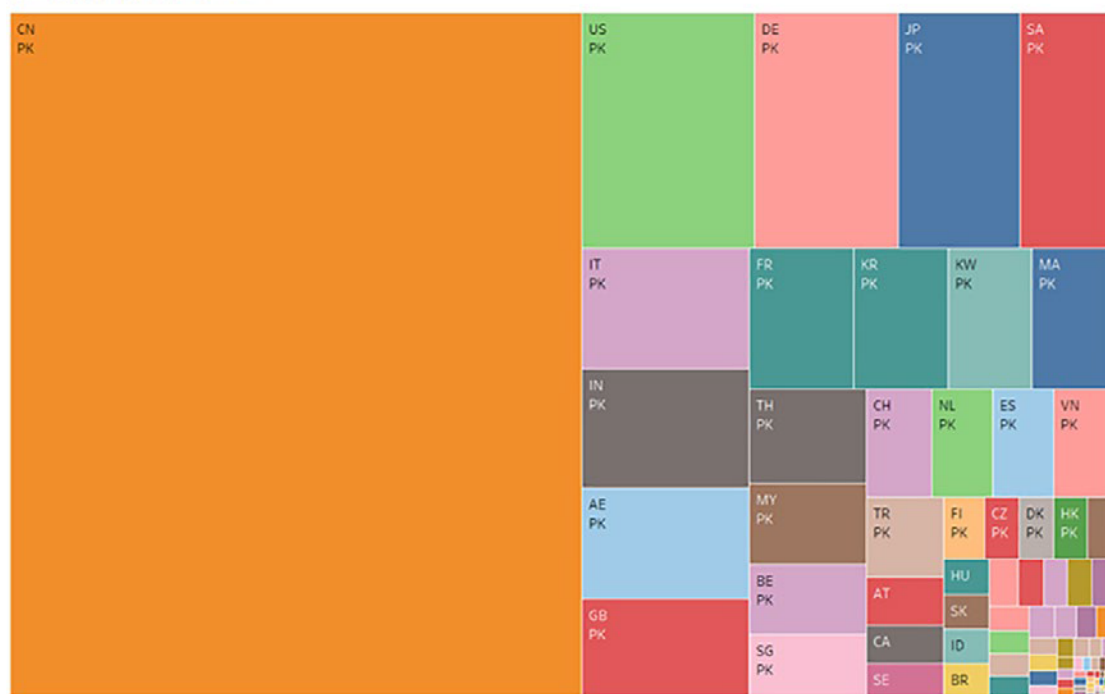


Figure 10: Top suppliers of proliferation-relevant exports to Syria (SY) in 2016

threat perspective - IR

**Figure 11:** Top suppliers of proliferation-relevant exports to Iran (IR) in 2016

threat perspective - PK

**Figure 12:** Top suppliers of proliferation-relevant exports to Pakistan (PK) in 2016

threat perspective - KP



Figure 13: Top suppliers of proliferation-relevant exports to DPRK (KP) in 2016

threat perspective - CN

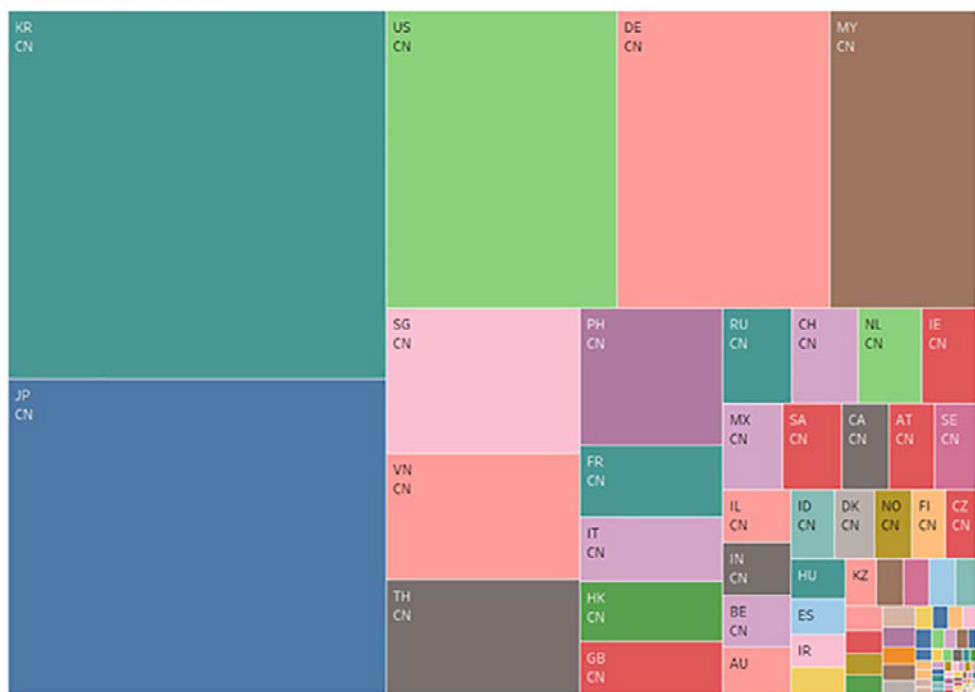


Figure 14: Top suppliers of proliferation-relevant exports to China (CN) in 2016

threat perspective - RU

**Figure 15:** Top suppliers of proliferation-relevant exports to Russia (RU) in 2016

8. References

- [1] Heine, P., Blackburn, T. and Attarian, A., *TradeRisk: IN-ECP's development and examinations of a proliferation trade metric*, Pacific Northwest National Laboratory, 2018, PNNL-28455.
- [2] Versino, C., Heine, P. and Carrera, C., *Strategic Trade Atlas — Country-based views*, Publications Office of the European Union, Luxembourg, 2018. Retrieved from: <https://ec.europa.eu/jrc/en/publication/strategic-trade-atlas-country-based-views-0>
- [3] *National Intelligence Strategy of the United States of America*, Office of the Director of National

Intelligence, 2019. Retrieved from: https://www.dni.gov/files/ODNI/documents/National_Intelligence_Strategy_2019.pdf

- [4] *National Security Strategy of the United States of America*, White House, 2017. Retrieved from: <https://www.whitehouse.gov/wp-content/uploads/2017/12/NSS-Final-12-18-2017-0905-2.pdf>
- [5] *Nuclear Posture Review*, US Department of Defense, Office of the Secretary of Defense, 2018. Retrieved from: <https://dod.defense.gov/News/SpecialReports/2018NuclearPostureReview.aspx>

